

**TEV GAMMA-RAY ASTRONOMY AND THE
DARK MATTER**

by

Jeter C Hall IV

A dissertation submitted to the faculty of
The University of Utah
in partial fulfillment of the requirements for the degree of

Doctor of Philosophy

Department of Physics

The University of Utah

May 2007

UMI Number: 3258571

INFORMATION TO USERS

The quality of this reproduction is dependent upon the quality of the copy submitted. Broken or indistinct print, colored or poor quality illustrations and photographs, print bleed-through, substandard margins, and improper alignment can adversely affect reproduction.

In the unlikely event that the author did not send a complete manuscript and there are missing pages, these will be noted. Also, if unauthorized copyright material had to be removed, a note will indicate the deletion.

UMI[®]

UMI Microform 3258571

Copyright 2007 by ProQuest Information and Learning Company.

All rights reserved. This microform edition is protected against unauthorized copying under Title 17, United States Code.

ProQuest Information and Learning Company
300 North Zeeb Road
P.O. Box 1346
Ann Arbor, MI 48106-1346

Copyright © Jeter C Hall IV 2007

All Rights Reserved

THE UNIVERSITY OF UTAH GRADUATE SCHOOL

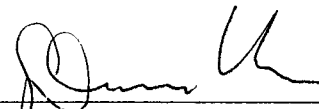
SUPERVISORY COMMITTEE APPROVAL

of a dissertation submitted by

Jeter C Hall IV

This dissertation has been read by each member of the following supervisory committee and by majority vote has been found to be satisfactory.


September 26, 2006


Chair: David Kieda

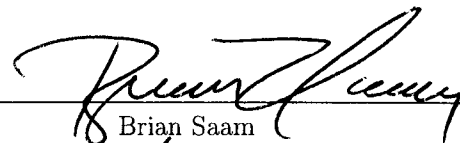
September 25th 2006


Stephan LeBohec

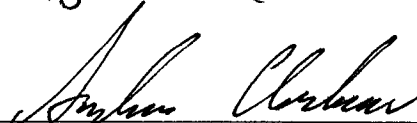
September 25, 2006


Paolo Gondolo

September 25th, 2006


Brian Saam

September 25th 2006


Andrej Cherkaev


THE UNIVERSITY OF UTAH GRADUATE SCHOOL

FINAL READING APPROVAL

To the Graduate Council of the University of Utah:

I have read the dissertation of Jeter C Hall IV in its final form and have found that (1) its format, citations, and bibliographic style are consistent and acceptable; (2) its illustrative materials including figures, tables, and charts are in place; and (3) the final manuscript is satisfactory to the Supervisory Committee and is ready for submission to The Graduate School.

9/26/2006
Date



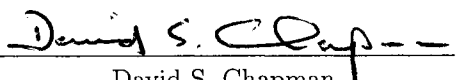
David Kieda
Chair, Supervisory Committee

Approved for the Major Department



Pierre Sokolsky
Chair/Dean

Approved for the Graduate Council



David S. Chapman
Dean of The Graduate School

ABSTRACT

In our Universe there is evidence that most of the matter is in the form of cold, dark, nonbaryonic matter. One candidate for this dark matter is the neutralino, the lightest, neutral, supersymmetric particle. The neutralino would annihilate other neutralinos and produce light at energies ranging from MeVs to TeVs. I discuss the possibility of using the technique of Gamma-Ray Astronomy, specifically ground based Imaging Atmospheric Cherenkov Telescopes, to observe gamma rays due to exotic particle annihilation. TeV radiation has been observed from the direction of the center of the Milky Way, and I discuss the possibility that this radiation is due to neutralino annihilation in the dark matter halo. Additionally I took data with the Whipple 10m telescope on several promising, nearby elliptical galaxies, M33, M32, and the dwarf spheriod galaxies Ursa Minor and Draco. I derive upper limits for the gamma-ray flux from these objects and discuss the implications these limits have for models of the neutralino.

For I can end as I began. From our home on the Earth, we look out into the distances and strive to imagine the sort of world into which we are born The search will continue. The urge is older than history. It is not satisfied and it will not be suppressed.

Edwin Hubble 1953

CONTENTS

ABSTRACT	iv
ACKNOWLEDGEMENTS	viii
CHAPTERS	
1. GAMMA-RAY ASTRONOMY	1
1.1 History of Gamma-Ray Astronomy	3
1.2 Current Observatories	6
1.3 Established TeV Gamma-Ray Sources	8
1.3.1 Galactic Sources	9
1.3.2 Extragalactic Sources	10
1.3.3 Dark Sources	12
1.4 Future of Gamma-Ray Astronomy	13
1.4.1 Simulated Ideal TeV Observatory	13
1.5 Discussion	16
2. THE DARK MATTER PROBLEM	20
2.1 Mass Measurements	21
2.2 Hubble's Law and the Big Bang	23
2.3 The Standard Cosmology	24
2.4 Cosmic Microwave Background	27
3. DARK MATTER ANNIHILATION	30
3.1 Candidates for the Dark Matter	30
3.2 WIMP Annihilation	33
4. SOURCE SELECTION	38
4.1 The Galactic Center	39
4.2 Dwarf Galaxies	40
4.3 M31-M33	42
5. THE GALACTIC CENTER	44
5.1 Particle Model Examples	46
5.2 DM Density Profile	48
5.3 Limits From the HESS Angular Profile	51
5.4 Limits From Stellar Dynamics	55
5.5 Results	57

6.	OBSERVATIONS WITH THE WHIPPLE TELESCOPE	64
6.1	The Data and Data Quality	64
6.1.1	Draco	66
6.1.2	Ursa Minor	68
6.1.3	M33	68
6.1.4	M32	68
6.1.5	Crab	69
6.1.6	Background Estimation	69
6.2	Analysis	70
6.2.1	Calibration	70
6.2.2	Image Cleaning	75
6.2.3	Parametrization - Hillas Parameters	75
6.2.4	Parameter Cuts	76
6.2.5	Parameter Optimization	81
6.2.6	Crab Normalization	83
6.2.7	Crab Plerion	83
6.3	Analysis Results	87
7.	DISCUSSION AND CONCLUSIONS	101
	REFERENCES	108

ACKNOWLEDGEMENTS

This work is the culmination of a long career as a graduate student. In this world we stand on the backs of giants both alive and dead. The view is amazing.

There are many people in the Whipple collaboration to whom I am grateful, and without whom I would never have finished this work. I would like to acknowledge the University of Utah and the Physics department for a wonderful academic environment. Thank you to my fellow graduate students for friendship and academic help. I would especially like to thank Gary Walker and Tomo Nagai for their help on much of the work in this dissertation.

Thanks to David Kieda for unquestioning support. I am amazed at the way he gets experimental physics done. Thanks to Vladimir Vassiliev for encouraging my curiosity in this field. He is brilliant and has many great ideas. Thanks to Paolo Gondolo for help and for encouraging my own ideas. He publishes more than anyone I know, and I know this is only a fraction of the good ideas he has to share. Thanks to Stephane LeBohec for his enthusiasm and encouragement. Thanks to Tessa for her patience.

CHAPTER 1

GAMMA-RAY ASTRONOMY

Ground-based gamma-ray astronomy is a natural progression in the study of radiation and the major scientific motivation for this dissertation. Gamma-ray astronomers have recently improved their telescopes and gained an order of magnitude in sensitivity. The number of gamma-ray sources is increasing from just a handful to dozens of sources. This new sensitivity allows a view of the important sources of radiation around a teraelectron volt ($1 \text{ TeV} = 10^{12} \text{ eV}$). This is just at the threshold of particle accelerators on Earth, which has two experimental advantages. First, the interactions in the atmosphere have a center of mass energy around 1 GeV so the atmospheric processes are now well understood. Second, the astrophysical production site is more energetic than any laboratory processes, making TeV astrophysics a test of extensions of physics. Besides sources of radiation with established astrophysical acceleration processes, this field also holds the exciting possibility of finding some new natural phenomena at energies above those accessible on Earth. An undiscovered massive particle decaying into TeV photons is the concrete example of new physics that could be observed, which I will explore in this dissertation. Finding a new fundamental particle could be a discovery from this new window on our Universe.

Observing photons with energies above 100 keV, gamma rays, today is done with two techniques. Gamma rays can be observed with space-based telescopes. These satellites convert incident gamma rays into charged particles, and the energies of these particles are measured in a calorimeter. Satellite gamma-ray observatories have been successful in exploring the sky in the energy range from 100 keV to 1 GeV. Above this energy the cost of satellites with the large areas required

becomes prohibitively expensive. Compton Gamma Ray Observatory (CGRO), one of NASA's Great Observatories, was home to the highest energy space-based gamma-ray experiment, EGRET. New gamma-ray satellites are being launched; the successor of EGRET is the Gamma-ray Large Area Space Telescope, GLAST, which will be particularly relevant to searches for DM. The launch of GLAST is planned for 2007. GLAST will study photons with energies up to 100 GeV, with its best sensitivity below 10 GeV.

At energies around 100 GeV a new "window" opens up in the atmosphere. The gamma rays start generating a significant amount of visible and ultraviolet light when they hit the atmosphere. This light can be measured from the ground with large optical telescopes. This method was first suggested in the late 1950s and attempted in the 1960s as a method of studying the cosmic radiation, especially the sources of the cosmic radiation because the photons should point directly back to their point of origin. This is in contrast to all the charged particles in the cosmic radiation, which will bend in magnetic fields. The first repeatable measurement was demonstrated by the Whipple collaboration in 1989 with data on the Crab pulsar plerion. Currently this method is being explored by a new generation of instruments that is just now coming online. The HESS array is currently the most sensitive of the new generation and is making a large contribution to astronomy in the energy range 100 GeV to 50 TeV.

In this chapter I will touch briefly on the history of gamma-ray astronomy. The technique used in this dissertation is the ground-based technique, so I will focus on how this technique is accomplished. Finally I will discuss a few gamma-ray telescopes, mainly the 10 m gamma-ray telescope at the Fred Lawrence Whipple Observatory (hereafter referred to as the Whipple Telescope) as well as the new generation of ground-based telescopes. Later in the dissertation results from the HESS array will be discussed and some data from the Whipple Telescope will be presented in the context of an indirect search for DM.

1.1 History of Gamma-Ray Astronomy

In the energy range of interest the story starts with the discovery of cosmic radiation. Around 1900 [1], scientists investigating radioactivity noticed that charge leaking from a metal container could be reduced by screening the container with a radiation shield, this was confirmed by two experiments in 1903 [2]. This pointed to the existence of some penetrating form of radiation that was causing the air to ionize and form a current that allowed charge to leak from the container. In the time period from 1910-1914, a number of balloon experiments [3, 4] were conducted that measured the ions in air as a function of elevation. Although the ionization of air decreased slightly as the balloons left the Earth, the rate started increasing again with altitude. Although not settled for at least a decade [2], this was discussed as the first evidence of the cosmic nature of this background radiation. Many scientists tried to prove the cosmic nature of this radiation, because this allowed the study of astrophysical phenomenon with rays that have energies much greater than any known processes at the time. An analysis by Pierre Auger in 1939 showed that this cosmic radiation extended in energy up to at least 10^{15} eV [5]. He states that it is “actually impossible to imagine a single process able to give to a particle such an energy.”

As scientists started studying the cosmic rays, new avenues of detection started to open up. In 1948 P. M. S. Blackett noted that a small portion of the night sky glow is due to Cherenkov radiation [6]. Cherenkov radiation is the radiation emitted by a material in response to a flux of charged superluminal particles. More specifically, “radiation of frequency ω occurs if the velocity of the particle exceeds the phase velocity of waves of that frequency in the medium concerned” [7]. The spectrum of the Cherenkov light is proportional to ν^2 so most of the Cherenkov light in the atmosphere is blue and ultraviolet. The radiation is emitted by the medium in response to the field of the particle in contrast to bremsstrahlung, which is emitted by the energetic particle itself. Although only a small fraction of the shower energy is released in Cherenkov light, this light is the brightest evidence of the cosmic radiation that reaches the Earth.

About this time, the processes involved with high energy cosmic rays in the atmosphere were laid out [8, 9]. This theory predicted a large amount of superluminous charged particles resulting from a cosmic ray interacting with the atmosphere. The interaction of a cosmic ray with the atmosphere became known as an Extensive Air Shower (EAS). In an EAS the primary particle is relativistic so it is able to create a large number of particles. For example, as shown in Fig. (1.1), for a photon initiated shower, when a high energy photon strikes the atmosphere it will create an electron-positron pair. These particles will shed gamma rays through bremsstrahlung. These bremsstrahlung gamma rays will again pair produce in the atmosphere. These processes will continue to cascade until the particles have a low enough energy to be lost to ionization (~ 1 GeV.)

In 1953 the first cosmic ray telescope was constructed by Galbraith and Jelley [10]. A schematic diagram of this telescope is shown in Fig. (1.1). This telescope consisted of a 25 cm parabolic mirror. A photomultiplier tube (PMT) was placed in the focal plane of the mirror. This setup was mounted inside a standard issue laboratory trashbin. The night sky dominated the PMT output, so they set the threshold on a discriminator fairly high so that the rate was one to two per minute. To check that this rate was due to something in the sky, a light bulb was attached to the trash can lid and it was placed back on the telescope. The voltage across the light was adjusted so that the current observed in the PMT was the same as when the lid was off the telescope. The rate of one to two events per minute disappeared and the first Atmospheric Cherenkov Telescope (ACT) was born.

A goal in the study of cosmic radiation was to observe anisotropy in the form of point sources. Point sources would have two implications. First was that this anisotropic portion of the cosmic rays was neutral and probably gamma rays; any charged particle would bend in the Galactic magnetic field, neutrinos are difficult to detect, and other neutral particles, such as neutrons, have short lifetimes. Second, these point sources would be the directions of the high energy processes that are accelerating or interacting with the cosmic rays. Since these particles have energies much greater than anything manmade on Earth, these cosmic ray sources would

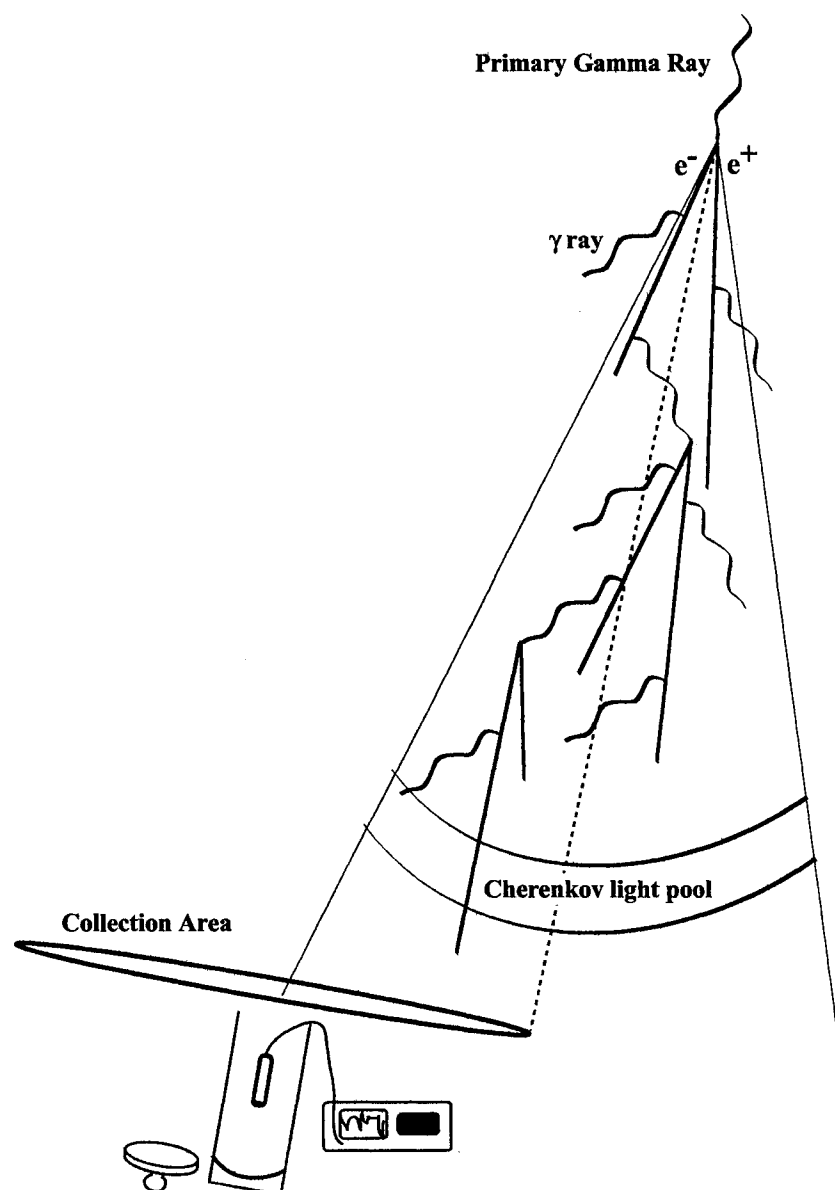


Figure 1.1. The first gamma-ray telescope consisted of a 25 cm parabolic mirror mounted to a trashbin. The camera consisted of a single PMT with a 22° field of view. A schematic of an electromagnetic shower is shown. The primary gamma ray pair produces an electron and positron. These charged particles will emit gamma rays through the bremsstrahlung process and these gamma rays will pair produce. These processes will go on until the energy of the primary is finally lost to ionization. During the shower the air will emit Cherenkov radiation as the electrons and positrons will have velocities greater than the speed of light. These Cherenkov photons build up in a correlated light beam with a time-spread of a few nanoseconds for typical impact parameters. The PMT detects these photons so the collecting area of the telescope is approximately as large as the Cherenkov wave front. A typical radius for this wavefront is about 120 m.

be a good astrophysical laboratory for studying these high energy acceleration process and their products. There were attempts to find point sources in the cosmic radiation [11, 12], and the first statistically significant and steady detection came in 1989 with the Whipple Telescope at the Fred Lawrence Whipple Observatory on Mt. Hopkins in southern Arizona. The Whipple collaboration was able to detect a steady point-like anisotropy in the cosmic radiation in the direction of the Crab pulsar. This detection of gamma rays has been reproduced many times. The Crab has become the standard candle of TeV astronomy because it is bright and constant. The Crab is now usually the first source that a gamma-ray telescope is pointed to in order to establish its performance.

1.2 Current Observatories

The major innovation in the Whipple Telescope was the camera. Like Galbraith and Jelley, the Whipple started out in 1968 with a single PMT in the field of view. This PMT collected all the photons within a 1° field of view and the only directional information from the PMT is that the photons came from within this field of view. In 1980s the Whipple collaboration put many pixels in the focal plane. Starting with 37 pixels in 1982 with upgrades in the late 1980s and all throughout the 1990s, these cameras with multiple pixels and fast electronics were able to record an image of the Cherenkov light from the shower. Imaging the shower improved the reconstruction of the primary particle direction down to a fraction of a degree.

A picture of the Whipple Telescope is shown in Fig. (1.2). The primary optical element is a faceted 10 m mirror. The optical design is an $f/0.7$ Davies-Cotton [13]. The current camera, the GRANITE-III camera, consists of 379 half-inch pixels with a hexagonal geometry. Each pixel has a field of view of 0.12° and the camera has a field of view of 2.6° . This camera was installed in the Fall of 1999.

One goal of the many upgrades to the camera in the 1990s was to lower the energy threshold of the telescope. By introducing high resolution cameras, smaller low energy images may come into view. The main limitation to this is small images in the camera created by local muons that mimic gamma-ray air showers. The

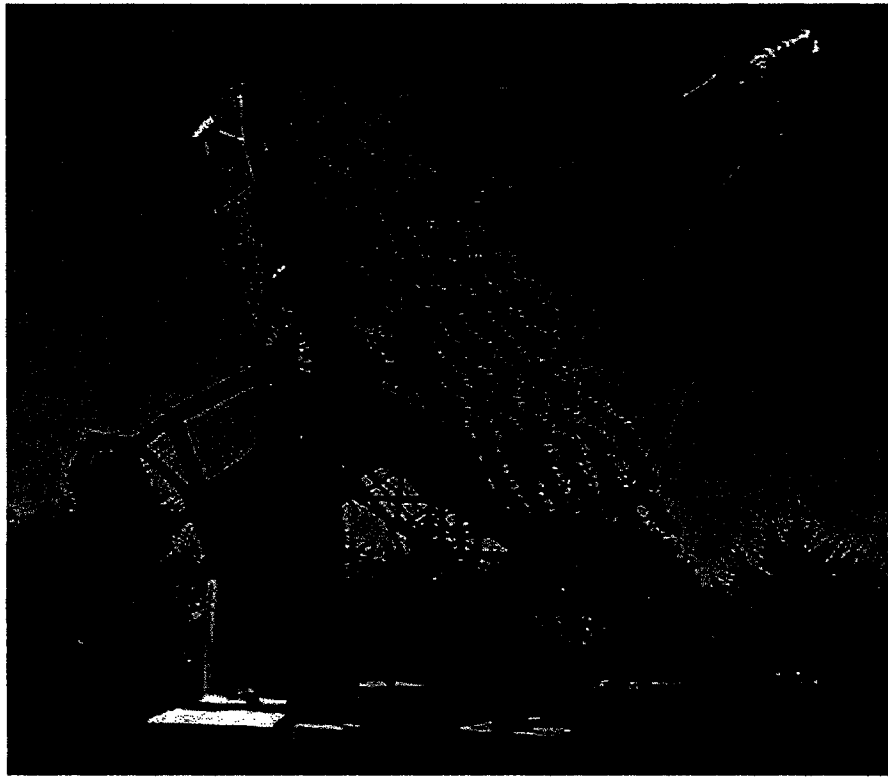


Figure 1.2. The 10 m gamma-ray telescope on Mount Hopkins in Arizona (the Whipple Telescope).

HEGRA [14] ACT array made a major advance in rejecting this background during the same time that the Whipple collaboration was optimizing their camera. A single muon with a trajectory coincident with the telescope optical axis will create an image of a circle in the focal plane. This is because the air around the muon is emitting Cherenkov radiation with the characteristic Cherenkov angle, isotropically in azimuth, which creates a circle if all the light is collected. If the muon trajectory is parallel to the optical axis but at a distance greater than the radius of the telescope aperture, then only part of the circle will show up in the image. At a distance of ~ 25 ms the muon arc will take up about three pixels in the Whipple Telescope. This is indistinguishable from images of photons with energies less than ~ 400 GeV in the telescope. The trigger threshold of the Whipple Telescope is ~ 100 GeV, but this muon background pushes the energy threshold up to ~ 400 GeV

after analysis. The HEGRA telescope consisted of five identical telescopes with 8.5 m² reflectors. The cameras consisted of clusters of 271 photomultiplier tubes that imaged the EAS. The telescopes were situated at the corners of a 100 m square with the fifth telescope in the center. This telescope spacing allows for multiple views of air showers. Single relativistic particles that form a large background for single telescopes can be eliminated from array data by requiring two or more telescopes exceed a given threshold of light.

New ACT arrays are being built all over the world. In the United States, the Whipple collaboration has grown and become the VERITAS collaboration which is constructing an array in Arizona. The HEGRA collaboration in Europe split and grew forming two experimental collaborations, HESS and MAGIC. Finally, the Japanese have an experiment in Australia called CANGAROO that is a similar array of ACT telescopes. These telescopes are currently the largest optical telescopes in the world. HESS consists of four telescopes with 12 m diameter reflectors placed at the corners of a 100 m square. VERITAS also consists of four telescopes with 12 m diameters at baselines of 55 m to 140 m. CANGAROO is an array of 4 10 m telescopes.

Part of the HEGRA collaboration decided to increase the light sensitivity of the single telescope in an attempt to reach lower energies with the ACT method so they built a 17 m telescope on La Palma in the Canary Islands in the MAGIC experiment. They have been successful in reaching an energy threshold of ~ 100 GeV and now they are building another 17 m telescope to improve the background rejection capabilities.

1.3 Established TeV Gamma-Ray Sources

There are almost three dozen established gamma-ray sources today. Both galactic and extragalactic sources have been observed. There are only a few dozen known sources in the TeV sky, corresponding to a few source types, so I will very briefly mention each type of source.

1.3.1 Galactic Sources

There are two main confirmed sources of TeV radiation in the Galaxy, supernova remnants and compact binary systems. The first source discovered was the Crab, the remnant of the supernova in 1054 AD, which was noted by Chinese astronomers. This powerful event ejected a major portion of the original star into the surrounding volume. A pulsar was left in place of the progenitor. The magnetic field from this pulsar accelerates a plerion wind around the pulsar, which shines at TeV energies. This is the strongest apparent point source of cosmic radiation and the first significant source which was reported in 1989 [15]. The TeV radiation from the Crab pulsar has been studied for variations of any kind and no significant variation has been observed.

This was just the first plerion to be discovered. The catalogue of TeV plerions is growing. The HESS array in Namibia performed a scan of the galactic plane and discovered a few more plerions or possible plerion associations [16, 17]. They are MSH 15 – 52 [18], PSR J1617 – 5055 (?), PSR B1823 – 13 (?), and PSR J1803 – 2137 (?). The associations marked with question marks are tentative, and some unexpected features must be explained for these associations to be confirmed. One interesting feature is that the TeV emission region is usually offset from the pulsar position, indicating jet-like activity including some hints of asymmetrical jets.

Shell-type supernova remnants are now confirmed as bright in the TeV sky. Probably the best studied TeV supernova shell is the remnant RX J1713 – 3946 [19, 20]. A few more sources with possible associations to shell-type remnants have been observed by HESS in their survey of the Galactic Plane.

When particles are accelerated in systems such as supernova remnants, they travel through the galaxy. Giant molecular clouds will start shining when a large flux of this radiation is present [21, 22]. With this mechanism it is possible to measure the flux, spectrum, and some rough composition features of the Galactic cosmic radiation at the positions of these molecular clouds. The observation of gamma rays from the Galactic Center ridge [23] and the emission seems to show a

correlation with the CO density in this region. The CO density is a good indicator of the density of these molecular clouds. This opens up the possibility of studying and trying to understand the Galactic cosmic ray density in much more detail.

Compact binary systems are also a significant source of TeV radiation. These systems are the first variable sources to be found in the Galaxy. These systems have a normal main sequence star in a binary orbit with a compact object like a neutron star or black hole. The binary pulsar PSR B1259 – 63 was the first binary TeV source discovered [24]. The TeV emission was predicted well before the emission was detected [25]. The flux of gamma rays is correlated with the orbit of a pulsar around a massive Be star that is losing mass in a disk-like outflow. As the pulsar passes through the disk, TeV gamma rays are observed. The flux is stronger when the pulsar passes the disk, but there are some indications that the strongest inverse compton signal from this process is slightly displaced in time with the crossing of the disk.

LS 5039 was the first x-ray binary system to be observed in the TeV waveband [26]. This is a candidate microquasar with a massive star orbiting an unknown compact object. An accretion disk is thought to build up around the compact object. As the accretion disk collapses, the system will eject jets. Another microquasar was observed in very high energy gamma rays, LS I +61303 [27], and evidence of variability was seen. Variability is expected in these microquasars. Jet activity has been imaged with radio telescopes and so these systems are expected to be similar to accretion onto massive black holes in the centers of galaxies. Microquasars and quasars are expected to have accretion disks that shed their angular momentum by ejecting particles in a relativistic jet normal to the accretion disk.

1.3.2 Extragalactic Sources

These microquasars are believed to be similar to the known extragalactic sources, the quasars [28]. After the Crab pulsar plerion was observed at TeV energies with the Whipple Telescope in 1989, the Whipple collaboration discovered the first extragalactic source of TeV radiation, Markarian 421 [29], in 1992. The source of the high energy nonthermal radiation from Markarian 421 is believed to be the

active galactic nucleus (AGN) of this blazar. AGN eject particles in relativistic jets perpendicular to their accretion disks. This is thought to be the major mechanism of shedding angular momentum from the disk. When the jet is pointed at the Earth, the AGN is called a blazar. These objects were classified by their x-ray emission [30] and Markarian 421, and 501 [31], were at the top of this classification, and were subsequently observed to be the brightest TeV blazars. AGN typically exhibit a synchrotron-inverse compton spectrum with a broad nonthermal spectrum that has two peaks. The first peak of the most extreme blazars spectrum is in the hard x-ray or soft gamma ray bands. Other objects were selected on this basis and observed to emit TeV gamma rays.

AGN can be used as probes of the Universe. As we look back into the Universe, quasars are some of the most distant objects. The large time between the emission zone and the detection of photons at Earth allows a test of some long-term processes. One of the future possibilities of TeV astronomy is that it is possible to observe cosmological processes in the history of the Universe. Most gamma-ray AGN have been seen with redshifts of 0.1 or less. The furthest TeV gamma-ray blazar to be detected, PG 1553 + 113, has an unknown redshift. A lower limit of 0.8 was published for the redshift of PG 1553 + 113 [32]. However, other authors suggest a lower limit of 0.25, which is more reasonable given the expected gamma-ray flux and attenuation from infrared pair production.

One success of gamma-ray astronomy has been to use these AGN to set limits on the infrared background in the Universe, which has implications on early star formation models. TeV gamma-rays have high enough energy that they start to pair produce with infrared and microwave photons. This attenuation is actually the best possibility for measuring some wavebands of the infrared light because the backgrounds from the Solar System and the Milky Way are too bright and swamp the signal from the relic background light from the star formation history.

AGN are now known to be among the brightest sources in the TeV sky. The AGN are typically variable with 100% TeV luminosity changes on random time scales of < 0.5 hours to days. The flare of Markarian 421 in 1996 was the brightest

gamma-ray event observed with a flux 10 times that of the Crab plerion [33]. The fact that new galactic counterparts might be found with the microquasars may increase our knowledge about these massive systems which appear to be the similar despite the difference in overall size. The promise of these new sources is that we may decouple the intrinsic emission process at the AGN from the extrinsic process of gamma rays travelling through the infrared background field. This would allow a much more precise measurement of the relic cosmic infrared background light, because today the TeV spectral behavior of AGN is difficult to interpret and understand.

1.3.3 Dark Sources

It is evident that numerous new physical measurements are accessible in this very high energy radiation. As I started this work, I mentioned that the most exciting possibility when looking out into the sky in new wavebands is the possibility of seeing something new, something that can not be seen with previous astronomical instruments. One major legacy of EGRET is the large number of EGRET sources that have not been associated with known astrophysical objects [34]. The HESS array is beginning to show hints in the southern sky that there are natural systems that are observed most easily, or only, in very high energy radiation. In [17], the HESS collaboration reports that three of the gamma-ray sources identified in their [16] galactic scan have no apparent supernova remnant, pulsar, or EGRET counterparts. These could be some unobserved supernova remnant or plerion, but they could be indicative of some new TeV source of radiation that is dark in all previously accessible wavebands. Longer exposures over the whole sky, coupled with follow up measurements in other wavebands, should help us understand if these phenomena are “new physics” or shrouded, known astrophysical objects that are simply easier to see in the TeV energy range. This mystery, and all the physics discussed above, are driving the push for new, more sensitive TeV observatories.

1.4 Future of Gamma-Ray Astronomy

The gamma-ray astronomy is reaping the benefits of new, more sensitive telescopes, but even more sensitive telescopes, a next generation, are being proposed and built. There is some debate as to the direction of the next generation gamma-ray telescopes. There are a few directions that the development of these telescopes should naturally explore. These directions include increasing aperture, angular resolution, energy resolution, and energy range. Improving the aperture and angular resolution will increase the sensitivity of the telescope. Increasing the energy resolution and energy range will extend the information collected by the telescope.

Any time a major telescope is being constructed the scientific needs dictate the capabilities of the telescope. Scientific justifications for increasing the capabilities of these VHE observatories include study of high energy processes in the inner parts of the jet phenomena observed in accreting massive objects as well as the acceleration of particles in the winds produced in high energy processes such as supernova remnants. In addition to particle acceleration, the cosmic rays can interact with interstellar media modifying gamma-ray distributions; extragalactic gamma-ray sources can be used to probe cosmological information such as the intergalactic diffuse infrared background. Furthermore, the charged cosmic radiation that makes up most of the data taken by Cherenkov telescopes can be studied in more detail with future detectors [35].

Laboratory particle physics is limited by the particle accelerator energy scales at a few TeV, and particle physics on larger energy scales might be easier to study in astrophysical settings. The search for annihilating neutralinos, the lightest neutral supersymmetric particle, is one example of high energy particle physics that is being probed by these VHE observations. Understanding the capabilities of the method allows for understanding the science that such Cherenkov telescopes can observe in astronomy and cosmic ray physics.

1.4.1 Simulated Ideal TeV Observatory

It is true that the scientific justification dictates any improvements that can be achieved for a specific experiment, but the theoretical capabilities of an experimen-

tal method dictate the physical parameter space that is accessible and therefore the potential scientific discoveries of a particular experimental method. To study potential improvements to VHE observatories, I present simulations of a number of gamma-ray induced extensive air showers in order to examine the physical limit of the Imaging Air Cherenkov Telescope (IACT) technique. I ignore the real-world limitations of instrumentation and examine the information contained in the ground level Cherenkov photons produced in these air showers. Another study along these lines was initiated simultaneously [36]. The analysis used here was fairly simple, but it reproduces many aspects of modern Cherenkov observatories. The more sophisticated analysis in [36] indicates some interesting possibilities and I will try to explore these relationships in this section.

Monoenergetic populations of high energy photons were simulated cascading in the atmosphere. All Cherenkov photons reaching a depth of 763 gm/cm^2 are then collected and subject to the analysis. The spatial resolution of the photons is 0.1 m and the angular resolution is $0.3'$. This is slightly worse than the diffraction limit of $1''$ at 400 nm with this spatial resolution. A view of the detector data is shown in Fig. (1.3) for a 10 GeV shower. In this plot the data are clearly made up of circles in both physical space and angular space. Each circle is due to one particle emitting Cherenkov light. From these data it is possible to reconstruct the direction of each particle as the average of the photon directions. The position in the sky of this particle can then be estimated purely geometrically. It is possible to reconstruct all the tracks of the energetic, charged particles in the shower.

To reconstruct the direction of the primary photon, I use a simple average over the Cherenkov photon directions. The idea behind this method is that this should be an average over the directions of the Cherenkov emitting particles and should therefore be a good estimate of the momentum of the shower. Since the information on how much energy each particle carries is lost in this radiative process, I use all the charged particles to weigh the shower reconstruction in the direction of the most energetic particles. The energy of the shower is assumed to be proportional to the number of Cherenkov photons produced in the shower because the number

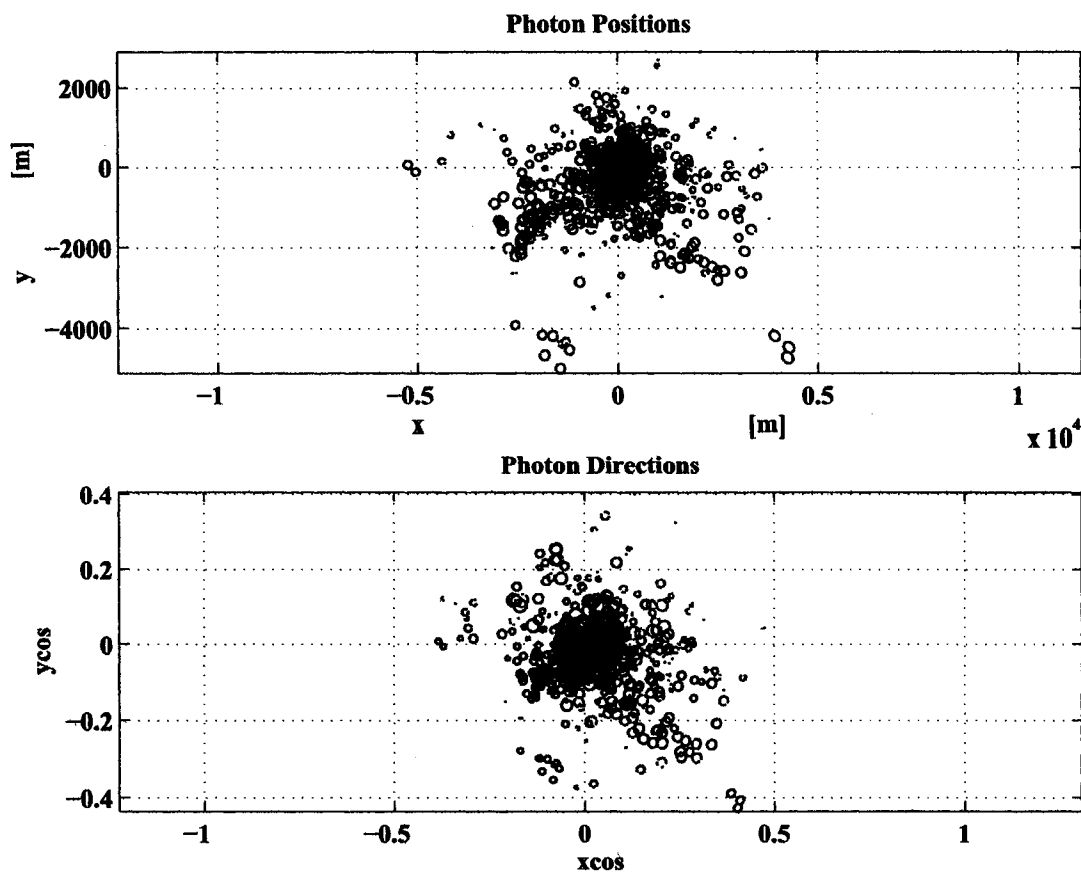


Figure 1.3. The data collected by an ideal detector. The x-axis of the top plot is in units of 10^4 m.

of Cherenkov photons is directly proportional to the number of particles created with energies above the Cherenkov threshold of ~ 2.5 MeV.

The results of the angular resolution reconstruction are shown in Fig. (1.4). The results are fit well by a power law distribution with the angular resolution $\Omega \sim E^{-0.2}$. For comparison, the angular resolution of HESS is quoted to be 0.1° with a threshold in the range 100-200 GeV. The energy resolution results are shown in Fig.(1.5). The energy resolution is constant at 11% at energies above 20 GeV. Below 20 GeV the energy resolution begins to degrade.

The energy resolution derived with this study seems to be very reasonable and

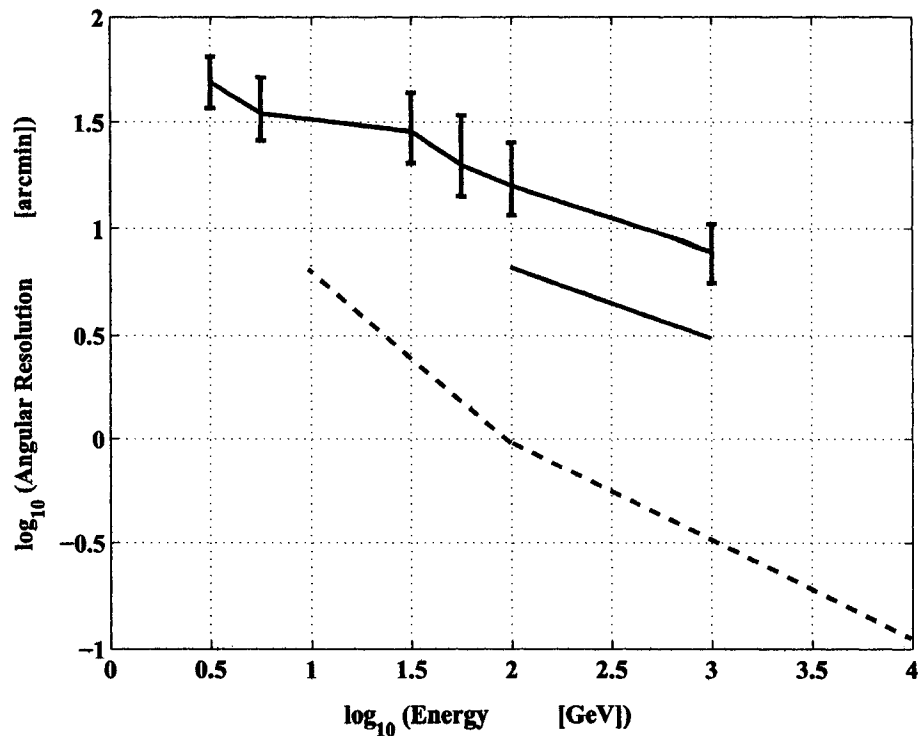


Figure 1.4. The angular resolution achieved by the ideal detector described. The solid black curve with errorbars is the resolution of the simulation described in the text. The dashed black line at the bottom was adapted from [36], which takes into account the correlations between the photons positions and directions. The short solid line between these two results is the experimental resolution of the HESS array.

similar to the performance exhibited by modern Cherenkov observatories. However, these results shows that order of magnitude gains in the energy resolution are probably not possible with this experimental technique. This is unfortunate because an exceptional energy resolution would help with the identification of new physics, because, as I discuss in the next few chapters, the evidence of such new physics could come in the form of gamma-ray spectral lines.

1.5 Discussion

I have simulated photons in order to understand the energy resolution and angular resolutions possible with the IACT method. I found that the current

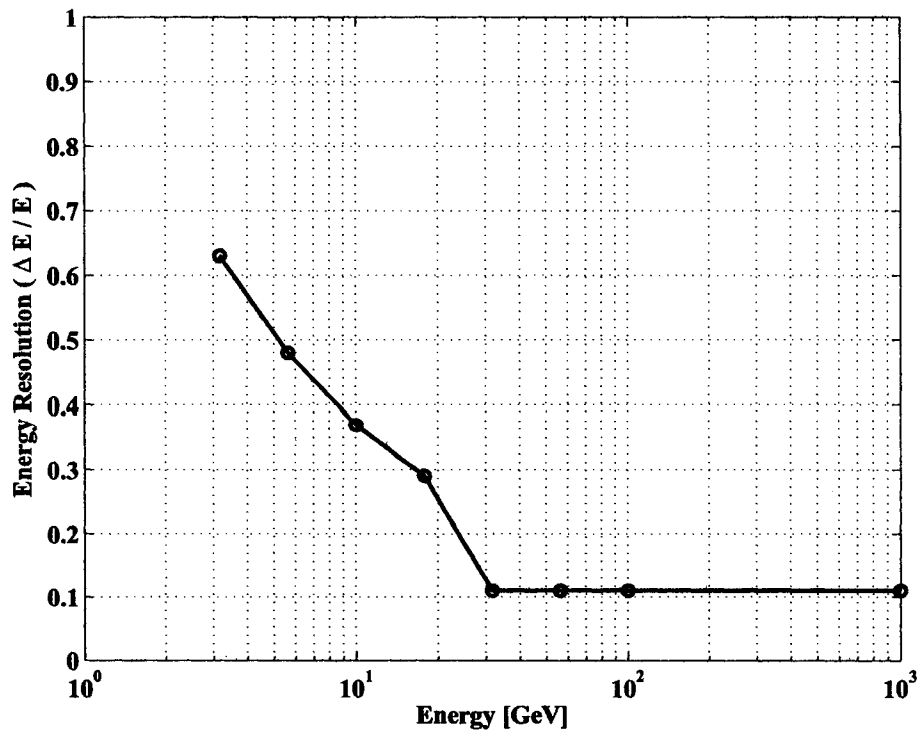


Figure 1.5. The energy resolution achieved by the ideal detector described. Currently the HESS array quotes the best energy resolution of any IACT array as 20%.

generation of IACTs coming on line are already at the limit of these two detector resolutions. Therefore increasing the information known about the air showers will not increase the telescope performance in these two key aspects. The energy resolution is approximately constant above 20 GeV but begins to degrade rapidly below this threshold. The angular resolution is found to be proportional to $E^{-0.2}$. This angular resolution is worse than what was found by a similar investigation [36], which takes into account the correlations between the photon directions and positions that were not used in this analysis.

The loss of angular resolution at low energies can be compensated by the large number of photons at these energies. The source location can be known to a factor of \sqrt{N} better than the angular resolution of a given event where N is the number of gamma rays detected. Low energies are interesting because the gamma-ray

horizon opens up for astronomy at approximately 50 GeV or so. At high energies the cosmic infrared background attenuates gamma rays, and the horizon shrinks dramatically for photons with energies greater than 1 TeV. Cosmic ray electrons, an irreducible background at low energies, become more dominant at low energies and it requires more study to understand if gamma rays below ~ 50 GeV are better studied on the ground or in space. Initial price estimates of ground-based arrays that could access these low energies are in excess of a couple hundred million dollars which is the near the cost of a space-based observatory. Current space-based gamma-ray observatories have larger fields of view, higher duty cycles, and more efficient background rejection, so they may be better platforms for observing the Universe at energies up to 10 – 50 GeV.

Higher energy photons have a smaller horizon. However, these energies are interesting because it is possible to study the large population of cosmic-ray sources in our galaxy at energies which can not be reached in a laboratory on Earth. In competition with designing an IACT that can probe cosmological distances, which would require greater light sensitivity (i.e., more mirror area per telescope), is an array of IACTs that would have the aperture to detect sources of even higher energies (10-1000 TeV). Opening up the high energy universe can help us probe natural phenomenon at energies that cannot be reached in the laboratory in the foreseeable future. Additionally the IACT method can be used to solve the perplexing problems of the origin of the cosmic rays and the origin of the features in the cosmic ray spectrum. Possible uses of the method also include a high-resolution spectroscopic IACT that could identify the direct Cherenkov light from the primary cosmic rays and do a high resolution study of the composition of the cosmic radiation. This, of course, is in addition to searching for photon production at the site of the cosmic-ray proton acceleration, one of the main goals, if not the main goal, of TeV astronomy.

If today's IACTs achieve the best possible angular resolution/energy resolution, it may be possible to reduce the performance of each individual IACT in an array and still achieve the same performance. For example it may be possible to increase

the pixel size, which would have the benefit of increasing the field of view with the same number of electronics channels. This must be done carefully because if the pixel size is too large then extra noise is introduced into the data. The sensitivity of the IACT method can still be improved through increasing the field of view, the collecting area, or the duty cycle. The IACT method currently has a small, $\sim 3.5^\circ$, field of view and a small, ~ 0.1 , duty cycle. The collecting area of the current instruments is approximately the size of the light pool, $\sim 10^8 \text{ cm}^2$ and an array of IACTs would have to have a larger area to substantially increase the sensitivity.

In this chapter I have given an overview of the field of TeV astronomy. TeV astronomy is a new astronomical window that has recently been opened, and now the number of sources is growing to the point that population studies are possible. This opens up the possibility of really understanding the sources of the Galactic cosmic radiation. Additionally other physics is open to these large observatories. These areas include the relic infrared radiation background from the history of star formation, the composition of the cosmic radiation, and dark matter, the focus of this dissertation. Many astronomers and laboratory physicists are searching for the dark matter. In the next chapter I will discuss the data that form our belief that the matter in the Universe is predominantly composed of some unknown dark matter.

CHAPTER 2

THE DARK MATTER PROBLEM

In the last chapter I discussed how TeV astronomy is just developing to the point that new observatories are sensitive to the important TeV energy radiation processes in the Galaxy and the Universe. Besides the expected gamma-ray sources such as supernova remnants, the most exciting possibility is that these new instruments could observe processes that are completely unknown. In other words when we look out with new eyes, we may see something surprising and revolutionary. In this chapter I discuss the evidence that the Universe is composed of some unknown type of matter. We do not understand the matter content of the Universe, and this new window on the Universe at TeV energies may allow us to see radiation from the unknown component of matter that makes up the Universe.

The matter in the Universe is composed of 20% normal baryonic matter and 80% nonbaryonic dark matter of unknown composition. This is the standard interpretation in cosmology of the various measurements that have been made of the Universe. In this chapter I will examine some of the evidence that leads to this conclusion. This examination will use the historical evolution of the important measurements to illustrate the role these measurements play in cosmology. The physics described here is rich, and my treatment is brief. A full dissertation could be written on any of these topics. I will try to explain two experimental results besides the measurements of stellar dynamics, the first dataset where dark matter is implied. The standard cosmological model requires a large amount of cold dark matter in order to reproduce the observed anisotropy in the relic microwave background and the relationship of luminosity distance to redshift.

Measuring the masses of galaxies and clusters gave the first evidence for signifi-

cant amounts of dark matter. With cosmological measurements starting around the same time, it became clear in the last part of the century that the dark matter is a significant part of the energy density of the Universe. The theory of the Big Bang, along with our knowledge of particle and nuclear physics, gives us a natural way to theoretically compute the expected abundances of the elements in the Universe. Coupled with theories of stellar evolution, we can predict present day chemical composition of the Universe. These predictions agree with observations and they give a theoretical basis for the amount of baryonic matter in the Universe.

2.1 Mass Measurements

Observing the rotations of galaxies and galaxy clusters began in the late 1930s. Zwicky was the first to develop the theory of measuring mass distributions by observing the dispersion in the velocities of orbiting objects. This theory can be derived from the virial theorem. In addition he used the powerful arguments of statistical mechanics to make a more exact measurement. When applying his method to the Coma cluster he noticed that the mass profile seemed to extend far beyond the visible matter. Around the same time Babcock measured the rotation of the Andromeda galaxy and also noticed that the rotation was flat at the largest radii of the survey. These early studies did not take into account the dark baryonic matter that was later observed to exist in the form of gas throughout the Universe. Furthermore, Babcock's measurement did not extend far enough out in the Andromeda galaxy. At the distances he measured the bar rotation of the galaxy could make the flat rotation curve he observed.

Zwicky considered a simple picture of a galaxy as a collection of dust. If the galaxy were an ideal gas, the particles would pass by each other without interacting, and the dynamics should depend on the gravitational force. The trajectory of a given particle should depend only on the mass enclosed by the orbit and so the mass profile of the collection of particles can be measured by observing the trajectories of the orbiting particles. Most of the stars in galaxies and galaxies in clusters orbit on time scales much longer than the time scale of astronomy, but statistical methods

can be used to measure the mass profile.

Instead of imagining a galaxy as an ideal gas, consider our gas to have a high viscosity. Under this assumption the galaxy will rotate as a solid object. The rotation velocity should increase $\sim r^2$. Zwicky argued that a galaxy can be thought of as a mixture of these two extremes, with a high viscosity in the central region and just free particles in the outer regions of the galaxy. The velocity dispersions are expected to rise with galactocentric radius then flatten and finally drop off outside the mass concentration. Babcock's measurement of M31 did not show the expected drop off at large radii. His measurement extended to ~ 6 kpc, which Zwicky argued was not far enough to see the drop off. Although the evidence of galactic DM was questionable, Zwicky found significantly more mass in the Coma cluster than was expected.

Improvements in radio astronomy in the early seventies made it possible to measure rotation curves with the *HI* line. These studies, such as [37], again on the rotation of M31 but this time out to 30 kpc, showed that the mass to light ratio in the outer regions of the galaxy increased to ~ 100 . Around this time it was proposed that galactic rotation curves could be explained by embedding the galaxies in a massive dark halo [38]. The actual distribution of this dark mass and the nature of the particles that make up this energy field are still unknown and actively studied.

As observers count more of the dust and other, less luminous, matter in the Universe, the discrepancy between Newton's gravity and astrophysical dynamics does not disappear. Some postulate that the dark matter is just normal matter in some unseen form, but there is more evidence today that dark matter is the second largest component of the energy content of the Universe. Dark matter has become key ingredient in modern cosmology.

New measurements of weak gravitational lensing will give more information on the amount and spatial distribution of dark matter. This method does not need any luminous matter to be observed and so otherwise invisible clumps of dark matter could be detected through this method.

2.2 Hubble's Law and the Big Bang

Hubble's Law is the statement that there is an increase in the outward velocity of objects with their (luminosity) distance away from us [39]. This relationship is not true for close-by objects such as the Sun or Andromeda where the objects are gravitationally bound together. However, for objects outside our local cluster of galaxies, everything is redshifted. There are two interpretations possible for this relationship. Either everything is moving radially outward from the Earth with the outward velocity increasing with distance, or everything in the Universe is roughly stationary, but the Universe is expanding. Under the assumptions of homogeneity and isotropy, the expanding Universe is the only interpretation. Hubble measured the expansion of the Universe and so this redshift-luminosity relationship is called Hubble's Law.

The first cosmological measurement was the observation that the redshift for all astrophysical objects increase with the distance to the object [40]. Redshift is defined as the increase in the wavelength of observed light λ_0 compared with the wavelength of the light when it was emitted λ_e as

$$z \equiv \frac{\lambda_0 - \lambda_e}{\lambda_e} \quad (2.1)$$

The fact that there were almost no galaxies blue-shifted was remarkable and unexpected. Redshift is commonly seen when a light producing source is moving away from the observer at a speed v as

$$z = \frac{v}{c} . \quad (2.2)$$

The interpretation of these data was driven by the new theory of General Relativity. Three simple discrete metrics can describe a space under the assumptions of homogeneity and isotropy. From Einstein's equation, if we specify the types and quantity of matter in the Universe, we can recover the evolution of a model Universe.

If the Universe is expanding and cooling as far back in time as we can see, then we come to the idea that the Universe was hot and small and all of the points were

infinitely close together. This is one piece of evidence that the Big Bang, that the Universe started as an expanding plasma, is the best description of the birth of the Universe.

2.3 The Standard Cosmology

Cosmology is an elegant branch of physics. From very simple assumptions, homogeneity and isotropy, a picture of the evolution of the Universe starts to form. As we look around the Universe appears to be expanding and cooling off. If we extrapolate backward in time the Universe gets smaller and hotter. This naturally leads to the picture of the Big Bang. At some time the Universe was small and filled with a hot, dense plasma of energy. As this plasma expands, the temperature will pass some critical energy scales. At the energy scale when photons and matter decouple, for example, the density fluctuations from this system freeze out. These fluctuations are expected to grow and form the large scale structures we observe today such as clusters and galaxies. The growth and morphology of these objects depends on the mixture of hot and cold matter in the Universe. When the temperature nears atomic energies, the elemental abundances will freeze out and will depend only on the density of the Universe at this time. This simple theory, along with the rules of particle physics, explains the physical structure and composition of the Universe.

The Cosmological Principle, that the Universe is isotropic and homogeneous, is the assumption after which the formalism of modern cosmology follows. In fact if modern cosmology would fail in describing the Universe, it would undermine this principle that is a fundamental concept in physics. Isotropy is the principle that the Universe looks the same in every direction. Homogeneity loosely means that the Universe looks the same from any observation point in the space. For more rigorous definitions, see, e.g., Weinberg [41]. Of course there are applicable scales for these concepts. If I look into the sky in the Summer I see a much brighter condensation of matter towards the Galactic Plane than I see out of it. Thus there is a cosmological scale under which these principles are assumed to be valid which

is much bigger than the scale of the Milky Way.

Given the Cosmological Principle, a metric is known to solve Einstein's equation. That metric, the Robertson-Walker-Friedmann metric, is

$$d\tau^2 = dt^2 - R^2(t) \left[\frac{dr^2}{1 - kr^2} + r^2 d\theta^2 + r^2 \sin^2\theta d\phi^2 \right]. \quad (2.3)$$

k is a constant that can take the discrete values $+1$, 0 , or -1 . For $k = +1$, this is the metric of a three-dimensional sphere embedded in four dimensions with a radius $R(t)$, which is called the radius of the Universe. For $k = 0$ the Universe is "flat" and the metric is cartesian. Finally with $k = -1$ the Universe is hyperbolic. For all of these metrics, $R(t)$ is the *cosmic scale factor* and describes the scale of the space geometry.

The evolution of the cosmic scale factor can be expanded about the present, t_0 . The time between the present and the time of the production of the light of the galactic redshifts can be assumed to be small and the scale factor can be expressed

$$R(t) \simeq R(t_0) \left(1 + H_0(t - t_0) + \frac{1}{2}q_0 H_0^2(t - t_0)^2 \right). \quad (2.4)$$

Here we have introduced the Hubble constant,

$$H_0 \equiv \frac{\dot{R}(t_0)}{R(t_0)}, \quad (2.5)$$

and the acceleration parameter,

$$q_0 \equiv -\frac{\ddot{R}(t_0)R(t_0)}{\dot{R}^2(t_0)}. \quad (2.6)$$

Hubble's measurements extended far back in the Universe enough to be sensitive only to H_0 . More recent measurements, supernovae data, are sensitive to distances large enough to measure q_0 . Historically q_0 is defined negatively and called the deceleration parameter.

For a light ray $d\tau^2 = 0$, so we get the equation

$$\frac{dt}{R(t)} = \frac{dr}{\sqrt{1 - kr^2}} \quad (2.7)$$

for a light ray coming towards us. We can integrate this expression from the point of emission, r_e , and the point of observation, 0 .

Estimating the distance to objects is the biggest problem in measuring these parameters. For close objects the parallax may be used, but with a Hubble constant of $\sim 100 \text{ km s}^{-1} \text{ Mpc}^{-1}$, Hubble's estimate, we would need to observe parallax on the order of μpc , which is still not possible.

In general relativity, evolution of the cosmic scale factor is governed by the Einstein equation, which can be written as

$$\left(\frac{\dot{R}(t)}{R(t)}\right)^2 = 1 - \sum_i \Omega_i \left(\frac{\dot{R}(t)}{R(t)}\right)^{\nu_i} - \Omega_\Lambda . \quad (2.8)$$

Equation 2.8 is also called the Friedmann Equation. This equation has a static solution at an energy density called the critical density. This is the density at which the Universe is a black hole so no energy may ever escape. More specifically, it is static when the right hand side of equation 2.8 is exactly equal to zero. Any less dense and the Universe would expand forever; any more dense and the Universe will collapse into a Big Crunch. This static solution is known to be unstable; any slight deviation from the critical density will drive the evolution of the total energy density away from the equilibrium value. Energy densities in cosmology are usually denoted in units of the critical density. For a particle χ the energy density would be written as $\Omega_\chi h^2 = \rho_\chi / \rho_c$ where $\rho_c = 3H_0^2 / (8\pi G)$. For historical purposes the Hubble constant is usually given in units of $100 \text{ km s}^{-1} \text{ Mpc}^{-1}$ and written as h .

The Hubble constant (H_0) was first measured using the variable cepheid stars. The intrinsic luminosity of cepheid stars is a known function of their variability timescale. Therefore the distance to the cepheid star can be determined by its observed brightness. Hubble made the first measurements of the redshifts of these objects [39]. The evolution of the redshift directly yields H_0 . Hubble's data were sparse, but indicated a value of $\sim 100 \text{ km s}^{-1} \text{ Mpc}^{-1}$. This is the origin of the traditional units for H_0 . More recently the acceleration of the Universe has been measured by projects such as the Supernovae Legacy Survey. Supernovae are brighter candles than cepheid stars and the luminosities of type Ia supernovae are thought to be well known[42]. These observations allow more knowledge of the evolution of $R(t)$.

The value of ν describes the difference in evolution between various types of energy. This can be derived from the other two fundamental equations in cosmology, the equation of energy conservation

$$\left(\frac{R(t)}{H_0}\right)^2 = 1 - \sum_i \Omega_i \frac{R(t)^\nu}{H_0} - \Omega_\Lambda . \quad (2.9)$$

and the equation of state

$$\left(\frac{R(t)}{H_0}\right)^2 = 1 - \sum_i \Omega_i \left(\frac{R(t)}{H_0}\right)^\nu - \Omega_\Lambda . \quad (2.10)$$

2.4 Cosmic Microwave Background

Observations of the Cosmic Microwave Background (CMB) have yielded a large amount of information on the different energy densities in the Friedmann equation. The CMB was first discovered in the 1960s by early radio astronomers. The CMB is the brightest background light in the Universe and is considered the best evidence of a Big Bang Universe. This radiation has the spectrum of a blackbody at ~ 2.7 K. The isotropy and spectrum of the CMB are interpreted as evidence that the entire Universe was once a hot plasma. For the isotropy in the CMB to make sense, all the points in the Universe must have been close enough to come into thermal equilibrium. COBE, a satellite launched in 1989, observed the CMB and found it to be isotropic to one part in 10000 after a dipole component is subtracted. The microwave anisotropy sky map is shown in Fig. (2.1). The dipole component is considered to be a measurement of the proper motion of the Sun through the Universe. Additional moments of the anisotropy were detected by COBE. Since the Universe is speculated to have been a thermal plasma at some point, the coupling between the matter and the radiation was much like that of a mass and spring. Through the moments of the anisotropy the total density and the relationship between Ω_M , Ω_R and Ω can be measured. The latest satellite to measure the CMB anisotropy was WMAP, launched in 2001. WMAP measured many cosmological parameters including the Hubble constant $h = 0.71$, the total matter density $\Omega_M = 0.135h^2$, the baryonic density $\Omega_b h^2 = 0.0224$, and the total energy density $\Omega = 1.02$



Figure 2.1. A representation of the data collected by DMR on COBE. These maps show the large dipole in the top image, which is taken as the best measure of the proper motion of the Sun with respect to the Universe. The middle map shows the dipole subtracted image before the Galactic Plane contamination is modeled and subtracted. In the bottom image the Galactic component is subtracted and the image is interpolated across the Galactic Plane. The anisotropy after dipole and Galactic Plane subtraction is less than one part in 10^4 . COBE also hosted FIRAS, which measured the temperature of the dominant blackbody spectrum to be 2.725 ± 0.002 K.

[43]. The fitting of a cosmological model to the WMAP data also includes the measurement of the CMB temperature by COBE [44], and additional measurements of the CMB anisotropy by CBI [45] and ACKBAR [46]. Finally the fitting also includes the 2dFGRS survey of the power spectrum of the local galaxy fluctuations. This remarkable result shows that we now think 80% of the matter in the Universe is nonbaryonic. This is some of the strongest evidence that the nature of the dark matter causing the flat rotation curves of galaxies and clusters, and gives the motivation for this dissertation, is made of some massive weakly interacting

nonbaryonic particles.

The rest of the dissertation is concerned with the possibility that these heavy particles could be annihilating in significant enough quantity to produce a flux of high energy particles, which could be seen with current astronomical measurements. The next chapter will cover the important parameters involved in calculating the flux of gamma rays from annihilation of massive particles.

CHAPTER 3

DARK MATTER ANNIHILATION

In Chapter 2 I discussed the observational evidence of dark matter. All the observations and the Big Bang theory fit together as long as they include this nonbaryonic ingredient of dark matter. Many new grand unification theories or extensions of the Standard Model predict new particles that would be only weakly interacting massive particles. It has been hypothesized that these particles could be a natural explanation of dark matter. If they have the correct particle mass, then they would have the correct relic density to explain the structure formation in the Universe. Other explanations of the dark matter are either rejected due to current measurements or they are so theoretical that differences between them and the standard dark matter paradigm are difficult to predict. In this chapter I will discuss some example models of particles that could annihilate and create high energy radiation.

3.1 Candidates for the Dark Matter

There are many theories to explain the observations of DM. There are baryonic possibilities, so called MAssive Compact Halo Objects (MACHOs) such as brown dwarfs and black holes. Another popular class of particles are the Weakly Interacting Massive Particles (WIMPs), usually yet undiscovered particles proposed or created while solving problems in physics. Another intriguing possibility is that we need to modify the theory of Newtonian Dynamics (MOND). Since this is the first test of Newtonian gravity at such large scales, this theory postulates the acceleration seen in the rotation curves is due to a lack of understanding of gravity. MACHOs have been mostly ruled out by observations such as gravitational lensing surveys.

WIMPs and MOND are exciting possibilities that would help expand our knowledge of physics.

MACHOs have been detected as a part of the DM. Three groups have measured gravitational microlensing by surveying millions of stars, either in the Galactic Bulge or in the Large Magellenic Cloud [47, 48, 49]. These surveys have been successful in finding MACHOs, but they usually find MACHOs to be a fraction of the baryonic matter. Furthermore, the observations of WMAP and the theory of Big Bang Nucleosynthesis point to an energy density of DM of $\Omega_{DM} = 0.22$, about 80% of the total matter density in the Universe.

Nonthermal relics of the Big Bang are a possibility for explaining the DM. These particles would not be in thermal equilibrium in the early energy plasma, but would be created through other mechanisms. The axion is probably the most popular nonthermal relic. This particle was first proposed to explain the strong CP problem in Quantum Chromodynamics (QCD). The QCD Lagrangian contains a term that predicts an electric dipole of the neutron. The best experimental limit on the neutron dipole is almost 10 orders of magnitude smaller than the natural QCD prediction. This is known as the strong CP problem. By introducing a new symmetry to QCD the dipole upper limit can be explained. The field created by this symmetry is the axion field, which could also solve the DM problem. The axion is also an example of what is called a “well-motivated” DM candidate; a particle from a theory that was created a priori to solve another problem in physics that was later shown to be a possible DM candidate.

Thermal relics of the Big Bang are popular candidates for the DM. First there are the so called hot DM. Known particles, such as photons and neutrinos, have been suggested as an important photons and neutrinos. The photon density has been measured across the electromagnetic spectrum and Ω_R has value of $\Omega_R = 0.0004$. Neutrinos are another DM candidate. Neutrino oscillations, implying at least one nonzero neutrino mass, have now been detected. The masses of these particles are constrained by the oscillation measurements as well as other laboratory experiments to be around an eV. The best limit on the total energy density of the neutrinos is

given by [43] explained in [50] as $\Omega_\nu < 0.0076$. Both photons and light neutrinos would freeze out as relativistic particle, so called hot dark matter. This limit is due to the fact that a larger amount of relativistic particles would wash out too many structures in the Universe.

Finally there are a class of thermal WIMPs with masses near the GeV-TeV scale that would have a freeze out density near that measured for the Ω_{DM} . This DM would be nonrelativistic during galaxy formation and so would not disrupt the structures that we know to have formed. Usually the observed density of DM is thought to be produced thermally as the Big Bang cooled off. Once the mean free path of the WIMP reaches a Hubble length then the particles freeze-out and decouple from the Big-Bang plasma. The thermal relic density reaches the proper value when the interaction cross-section is on the order of the weak scale.

One of the most studied WIMPs is the lightest neutral supersymmetric particle, the neutralino. Supersymmetry is a new space-time symmetry suggested by efforts to find a theory to unify the fundamental forces. The lightest neutral particle is a good DM candidate because all the energy that went into supersymmetric particles would decay into the lightest particle. This energy density could account for the missing DM and the relic density of some theories could match the observed nonbaryonic DM density.

In supersymmetry there are a large number of free variables. All particles that make up the Standard Model would have superpartners in supersymmetry. If the symmetry were exact then all of the superpartners would have the same masses as their Standard Model counterparts. Supersymmetric particles have not been discovered, so, if they exist, their masses are higher than the scales reached so far in laboratory experiments. For the superpartners to have higher masses, supersymmetry must be broken, and this symmetry breaking introduces 106 new free parameters beyond the Standard Model. This model with the minimum number of new particles is called the Minimal Supersymmetric Standard Model (MSSM).

3.2 WIMP Annihilation

The flux of photons produced by DM annihilation depends largely on four factors: the annihilation product's energy spectrum, the particle mass, the annihilation cross-section, and the density of the DM particles. The energy spectrum of the annihilation products, the annihilation cross-sections, and the particle mass can be calculated by making assumptions about the large number of variables in a general supersymmetric theory and then solving for the remaining variables. The resulting particle physics model is compared to current observational constraints from particle accelerators, direct searches, and the CMB data. The density profile of a dark matter halo has long been a subject of much debate in the literature. Theoretical astrophysical considerations and numerical simulations have been used to suggest a family of DM halo shapes that could exist. The annihilation flux is proportional to the square of the number density, and many of the suggested DM halo shapes formally diverge when the emission rate is integrated along the line of sight through the center of the halo. The annihilation flux in the center of the DM halo will dominate the flux from these divergent halos. Astrophysically the density profile is expected to flatten at small radii where infalling objects can sweep out the centers of the halos through dynamical heating, although adiabatic accretion onto massive compact objects in the centers may create density enhancements [51, 52, 53].

In order to understand the physical parameters important in annihilation, consider a small emitting volume dV at a distance ℓ from a detector of collecting area dA (orthogonal to the line of sight.) This volume subtends a solid angle $d\Omega$ as seen from the detector. Let dN_e be the number of photons emitted during a time interval dt from the volume dV . Assuming the emission is isotropic, a fraction $dA/(4\pi\ell^2)$ of the emitted photons is detected. Thus the number of detected photons in the same amount of time dt is

$$dN_D = dN_e \frac{dA}{4\pi\ell^2}. \quad (3.1)$$

Specifically, for WIMP annihilation ($\chi\chi \rightarrow \dots \rightarrow \gamma$), the number of photons emitted is

$$dN_e = \frac{1}{2} \frac{dN_{\chi\chi\rightarrow\gamma}}{dE} \frac{\rho^2}{m_\chi^2} \langle\sigma v\rangle dE dt dV. \quad (3.2)$$

Here $\langle\sigma v\rangle$ is the χ - χ annihilation cross-section times relative velocity, ρ is the WIMP mass density, m_χ is the WIMP mass, and $dN_{\chi\chi\rightarrow\gamma}/dE$ is the number of photons in the energy interval $[E, E + dE]$ produced per annihilation. The factor of 1/2 is because two WIMPs are required per annihilation, $\rho^2 \langle\sigma v\rangle dt dV/m_\chi^2$ is the number of WIMPs annihilating and $dN_{\chi\chi\rightarrow\gamma}/dE$ is defined per annihilation. The photon flux from dV per unit energy at the detector is

$$\frac{d\Phi}{dE} = \frac{dN_D}{dA dt dE} = \frac{1}{8\pi\ell^2} \frac{dN_{\chi\chi\rightarrow\gamma}}{dE} \frac{\rho^2}{m_\chi^2} \langle\sigma v\rangle dV. \quad (3.3)$$

When Eq. (3.3) is integrated along the line of sight, dV can conveniently be written in terms of the solid angle $d\Omega$ as $dV = d\ell \ell^2 d\Omega$. This leads to the usual formula for the flux per unit energy per unit solid angle,

$$\frac{d\Phi}{dE d\Omega} = \frac{1}{8\pi} \frac{dN_{\chi\chi\rightarrow\gamma}}{dE} \frac{\langle\sigma v\rangle}{m_\chi^2} \frac{dJ}{d\Omega} \quad (3.4)$$

where

$$\frac{dJ}{d\Omega} = \int \rho^2 d\ell \quad (3.5)$$

with the integral taken along the line of sight. We have written the solid angle $d\Omega$ explicitly in $dJ/d\Omega$ to stress that its units are (mass density)² × (length)/(solid angle), as follows from Eq. (3.4) and our derivation. This same quantity is denoted by $J(\psi)$ in the literature, e.g., [54].

For a source whose size R is small compared to its distance D , we can replace ℓ in Eq. (3.3) by the source distance and use cartesian coordinates centered at the source. We write the volume element $dV = dx dy dz$ where z is along the line of sight and x, y are transverse to the line of sight. To study the angular dependence of the signal, we integrate in z only and introduce the angles $\theta_x = x/D$ and $\theta_y = y/D$. In terms of these, Eq. (3.3) gives

$$\frac{d\Phi}{dE d^2\theta} = \frac{1}{8\pi} \frac{dN_{\chi\chi\rightarrow\gamma}}{dE} \frac{\langle\sigma v\rangle}{m_\chi^2} \frac{dJ}{d^2\theta} \quad (3.6)$$

where

$$\frac{dJ}{d^2\theta} = \int \rho^2 dz. \quad (3.7)$$

Eq. (3.4) can be integrated over a region \mathcal{R} of the sky to give

$$\frac{d\Phi}{dE} = \int_{\mathcal{R}} \frac{d\Phi}{dEd\Omega} d\Omega = \frac{1}{8\pi} \frac{dN_{\chi\chi\rightarrow\gamma}}{dE} \frac{\langle\sigma v\rangle}{m_{\chi}^2} \int_{\mathcal{R}} \frac{dJ}{d\Omega} d\Omega \quad (3.8)$$

When integrating over the whole source, Eq. (3.8) gives a total flux of

$$\frac{d\Phi}{dE} = \frac{1}{8\pi} \frac{dN_{\chi\chi\rightarrow\gamma}}{dE} \frac{\langle\sigma v\rangle}{m_{\chi}^2} \frac{1}{D^2} \int_{\text{source}} \rho^2 dV. \quad (3.9)$$

Comparing Eqns. (3.9) and (3.8) we define

$$\int_{\text{source}} \frac{dJ}{d\Omega} d\Omega = \frac{1}{D^2} \int_{\text{source}} \rho^2 dV \equiv J. \quad (3.10)$$

J has units of $(\text{mass density})^2 \times (\text{length})$.

This factorization separates the factors due to a particular particle theory, $\langle\sigma v\rangle$, dN/dE , and m , from the astrophysical parameter J . The spectrum of the emission will be a broad continuum from π_0 decay with a sharp cutoff near the mass of the annihilating particle. An example of this is shown in Fig. (3.1). For some models a spectral line is detectable at the particle mass. This line would be incontrovertible evidence of an annihilation signal. Furthermore the morphology of the signal could yield clues about the density profile J .

A positive detection of annihilation would allow the measurement of the particle mass from the spectral cutoff or line at energy E_c . Any lower limits on the spectral cutoff, E_{cut} , can be considered an upper limit on the mass of the annihilating particle. The spectrum would also be a measurement of dN/dE . So the flux level detected would be a measurement of $\langle\sigma v\rangle \times J$. A wealth of information about the annihilating particle would be revealed. Alternatively if no detection of gamma rays is made it is possible to limit the variables in Eq. (3.8). We can expect the annihilation interaction to be on the order of the weak scale or weaker so

$$\langle\sigma v\rangle \leq \langle\sigma v\rangle_w \sim 10^{-26} \text{cm}^3 \text{s}^{-1}. \quad (3.11)$$

Telescopes are sensitive to radiation only in a certain energy range. Gamma-ray telescopes that will be considered in this dissertation characterize their energy

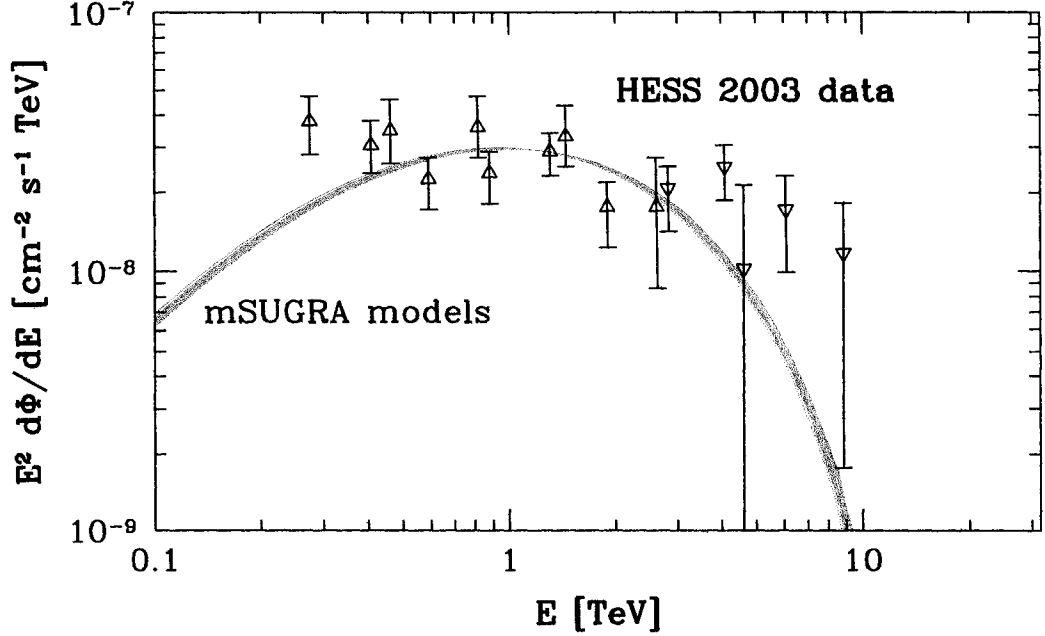


Figure 3.1. An example of a spectrum from WIMP annihilation [55]. These spectra are for 3 TeV and 10 TeV particles. The data shown is the flux from a gamma-ray observation of the galactic center discussed in chapter 3.

response by the energy threshold, E_t . These telescopes are sensitive to annihilating particles with masses above this energy, so the energy threshold can be taken as a lower limit for the particle mass in the absence of a detection. These considerations will lead to three possibilities for an upper limit for the density of annihilating particles. If the radiation is detected at flux level F with a cutoff and/or spectral line at E_c , the upper limit is

$$J \leq \frac{F E_c^2}{\langle \sigma v \rangle_w}. \quad (3.12)$$

If the source is extended beyond the point spread function of the telescope, then the angular dependence of the density profile, $dJ/d\Omega$ can be studied. If the cutoff or line is not detected, then E_{cl} can be substituted for E_c . Finally if no source is detected, we can calculate an upper limit for the flux, F_{ul} , and express the upper limit as

$$J \leq \frac{F_{ul} E_{cl}^2}{\langle \sigma v \rangle_w} \quad (3.13)$$

In this chapter we have shown the major evidence for the existence of a large amount of DM in our Universe. This large amount of DM influences the dynamics of galaxies and galaxy clusters. To model the DM we can imagine a spherical halo of weakly interacting massive particles that have been seen only through their gravitational influence on the baryonic matter. In order to explain the current data on the velocity dispersion of the stars and galaxies, the halo must extend out to the outermost data on these objects.

The flux of annihilation products depends on two astrophysical parameters, the distance and density of the particles. Physical parameters specific to the type of particle annihilating are its mass and annihilation cross-section. From basic considerations about WIMPs we can place an upper limit on the density of the particles if we know the distance to a particular clump of DM. This leaves gamma rays from dark matter annihilation as an important limit on the type and amount of dark matter.

CHAPTER 4

SOURCE SELECTION

In this chapter I discuss the process of selecting possible dark matter annihilation targets for TeV observations. As I discussed in Chapter 2, the expected flux from annihilation of a dark matter clump depends on two source specific parameters, the distance to the clump of dark matter and the density of the dark matter. For this search it is important to keep in mind that if we wish to explain the dark matter by some TeV radiation source, that this should be consistent between dark matter clumps. This may be the only way to conclusively prove or disprove the hypothesis that dark matter annihilation is a significant TeV radiation source.

The expected flux from WIMP annihilation is

$$\frac{d\Phi}{dE d\Omega} = \frac{dN}{dE} \frac{\langle\sigma v\rangle}{8\pi m_\chi^2} \frac{dJ(\theta, \phi)}{d\Omega}. \quad (4.1)$$

Here I used the WIMP model specific parameters the annihilation cross-section $\langle\sigma v\rangle$, the particle mass m , and the annihilation spectrum dN/dE . The source profile is related to the density profile through $dJ/d\Omega = \int dl \rho^2$ where integral is taken over the line of sight. This flux factorization shows the terms depending on the particle physics, separated from the astrophysical considerations that are contained in $dJ/d\Omega$. For a source small compared to the angular resolution of the detector at a distance D , the integrated J can be expressed as an integral over the volume of the source as

$$J \equiv \int_{\text{source}} d\Omega \frac{dJ(\theta, \phi)}{d\Omega} = \frac{1}{D^2} \int_{\text{source}} dV \rho^2. \quad (4.2)$$

This integrated J is a parameter that embodies the two astrophysical considerations for DM annihilation flux, the distance to the source and the density profile of

the DM particles. Close, dense DM clumps are therefore the best targets for observation. I choose to focus on the Local Group galaxies in order to compete with the D^{-2} factor in J . Additionally we tried to choose a variety of galaxy morphologies, because the baryonic matter in the galaxy can disrupt any DM cusp through heating. Black holes are expected to have a large effect on the inner regions of the DM profile. Adiabatic growth of a black hole can lead to a spike in the DM profile [51]. However, any large merging event between two supermassive black holes should wash out any cusp in the profile.

The DM density profile is important for the selection of targets. Each DM profile must be estimated from experimental measurements and theoretical considerations. The history, size, and baryonic content of each potential target can have an impact on the expected DM density profile, so we discuss each object individually. In general, I tried to cover a range of distances, sizes, and morphologies.

4.1 The Galactic Center

The Galactic Center (GC) has been proposed for observations of DM annihilation [56, 57, 58, 59, 54, 51, 60, 61] because it is close and might have a dense concentration of dark matter, thus a strong signal of gamma rays. After tentative detections of a TeV gamma-ray flux from the GC by the VERITAS collaboration [62] and the CANGAROO collaboration [63], the HESS collaboration [64] has initiated observations of the GC. HESS has reported a steady excess of TeV gamma-rays from the GC during two observational periods of 4.7 hours and 11.8 hours (at the 6 sigma and 9 sigma levels, respectively). This excess of gamma rays is confined to a region of 3 arcminutes centered around Sagittarius A*, the dynamical center of the galaxy which is believed to host a supermassive black hole [65]. The spectrum of this excess is a power law ($\frac{dF}{dE} \sim E^{-\alpha}$) with $\alpha = 2.2 \pm 0.2$ in the energy range [0.2, 8.8] TeV [66]. This spectrum is harder than typical gamma-ray sources such as plerions and active galactic nuclei. However, many of the newly discovered supernova remnants have similar spectra [67, 68].

The GC gamma-ray flux may be produced by a variety of mechanisms [69, 70,

71, 72]. For example, the central four million solar mass black hole could produce the gamma-ray flux by accelerating electrons in an extreme advection-dominated accretion flow. There is a high rate of supernovae near the GC and the shock fronts could accelerate particles to TeV energies. Alternatively it could be due to DM annihilation. The GC has been suggested as a possible site of enhanced DM annihilation [51, 52, 53, 73, 74] because it has a large stellar cusp and a million solar mass black hole in the center. The minimum radius to which any central dark matter density features extend is a key unknown in predicting the gamma-ray flux from WIMP annihilation. The interpretation of the photon flux from the GC is not settled and could lead at the very least to another example of an extreme particle accelerator, and possibly could shed light on the dark matter problem.

4.2 Dwarf Galaxies

Dark matter rich Milky Way satellite dwarf spheroidal galaxies are favored due to their proximity, their high mass to light ratio (as high as ~ 100), and their low gamma-ray background. The dynamical time of the galaxy nuclei, approximately the time for a star to cross the core, is comparable to the Hubble time for these galaxies. The DM elastically colliding with itself, instead of the usual ideal gas assumption, could give an explanation of the relaxation in some of these galaxies. If the DM is noninteracting the cores of these galaxies would not evolve within the Hubble time. Of the five known northern dwarf spheroidals, I chose Draco and Ursa Minor because they have the highest M/L ratio and they do not appear to be tidally disrupted.

One main advantage of these smaller galaxies as opposed to the GC is the density of these smaller halos is found to be higher in simulations due to their earlier production epochs. Dark matter in dwarf spheroidals has been intensively studied in the optical wavebands [75, 76]. These galaxies are the big brothers of globular clusters. The main formation scenario for both objects is violent relaxation [77]. Unlike spiral galaxies, which are believed to be formed by mergers, dwarf spheroidals are believed to be relics, frozen out early in the Big Bang scenario.

These 'subhalos' remain relatively undisturbed throughout history, although tidal forces from larger galaxies may be significant. Since the Universe was denser at the time these galaxies formed, as compared to large spiral galaxies, the density of the dark matter is expected to be higher.

Draco has been a favorite target for DM annihilation. Tyler [78] suggested that EGRET observations of Draco severely constrain the parameter space of SUSY. The CACTUS telescope recently claimed a tentative detection around 100 GeV; however, their new analysis does not seem to show a significant excess. For detailed discussions see [79, 80].

The distance to the core of Draco is measured to be 76 ± 6 kpc by Bonanos et al. [81] using variable stars. It has the highest M/L ratio of any Milky Way dwarf spheroidal. Of course, this number for dwarf spheroidals is model dependent due to the meager density of stars to measure. Kleyna et al. [76] measured the radial velocity dispersion of giant stars in Draco. Draco appears to have a mean $M/L = 330 \pm 125$ [76] within three core radii $r_c = 9.7' = 214pc$ [75]. Kleyna et al. find the rotation curve is flat or slightly increasing away from the core. The best fit DM halo profile is a nearly isothermal sphere of DM with a total mass of $8_{-2}^{+3} \times 10^7 M_\odot$.

Ursa Minor is an intriguing galaxy, similar to Draco in many physical aspects. The distance to Ursa Minor is 69 ± 4 kpc as measured by Mighell et al. [82]. Ursa Minor has clear substructure observed in the inner $\sim 10'$ [83]. The existence of this structure and an associated second population of stars is a mystery as this structure should only exist for a few hundred million years based on observations of stellar proper motions [84]. However, Kleyna et al. [85] show that this substructure could survive for the 10^{10} yr age of the galaxy if the halo has a constant density core. A detailed comparison of the observed astrophysical properties of Draco and Ursa Minor is discussed in [86].

Dwarf galaxies are compelling for gamma-ray observations of annihilation because the background is expected to be small. The density of stars in these dwarf galaxies is low, so the associated supernova rate and galactic cosmic-ray production

should be low as well. Thus, any signal detected from these galaxies would be a strong indication of dark matter annihilation. Bergstrom and Hooper [80] calculate the expected flux for Draco given the dispersion in the velocities of the stars and calculates a maximum flux from Draco of

$$F_{max} \simeq 2.4 \times 10^{-10} \left(\frac{100 \text{ GeV}}{m_\chi} \right)^2 \left(\frac{\langle \sigma v \rangle}{3 \times 10^{-26} \text{ cm}^3 \text{ s}^{-1}} \right) \left(\frac{N_\gamma}{10} \right) \text{ cm}^{-2} \text{ s}^{-1}. \quad (4.3)$$

This flux was derived using an NFW profile. Recent observations, however, support the idea that Draco has a cored inner profile [76]. For a cored isothermal halo, Bergstrom and Hooper [80] find that the maximum flux would be reduced by an order of magnitude.

The time allocation committee approved time on Draco and Ursa Minor for the 2002-2003 observing season. The total exposure on these objects is listed in Table (4.1).

4.3 M31-M33

The next closest satellite system, besides our own, is the Andromeda system. The first rotation curve of M31 is among the earliest evidence of DM on galactic scales [87]. Andromeda is a galaxy larger than the Milky Way at a distance of 785 ± 25 kpc [88]. M31 is massive, larger than the Milky Way, with a $10^7 M_\odot$ black hole in the center. Unfortunately, there is evidence that M31 is undergoing a merger with two distinct populations of stars and a double nucleus. This merging

Table 4.1. Source positions and total exposure time in hours with the telescope pointing at the selected potential sources. Both sets of exposure times are in hours. The left set of times is the total exposure in ON and OFF modes. The right set of times is the total exposure after quality selection cuts described in Chapter 6. Θ is the average zenith angle for the observations in degrees.

Source	RA	Dec	T_{ON}	T_{OFF}	T_{ON}	T_{OFF}	Θ
Draco	17 20 14	+57 55	14.5	7.5	10.3	5.6	28
Ursa Minor	15 09 10	+67 13	18.4	8.4	7.0	7.0	36
M32	00 42 00	+40 52	10.3	9.3	8.9	8.9	13
M33	01 33 51	+30 39	18.6	9.1	8.7	8.7	18

process should wash out any cusp in the DM density profile so M31 was not chosen for this survey.

M32 is the closest compact elliptical galaxy and it is bound closely to M31. Stellar velocities as well as gas dynamics measure a single supermassive compact object, $\sim 3.6 \times 10^6 M_{\odot}$, in the core of M32 [89]. This black hole could either enhance the DM annihilation rate due to adiabatic accretion, or it could wash out any DM enhancement if created by mergers of large black holes. Lauer et al. [90] use Hubble observations of the core of M31, M32, and M33 to suggest a density $> 2 \times 10^7 M_{\odot}$ in M32's core. The core of M32 appears relaxed and so it is a good candidate for structures such as DM spikes around the central black hole. M32 extends about $10'$ across the sky so any emission should be point-like.

M33 is a spiral galaxy at a distance of 809 ± 24 kpc measured using red giant stars [88]. The mass and density profile of the DM halo of M33 derived from rotation curves is well studied due to its proximity and orientation [91]. M33 does not have a large black hole in the center [92], which could suggest larger densities of DM if the formation of a supermassive black hole disrupts the halo. M33 has an angular size of $\sim 1^{\circ}$ so it is contained in the field of view, but it may be an extended source. However, most halos that would be visible with current sensitivities would be point-like. Lauer et al. [90] found in their study that the central density of M33 is about an order of magnitude less dense than the center of M32. They also found that the relaxation time is $\sim 3 \times 10^6$ yr, indicating a highly relaxed nucleus.

M32 and M33 were approved for observations by the time allocation committee for the Whipple Telescope in 2002-2003. Unfortunately, due to an operator error, the telescope was not pointed at M32 during this observing season. I applied for more time on M32 and received additional time in the 2004-2005 observing season.

CHAPTER 5

THE GALACTIC CENTER

The Galactic Center (GC) has been proposed for observations of DM annihilation [56, 57, 58, 59, 54, 51, 60, 61] because it is close and might have a dense concentration of dark matter resulting in a strong signal of gamma rays. After tentative detections of a TeV gamma-ray flux from the GC by the VERITAS collaboration [62] and the CANGAROO collaboration [63], the HESS collaboration [64] has initiated observations of the GC. HESS has reported a steady excess of TeV gamma rays from the GC during two observational periods of 4.7 hours and 11.8 hours (at the 6 sigma and 9 sigma levels, respectively).

In this chapter I will discuss the hypothesis that these gamma rays are due to dark matter annihilation. Additionally, I will show that there is additional information on the distribution of dark matter that could be responsible for these gamma rays from stellar orbit dynamics.

The GC gamma-ray source is confined to a region of 3 arcminutes centered around Sagittarius A*, the dynamical center of the galaxy which is believed to host a supermassive black hole [65]. The spectrum of this excess is a power law ($\frac{dF}{dE} \sim E^{-\alpha}$) with $\alpha = 2.2 \pm 0.2$ in the energy range [0.2, 8.8] TeV [66]. This spectrum is harder than typical gamma-ray sources such as plerions and active galactic nuclei. However, many of the newly discovered supernova remnants have similar spectra [67, 68].

The GC gamma-ray flux may be produced by a variety of mechanisms [69, 70, 71, 72]. For example, the central 4 million solar mass black hole could produce the gamma-ray flux by accelerating electrons in an extreme advection-dominated accretion flow. There is a high rate of supernovae near the GC and the shock fronts could accelerate particles to TeV energies. Alternatively it could be due to

DM annihilation. The GC has been suggested as a possible site of enhanced DM annihilation [51, 52, 53, 73, 74] because it has a large stellar cusp and a million solar mass black hole in the center. The minimum radius to which any central dark matter density features extend is a key unknown in predicting the gamma-ray flux from WIMP annihilation. The interpretation of the photon flux from the GC is not settled and could lead at the very least to another example of an extreme particle accelerator, and possibly could shed light on the dark matter problem.

In this chapter I consider the DM interpretation of the GC gamma-ray emission and study if any more information on this hypothesis is contained in the dynamical measurements of the mass profile at the GC. Advancements in infrared astronomy are testing the small scale mass profile of the center of the Milky Way, down to tens of AU. With the W.M. Keck 10 m telescope, proper motions of stars have been monitored near the GC since 1996 [93, 94, 65]. Entire orbits have been or will soon be measured around the dynamical center of the galaxy. A strong gamma-ray signal from the GC implies a large amount of DM under the WIMP annihilation hypothesis. The change in mass enclosed in a sphere with radius d , the distance from the GC to the star, changes as the stars, on highly elliptical orbits, traverse any central spherically symmetric density enhancement of the dark matter. This could lead to an observable deviation of the orbit from a purely Keplerian orbit. These observations provide direct constraints on the DM density profile in the center of the Milky Way and help us interpret the gamma-ray flux from the GC.

I use the data on the stellar orbits around the GC published in [95]. More recent data, including the complete orbital shapes, may provide further constraints [96]. I find that the gamma-ray flux from the GC is compatible with annihilation of a heavy, ~ 10 TeV, DM particle with a density profile consistent with the stellar orbits near the GC. Depending on the particle physics assumptions, the stellar orbits constraint is comparable but slightly stronger than the constraint on the source extension due to the angular resolution of HESS. Gamma-ray observations could have a very strong signature of WIMP annihilation due to the process $\chi\chi \rightarrow \gamma\gamma$, which would create a monochromatic line in the energy spectrum at the mass of

the annihilating particle. Unfortunately, I find that for a TeV neutralino the flux of the monochromatic line is too weak to be seen with an energy resolution of 10%, the resolution of the atmospheric Cherenkov method.

5.1 Particle Model Examples

Particle physics enters the gamma-ray flux through the combination

$$\frac{dN_\gamma}{dE} \frac{\langle\sigma v\rangle}{m_\chi^2} \quad (5.1)$$

in Eq. (3.3). It is possible to estimate values for $\frac{dN}{dE}$, $\langle\sigma v\rangle$, and the particle mass m_χ in examples of WIMPs. Once these values are given in a specific model, the resulting normalization required to fit the spectrum to the HESS flux gives a value for J . Varying the model parameters results in a band of J values.

I use here three examples of WIMPs: the lightest neutralino in minimal supergravity (mSUGRA), the lightest neutralino in a generic minimal supersymmetric standard model (MSSM), and a Kaluza-Klein (KK) dark matter particle [71].

To explore mSUGRA models, I used the program DarkSUSY [97] to find model parameters consistent with particle accelerator and direct search bounds. The spectrum of gamma rays extends up to ~ 9 TeV and any WIMP annihilation that would explain the observation would require a particle with a mass above 10 TeV. In mSUGRA excessive thermal relic densities are predicted for most neutralinos with such a high mass. However, changing the cosmological model may alleviate this difficulty [98], so I proceed without imposing the usual relic density constraint. I fit the normalization of the spectra to the HESS data. The results are shown in Fig. (5.1). The two physical processes included in this spectrum are secondary pion decay and direct annihilation into photons. The spectral line due to direct photon production is not observable in the spectrum after it has been convolved with the HESS energy resolution of $\sim 15\%$. Other processes, especially the acceleration of charged secondaries, could be reasonably expected to alter the spectrum [71]. This could provide other signatures of the annihilation, which could be an important check on the DM annihilation interpretation of the HESS flux. I find that there is a family of mSUGRA models that produce a neutralino with a mass of 10 to 11 TeV

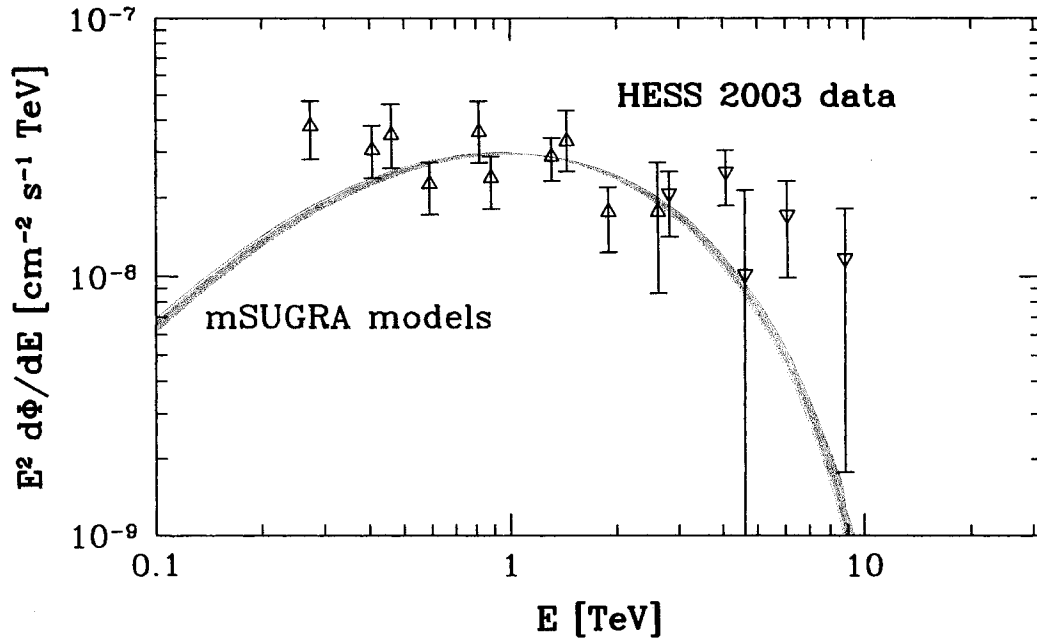


Figure 5.1. Minimal supergravity models of the annihilation flux fit to the 2004 HESS data. The grey band consists of several spectra generated with mSUGRA neutralinos of mass ~ 11 TeV.

consistent with current constraints and have a decent agreement with the HESS spectrum, with a χ^2 of ~ 1.2 . These models require the J parameter to be in the range [300,3000] BUBU to explain the flux observed by HESS.

Lower values of J may be obtained once the parameter space is relaxed beyond mSUGRA. The difficulty in finding mSUGRA models that fit the HESS data lies in the excessive thermal relic densities predicted for neutralinos with the required mass, ~ 10 TeV or higher. Profumo [99] has suggested that resonant annihilation of neutralinos through the A boson in the early Universe, which can occur for $m_A \simeq 2m_\chi$, can lower the relic density for particles around 10 TeV. In this case the value of J can be as low as ~ 1600 BUBU (see his Fig. (7b) obtained in an anomaly mediated supersymmetry breaking model) or even ~ 3 BUBU (see his Fig. 8b, for a generic MSSM model).

A third example of WIMPs that fit the HESS data is Kaluza-Klein (KK)

particles. These particles are predicted by many dimensional theories such as string theory. Ref. [71] finds that the spectrum for a model of KK DM requires a J value of ~ 130 BUBU in order to be responsible for the flux recorded by HESS.

5.2 DM Density Profile

A dark matter density profile that would explain the TeV gamma-ray flux from the GC with the particles discussed in the last section will need to have a higher than expected density. The HESS GC source does not extend beyond $\sim 0.1^\circ$ or ~ 10 pc, covering a solid angle $\Omega \sim 10^{-5}$ sr. The required J value from section 5.1 ranges from 3 – 3000 BUBU or a $dJ/d\Omega \sim 10^5 - 10^8$ BUBU sr $^{-1}$ for 0.1° or $\Theta \sim 10^{-3}$ rad.

The contribution from the extended DM halo along the line of sight to the GC can be estimated from Eq. (3.5) as $dJ/d\Omega \sim \rho^2 D$. For a canonical isothermal halo $\rho \sim 2\rho_{local} \sim 0.6$ GeV cm $^{-3}$ and $dJ/d\Omega \sim 4$ BUBU sr $^{-1}$ from the DM column through the extended DM halo. This is five to eight orders of magnitude smaller than required, so higher DM densities are needed to produce the gamma-ray flux by annihilation of our candidate DM particles.

A Navarro-Frenk-White profile (NFW) [100] is denser at the center. For an NFW profile, the average value of $dJ/d\Omega$ within 0.1° is, from Eq. (5.4) below,

$$\frac{dJ}{d\Omega} \sim \frac{1}{\Omega} \int_{\Omega} \frac{dJ}{d\Omega} d\Omega = \frac{2\pi\rho_s^2 r_s^2}{D\Theta} \sim 3 \times 10^3 \text{ BUBU sr}^{-1}. \quad (5.2)$$

This is still two to five orders of magnitude too small to explain the observed gamma-ray flux for most of the dark matter particles I consider. I conclude that, if the HESS signal is due to DM annihilation, the extended halo contributes no more than a few percent of the gamma-ray flux and a strong enhancement in the density must exist within 10 pc of the center of the galaxy.

The dark matter density profile within 10 pc of the GC is not known in detail and mechanisms for such density enhancements have been proposed. For example, such enhancement could be explained by extreme clumping of the dark matter [101, 102, 103, 104], which would have implications on models of structure formation, by steeper density profiles, $\rho \propto r^{-\alpha}$ with $\alpha \geq 3/2$, have been suggested [105]

but are disfavored, or by a strong dark matter concentration at the GC (a spike [51, 52, 53, 73, 74]). To include the latter two possibilities, I split the dark matter profile into an inner and an outer part at a transition radius R_I .

As an example of the outer profile I use the NFW profile

$$\rho_{\text{NFW}} = \frac{\rho_s}{\frac{r}{r_s} \left[1 + \left(\frac{r}{r_s} \right)^2 \right]}. \quad (5.3)$$

r_s is a scale radius and ρ_s is twice the density at r_s . I will take typical values [54] of $r_s = 25$ kpc and $\rho_s = \rho_0(D/r_s)[1 + (D/r_s)^2]$ with a local density $\rho_0 = 0.3$ GeV cm^{-3} . I take the distance to the GC to be $D = 8$ kpc [106]. For this profile I compute

$$\frac{dJ_{\text{NFW}}}{d\Omega} = \rho_s^2 r_s \left\{ \frac{\pi - \theta}{y} - \frac{3 + 2y^2}{2(1 + y^2)} \left[\arctan \left(\frac{z}{\sqrt{1 + y^2}} \right) + \frac{\pi}{2} \right] - \frac{z}{2(1 + x^2)(1 + y^2)} \right\} \quad (5.4)$$

where θ is the angle between the line of sight and the GC, $x = D/r_s$, $y = x \sin \theta$, and $z = x \cos \theta$.

Notice that Eq. (5.4) diverges in the direction of the GC ($\theta = 0, y = 0$) as $\pi \rho_s^2 r_s^2 / D\theta$. To remove the inner part of the NFW profile, I add an inner cutoff at R_I by replacing the term $(\pi - \theta)/y$ in Eq. (5.4) with

$$\mathcal{F}(y, z_c) + \mathcal{F}(y, b_c) - \frac{z_c}{(1 + y^2)(1 + x_c^2)} - \frac{3 + 2y^2}{(1 + y^2)^{\frac{3}{2}}} \arctan \left(\frac{z_c}{\sqrt{1 + y^2}} \right) \quad (5.5)$$

where $x_c = R_I/r_s$, $z_c = \sqrt{x_c^2 - y^2}$, $b_c = (zz_c + y^2)/(z - z_c)$, and

$$\mathcal{F}(y, a) = \frac{1}{\sqrt{a^2 + y^2}} {}_2F_1 \left(\frac{1}{2}, \frac{1}{2}; \frac{3}{2}; \frac{y^2}{y^2 + a^2} \right) = \frac{1}{y} \arctan \left(\frac{y}{a} \right) \quad (5.6)$$

The form with the hypergeometric function is used to avoid division by zero at $y = 0$ ($\theta = 0$).

In the inner ($r \lesssim 10$ pc) part of the density profile I use a simple functional form to model a central density enhancement. I assume that a DM mass M_I is contained

within a sphere of radius R_I , and that its density profile is spherically symmetric and decreases with a power α of the radius. The inner profile I use is

$$\rho_I(r) = \begin{cases} \frac{3-\alpha}{4\pi} \frac{M_I}{R_I^3} \left(\frac{r}{R_I}\right)^{-\alpha}, & R_c \leq r \leq R_I, \\ 0, & \text{otherwise.} \end{cases} \quad (5.7)$$

This inner profile could be a steep profile, or a spike around the central black hole. For this inner profile, I find

$$J_I = \frac{(3-\alpha)^2}{4\pi} \frac{M_I^2}{R_I^3 D^2} \frac{1}{3-2\alpha} \left[1 - \left(\frac{R_c}{R_I}\right)^{3-2\alpha} \right]. \quad (5.8)$$

Here R_c is an inner cutoff radius discussed in the next paragraph. For the angular profile I compute

$$j(\theta) \equiv \frac{1}{J} \frac{dJ(\theta)}{d^2\theta} = \begin{cases} \frac{1}{2\pi} \frac{3-2\alpha}{\theta_I^{3-2\alpha} - \theta_c^{3-2\alpha}} \left[\frac{\theta_I^{1-2\alpha}}{1-2\alpha} F\left(\alpha, \frac{\theta}{\theta_I}\right) - \frac{\theta_c^{1-2\alpha}}{1-2\alpha} F\left(\alpha, \frac{\theta}{\theta_c}\right) \right], & \theta < \theta_c, \\ \frac{1}{2\pi} \frac{3-2\alpha}{\theta_I^{3-2\alpha} - \theta_c^{3-2\alpha}} \left[\frac{\theta_I^{1-2\alpha}}{1-2\alpha} F\left(\alpha, \frac{\theta}{\theta_I}\right) - \frac{\theta^{1-2\alpha}}{1-2\alpha} \frac{\sqrt{\pi} \Gamma(\alpha + \frac{1}{2})}{\Gamma(\alpha)} \right], & \theta_c < \theta < \theta_I, \end{cases} \quad (5.9)$$

and zero for $\theta > \theta_I$. Here I defined $\theta_I = R_I/D$, $\theta_c = R_c/D$, and

$$F(\alpha, x) = \sqrt{1-x^2} {}_2F_1\left(\alpha, 1; \alpha + \frac{1}{2}; x^2\right) \quad (5.11)$$

where ${}_2F_1$ is the hypergeometric function. Notice that for $\alpha = 3/2$ the factor in front of the square bracket is $[2\pi \ln(\theta_I/\theta_c)]^{-1}$ and that for $\alpha = 1/2$ the square bracket is $\ln(\theta_I/\theta_c)$.

An inner cutoff at R_c is introduced to avoid the divergence that occurs in $dJ_I/d\Omega$ when $\alpha \geq 3/2$. This inner cutoff is left as a free parameter, because this part of the halo is even more unknown than the rest. Physically an inner cutoff would naturally be present. This cutoff could be the capture radius of the black hole, or some effective radius at which, e.g., the DM density is depleted by annihilation

during the history of the Milky Way. In the latter case the maximum sustainable density is usually taken as

$$\rho \leq \rho_{max} \simeq \frac{m}{\langle \sigma v \rangle t} \quad (5.12)$$

with the time t taken as the age of the Milky Way. In the case I am considering, there is a measurement of the flux and of the particle mass from the extent of the spectrum. For example, integrating Eq. (3.9) in energy above the threshold and inserting Eq. (5.7) with $\alpha = 0$, Eq. (5.12) implies

$$M_I \geq M_c \equiv \frac{8\pi D^2 m t \Phi}{N_\gamma}, \quad (5.13)$$

where Φ is the total photon flux above threshold and N_γ is the number of photons produced above threshold in each annihilation. Thus the maximum density ρ_{max} corresponds to a lower limit on the mass of an inner feature of the halo that could explain the gamma-ray observation. If the mass is too small, then the cross-section and density required to maintain the same flux are so large that the feature would have annihilated by now. This can be generalized to all α values by finding the R_c for which $\rho(R_c) \leq \rho_{max}$. They are any R_c greater than the solution for R_q in the equation

$$R = R_q \left(1 + \frac{M_c^2}{D^2 J} \frac{3 - 2\alpha}{4\pi R_q^3} \right)^{\frac{1}{3-2\alpha}}. \quad (5.14)$$

Another scale in this problem is the capture radius of a 3 million solar mass black hole, expected to be in the center of all of these profiles. I find that the capture radius, $\sim 10^{-7}$ pc, is greater than all R_q .

Thus, as a physically motivated number, I take the range of cutoff radii to be

$$10^{-7} \text{ pc} \leq R_c \leq R_I. \quad (5.15)$$

5.3 Limits From the HESS Angular Profile

The angular distribution of photons in the HESS detector carries information on the source profile. Here I investigate the constraint on the source profile due to these data.

The HESS analysis [66] assumes a gaussian source profile, and gives a limit on the source angular size equal to $\leq 3'$. To determine the limit on our power-law sphere in Eq. (5.7), I compare the emission profile, Eq. (5.9), with the angular distribution of detected photons. Fig. (2) in [66] gives the photon counts C_i and their errors δ_i in each θ_i^2 bin. Here θ_i is the angle between the photon direction and the center of the excess. The center of the excess agrees to the position of the GC to well within the systematic errors in the pointing of the HESS array. The intrinsic angular profile

$$j(\theta) = \frac{1}{J} \left[\frac{dJ_I}{d\Omega} + \frac{dJ_o}{d\Omega} \right] \quad (5.16)$$

is convolved with the point spread function (psf) of HESS as given in [72]:

$$f_{psf}(\theta) = f_0 \left[e^{-\frac{\theta^2}{2\sigma_1^2}} + \frac{1}{8.7} e^{-\frac{\theta^2}{2\sigma_2^2}} \right]. \quad (5.17)$$

Here f_0 was chosen so the psf has unit area and the widths of the gaussians are $\sigma_1 = 0.052^\circ$ and $\sigma_2 = 0.136^\circ$. I rewrite this as a linear combination of two normalized gaussians,

$$f_{psf}(\theta) = \frac{c_1}{2\pi\sigma_1^2} e^{-\frac{\theta^2}{2\sigma_1^2}} + \frac{c_2}{2\pi\sigma_2^2} e^{-\frac{\theta^2}{2\sigma_2^2}} \quad (5.18)$$

with $c_1 = 8.7\sigma_1^2/(8.7\sigma_1^2 + \sigma_2^2)$ and $c_2 = \sigma_2^2/(8.7\sigma_1^2 + \sigma_2^2)$. The source profile convolved with a normalized gaussian is

$$\bar{j}(\theta, \sigma) = \sigma^{-2} e^{-\frac{1}{2}(\frac{\theta}{\sigma})^2} \int_0^{\theta_{DM}} \theta' e^{-\frac{1}{2}(\frac{\theta'}{\sigma})^2} I_0\left(\frac{\theta\theta'}{\sigma^2}\right) j(\theta') d\theta' \quad (5.19)$$

and j convolved with the entire psf is

$$j_{psf}(\theta) = c_1 \bar{j}(\theta, \sigma_1) + c_2 \bar{j}(\theta, \sigma_2). \quad (5.20)$$

The photon counts $C(\theta)$ as a function of angle θ from the GC are proportional to the convolution of $dJ/d\Omega$ with the psf

$$C(\theta) = A \left(\frac{dJ}{d\Omega} \right)_{psf}. \quad (5.21)$$

The proportionality constant is given by

$$A = \mathcal{E} \frac{\langle \sigma v \rangle N_\gamma}{m_\chi^2} \frac{N_\gamma}{8\pi} \pi \Delta\theta^2, \quad (5.22)$$

where \mathcal{E} is the exposure, N_γ is the total number of photons above the experimental threshold emitted per annihilation, and $\Delta\theta^2$ is the aperture of the observation. I

have estimated the HESS exposure as the ratio of the total counts assuming a point source and the integral flux of $1.82 \times 10^{-6} \text{m}^{-2} \text{s}^{-1}$ above threshold, both as reported by HESS in [66]. I estimate an exposure $\mathcal{E} \sim 3 \times 10^{13} \text{cm}^2 \text{s}$. Furthermore,

$$\left(\frac{dJ}{d\Omega}\right)_{\text{psf}} = J j_{\text{psf}}(\theta). \quad (5.23)$$

The best fit for the normalization factor A is

$$A = \sum_i \frac{C_i J j_{\text{psf}}(\sqrt{\theta_i^2})}{\delta_i}, \quad (5.24)$$

with the χ^2 given by

$$\chi^2 = \sum_i \left(\frac{C_i - A J j_{\text{psf}}(\sqrt{\theta_i^2})}{\delta_i} \right)^2. \quad (5.25)$$

I take the probability distribution as proportional to $e^{-\chi^2/2}$ and find our confidence intervals in (α, R_1) by integrating this distribution.

The results of this piece of the analysis are shown in Fig. (5.2). The 68%, 90%, and 99% confidence regions in the R_1, α are shown. At the 90% confidence level the HESS data confine the source diameter to $\lesssim 1 \text{pc}$ for a uniform sphere. For power law density profiles with index $\alpha \gtrsim 1.5$ the constraint on the source size starts to weaken considerably; these profiles could be modeled as a smaller source with a harder power law index. Finally, I include a fit of two profiles in Fig. (5.3). The first, more shallow profile is an NFW profile alone. Evidently the flux rules out an NFW only DM profile, and so does the angular profile of the gamma-ray source. The steeper profile is a fit of an NFW profile with a spike. A spike can simulate a point source effectively, and the extended NFW piece makes the profile fit slightly better than a point source.

As an illustration of the kind of angular gamma-ray profiles compatible with the HESS data in models with a DM spike I show such a profile for an NFW model. I fix the halo NFW model with the parameters give in section 5.2. A pure NFW model does not fit the data well at small angles from the GC. However, motivated by [51], I add a spike with a radius of 1 pc and a slope of $\alpha = 1.9$, which are

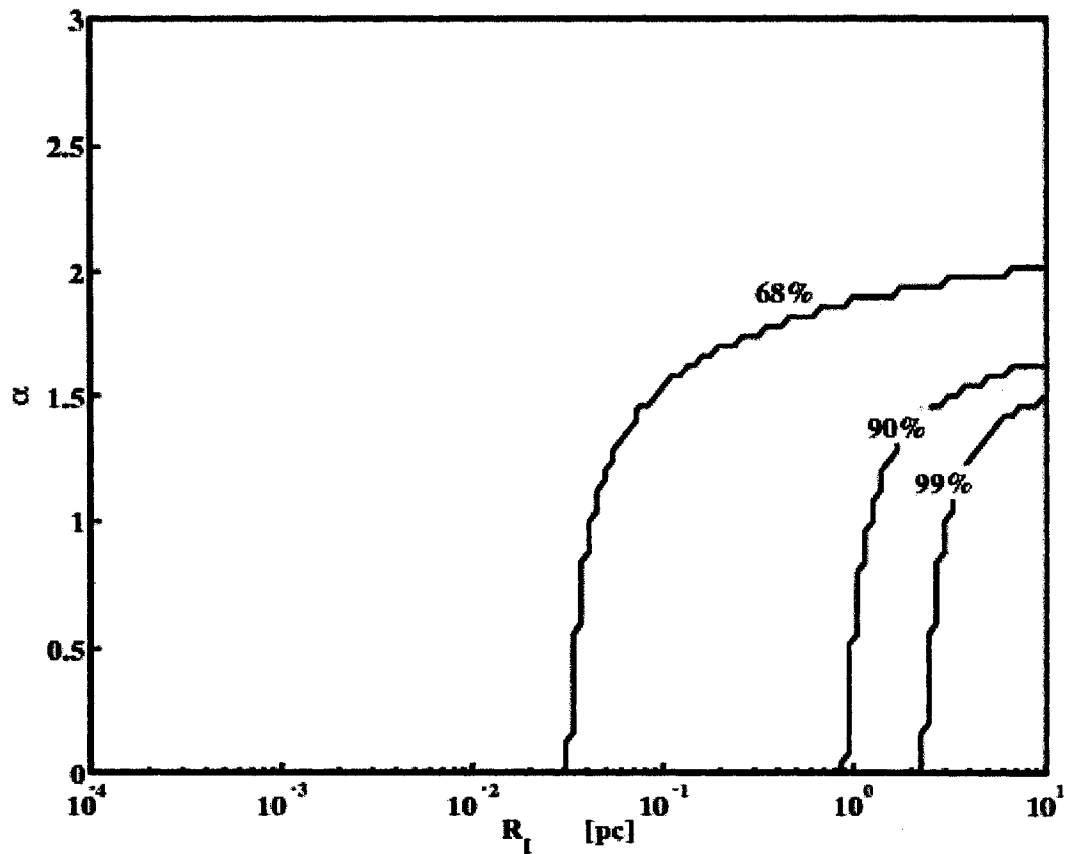


Figure 5.2. The constraint from the HESS angular size. The profiles are generally required to be steep, $\alpha > 1.5$, or small, $R_l < 1$ pc.

typical values after inclusion of the effects of stars and annihilation [74]. The χ^2 per degree of freedom for the fit is 1.3 which is the same ($\Delta\chi^2 \sim 10^{-4}$) as in the fit of a point-like source. Since the density of the dark matter is fixed by the local density and the particle mass is bounded by the spectrum, the normalization of the fit to the flux gives the value of the cross-section, $N_\gamma \langle \sigma v \rangle = 3.3 \times 10^{-28} \text{ cm}^3 \text{ s}^{-1}$. This is a reasonable value for the WIMP annihilation cross section in particle physics models.

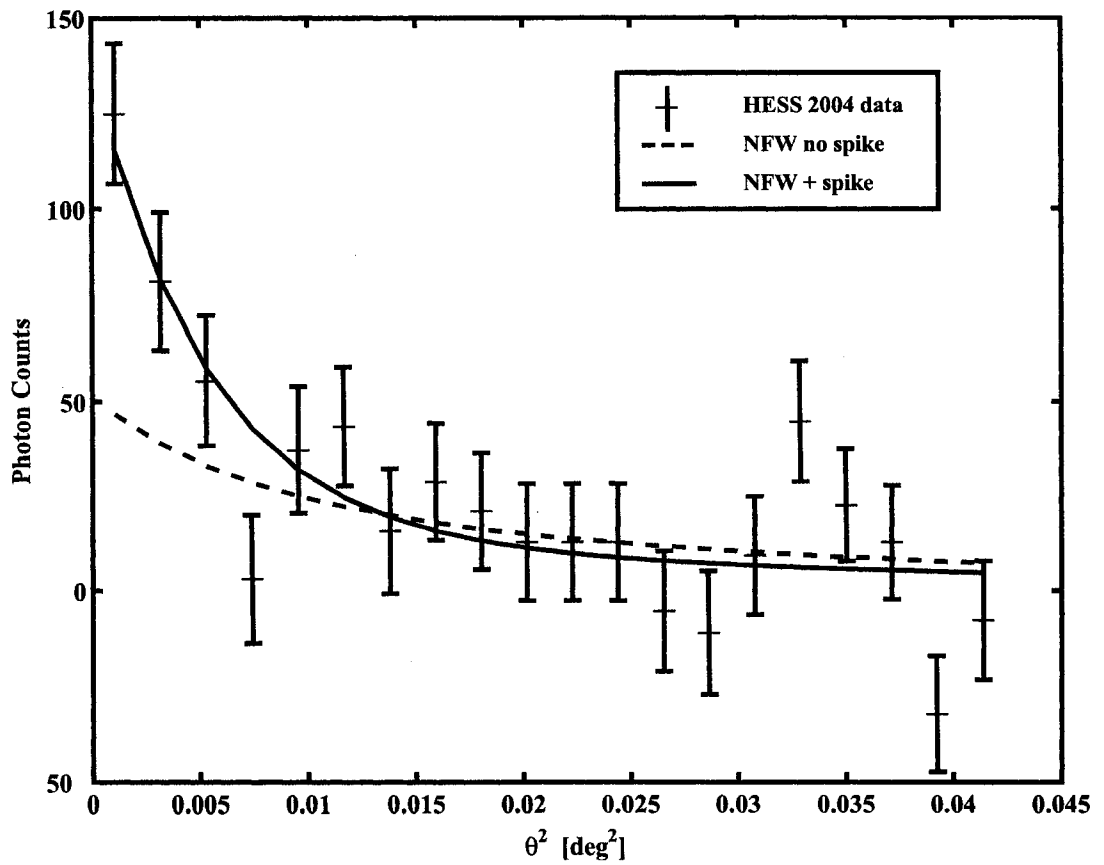


Figure 5.3. An NFW+spike fit to the 2004 HESS gamma-ray data on the GC. For this fit I used a NFW profile outside 1 pc and a $\rho \sim r^{-1.9}$ profile for $r < 1$ pc. An inner cutoff of 10^{-5} pc was used to approximate the inner core. This is a typical profile of a spike after dynamical heating and annihilation effects are included.

5.4 Limits From Stellar Dynamics

Here I examine how measurements of the mass $M(< r)$ contained within a distance r from the GC constrain the hypothesis that the GC radiation is due to DM annihilation. I use the compilation of enclosed mass measurements in [95] which were inferred from the observed proper motion of the stars in the GC. From their paper, I extract a table of the mass M_i contained within radius r_i , together with its quoted error σ_i .

To these data I fit a mass profile with three components: the central black hole,

the central stellar cluster, and the dark matter sphere described above.

$$M(< r) = M_{\text{BH}} + M_*(< r) + M_{\text{I}}(< r). \quad (5.26)$$

M_{BH} is the mass of the central black hole Sagittarius A*. For the central stellar cluster I use the empirical mass profile $M_*(< r)$ obtained from data in [107],

$$M_*(< r) = \begin{cases} M_* \left(\frac{r}{R_*} \right)^{1.6}, & r \leq R_*, \\ M_* \left(\frac{r}{R_*} \right)^{1.0}, & r > R_*, \end{cases} \quad (5.27)$$

with $M_* = 0.88 \times 10^6 M_\odot$ and $R_* = 0.3878$ pc. I model the dark matter with the density profile described in Eq (5.7), which corresponds to a DM mass profile

$$M_{\text{I}}(< r) = \begin{cases} M_{\text{I}} \left(\frac{r}{R_{\text{I}}} \right)^{3-\alpha}, & r \leq R_{\text{I}}, \\ M_{\text{I}}, & r > R_{\text{I}}. \end{cases} \quad (5.28)$$

I use the likelihood function to find constraints on the DM density profile. Assuming the errors quoted in [95] are gaussian, the likelihood \mathcal{L} is given by

$$2 \ln \mathcal{L} = \sum_i \frac{(M_i - M(< r_i))^2}{\sigma_i^2} = \sum_i \frac{(M_i - M_{\text{BH}} - M_*(< r_i) - M_{\text{I}} f_i)^2}{\sigma_i^2} \quad (5.29)$$

with

$$f_i = \begin{cases} \left(\frac{r_i}{R_{\text{I}}} \right)^{3-\alpha}, & r_i \leq R_{\text{I}}, \\ 1, & r_i > R_{\text{I}}. \end{cases} \quad (5.30)$$

In order to obtain a constraint on the parameters M_{I} and R_{I} at a fixed value of α , I first marginalize over M_{BH} . Since $\ln \mathcal{L}$ is quadratic in M_{BH} , I need only replace M_{BH} in Eq. (5.29) with the value M_{BH}^0 obtained by maximizing the likelihood. This is given by

$$M_{\text{BH}}^0 = \frac{x_3 x_4 - x_2 x_5}{x_3^2 - x_1 x_5}, \quad (5.31)$$

with

$$x_1 = \sum \frac{1}{\sigma_i^2}, \quad x_2 = \sum \frac{M_i - M_*(< r_i)}{\sigma_i^2}, \quad x_3 = \sum \frac{f_i}{\sigma_i^2}, \quad (5.32)$$

$$x_4 = \sum \frac{f_i [M_i - M_*(< r_i)]}{\sigma_i^2}, \quad x_5 = \sum \frac{f_i^2}{\sigma_i^2}. \quad (5.33)$$

As a prior, R_{I} is restricted to the range [0.0004,10] pc and distributed logarithmically, and α is kept at a few fixed values (0,1,2). By integrating the posterior

probability distribution I derive a one sigma upper limit and a 90% confidence interval in the M_I, R_I parameter space. For R_I smaller than the innermost data point (0.0004 pc), there is a degeneracy between M_{BH} and M_I . I break this degeneracy by imposing M_I less than the upper bound on the black hole mass reported in [95] ($3.6 \pm 0.4 \times 10^6 M_\odot$). This is equivalent to assuming all the mass within the innermost orbit could be DM.

5.5 Results

From the particle examples in Section 5.1 I find that a range of $J = [300, 3000]$ is needed to explain the flux of gamma rays from the GC as DM annihilation products. With resonant annihilations, J can be as low as ~ 1 . Furthermore I conclude that the DM annihilation line will be unobservable with an energy resolution of 10%. I find that the spectrum of gamma rays from the GC is compatible with the decay of pions produced in the annihilation. More complex models of the radiation, such as [71] where bremsstrahlung of W products has an appreciable effect, the spectrum may be similar to a power law and other spectral features, such as a hardening of the spectrum near the WIMP mass, may be observable.

The requirement that the central feature of dark matter not annihilate in the lifetime of the Universe gives a lower limit on the mass. For example, a central feature with $\alpha = 0$ and an upper limit on the density of $\rho = 10^{15} M_\odot \text{pc}^{-3}$ and the requirement that $J = 1000$ BUBU gives a lower limit of $\sim 3 \times 10^{-4} M_\odot$. For a limit density of $\rho = 10^{12} M_\odot \text{pc}^{-3}$ the mass of annihilating dark matter must be greater than $\sim 1 M_\odot$ to be stable for 10^{10} years. These limits are below the lower edge of our results plots.

The stellar dynamics limit extended mass distributions to $\sim 10\%$ of the black hole mass for $R_I = (10^{-3}, 1)$. The angular size bounds are complementary, excluding regions above a radius that depends on the assumed α for the distribution, as seen in Fig. (5.2).

In Figs. (5.4, 5.5, 5.6, and 5.7) I plot both the stellar dynamics bound and the angular size bound in the $M_I - R_I$ plane for three values of α . The expected range

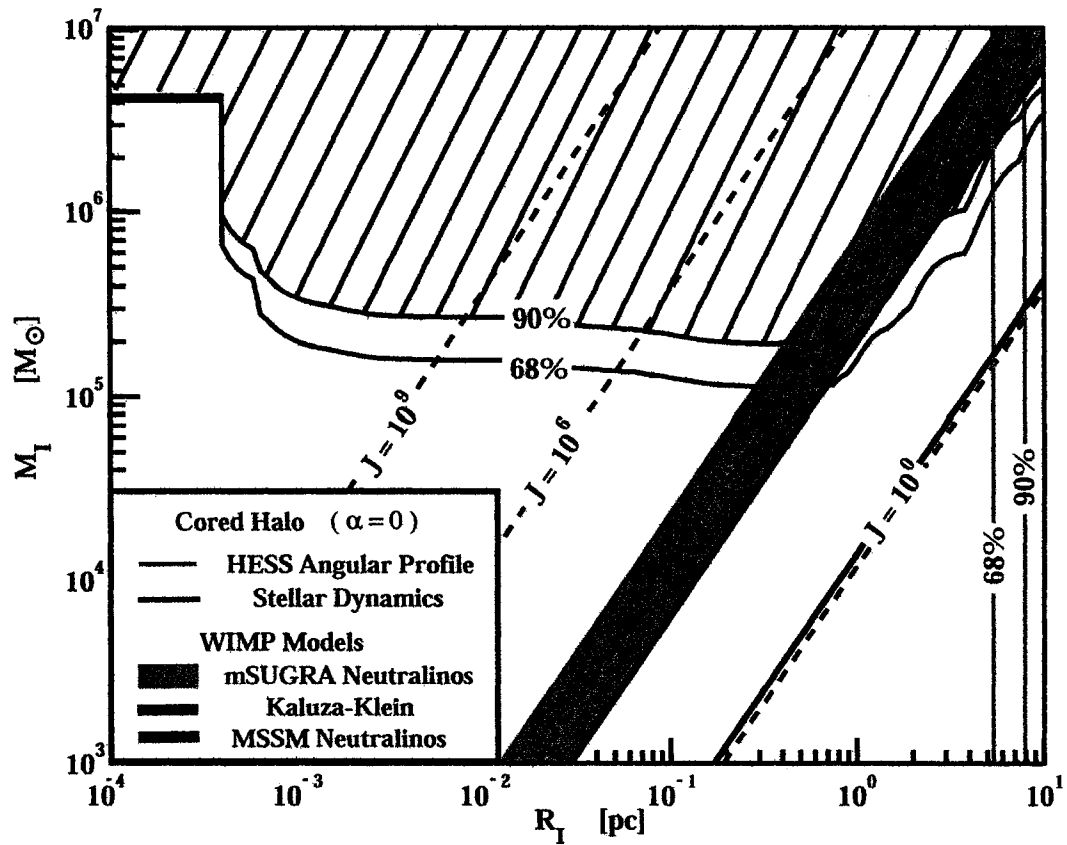


Figure 5.4. Stellar orbit constraints on the mass and size of a dark matter concentration at the GC. The black lines are the 1 sigma upper limit and 90% confidence interval for the mass of dark matter spheres with power law density profile index $\alpha = 0$. The dashed lines show the mass corresponding to the J values indicated (in BUBU). The 1 sigma and 90% bounds from the angular profile are shown as the vertical gray lines. The grey bands show the typical values of J required to produce the HESS flux in WIMP models: KK (dark grey), mSUGRA (medium grey), and MSSM (light grey)

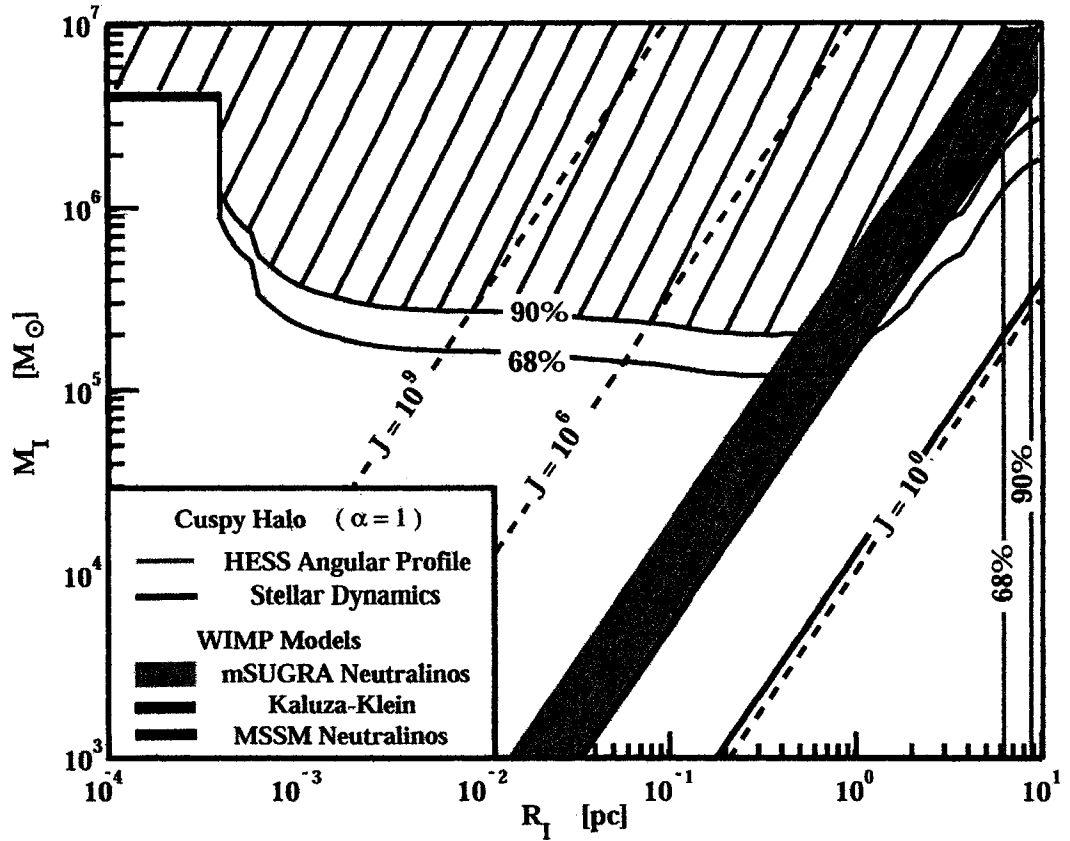


Figure 5.5. Stellar orbit constraints on the mass and size of a dark matter concentration at the GC. The black lines are the 1 sigma upper limit and 90% confidence interval for the mass of dark matter spheres with power law density profile index $\alpha = 1$. The dashed lines show the mass corresponding to the J values indicated (in BUBU). The 1 sigma and 90% bounds from the angular profile are shown as the vertical gray lines. The grey bands show the typical values of J required to produce the HESS flux in WIMP models: KK (dark grey), mSUGRA (medium grey), and MSSM (light grey).

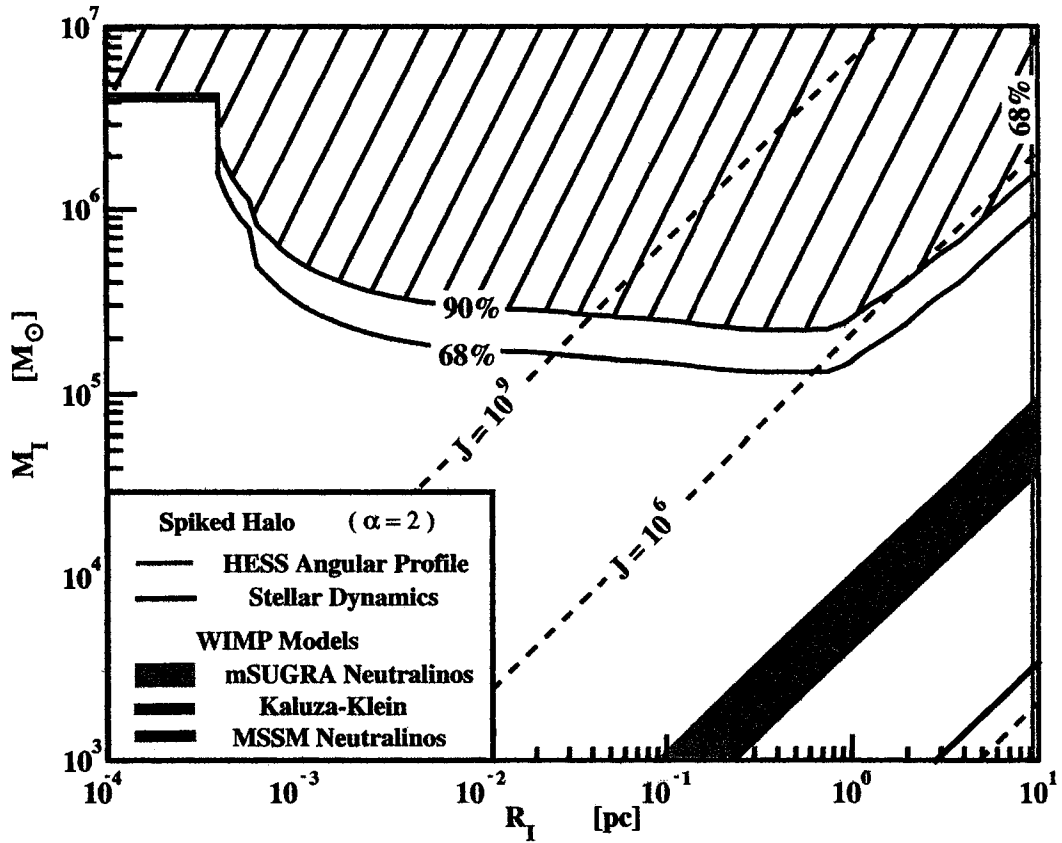


Figure 5.6. Stellar orbit constraints on the mass and size of a dark matter concentration at the GC. The black lines are the 1 sigma upper limit and 90% confidence interval for the mass of dark matter spheres with power law density profile index $\alpha = 2$. The dashed lines show the mass corresponding to the J values indicated (in BUBU). The 1 sigma and 90% bounds from the angular profile are shown as the vertical gray lines. The grey bands show the typical values of J required to produce the HESS flux in WIMP models: KK (dark grey), mSUGRA (medium grey), and MSSM (light grey). For this steep density profile, which “looks” like a smaller sphere, the size constraint on the DM feature is not as strong, constraining values of $J \sim 10^6$ BUBU or higher. To avoid a divergence in J and because these profiles are expected to flatten at some inner radius, this profile was computed with a minimum cutoff radius $R_c = 10^{-4}$ pc.

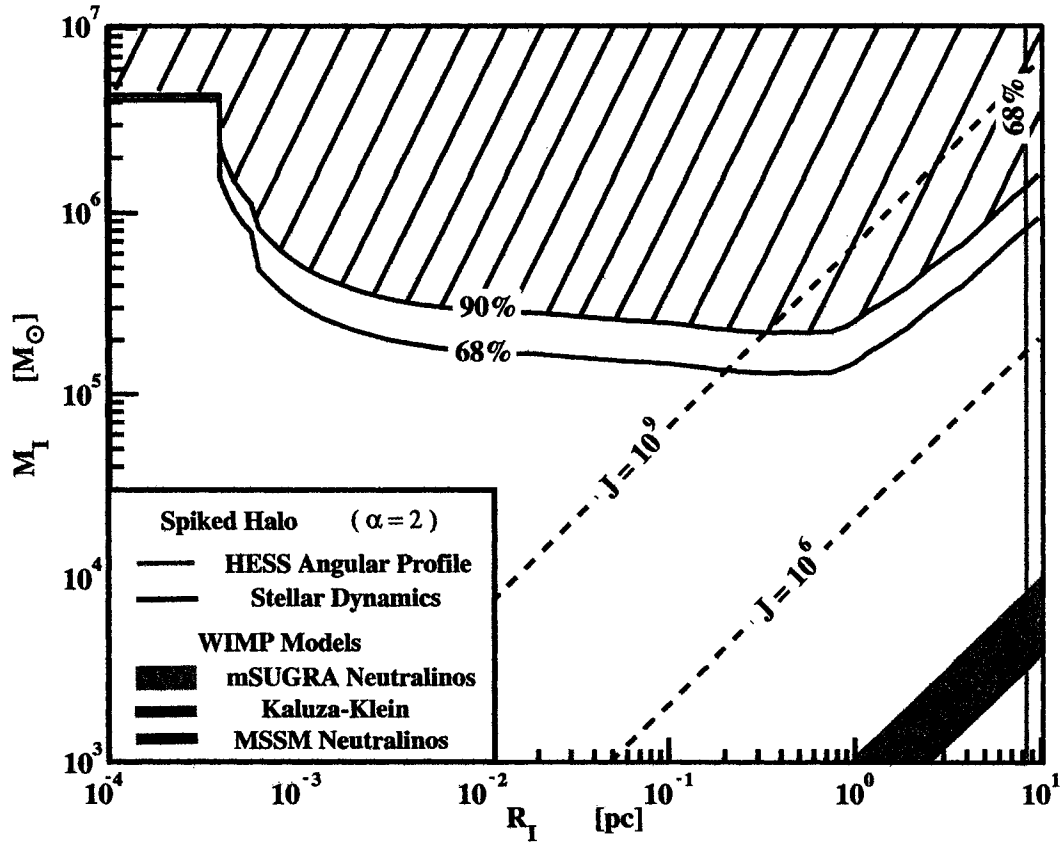


Figure 5.7. Stellar orbit constraints on the mass and size of a dark matter concentration at the GC. The black lines are the 1 sigma upper limit and 90% confidence interval for the mass of dark matter spheres with power law density profile index $\alpha = 2$. The dashed lines show the mass corresponding to the J values indicated (in BUBU). The 1 sigma and 90% bounds from the angular profile are shown as the vertical gray lines. The grey bands show the typical values of J required to produce the HESS flux in WIMP models: KK (dark grey), mSUGRA (medium grey), and MSSM (light grey). For this steep density profile, which “looks” like a smaller sphere, the size constraint on the DM feature is not as strong, constraining values of $J \sim 10^6$ BUBU or higher. To avoid a divergence in J and because these profiles are expected to flatten at some inner radius, this profile was computed with a minimum cutoff radius $R_c = 10^{-6}$ pc.

from the particle physics are shown as shaded regions. These regions correspond to either a value of J that could produce the observed flux, or equivalently to a value for $N\langle\sigma v\rangle$.

Comparing these models to our stellar dynamics bounds, the source size is restricted to $\lesssim 20$ pc for $\alpha = 0$ (Fig. 5.4) in mSUGRA and KK models. For larger cross-sections with resonant annihilation, the source size is unbounded by the stellar dynamics. The constraint from the HESS source profile limits the source size to $\lesssim 1$ pc (vertical line), so it is similar to the stellar dynamics constraint in mSUGRA and KK models, but is stronger for resonant-annihilation models. However, for some of the mSUGRA models I considered the stellar dynamics constraints were stronger restricting the source size to $\lesssim 0.3$ pc.

For profiles with shallow cusps ($\alpha = 1$; Fig. 5.5), the source size constraint on WIMP models from stellar dynamics is similar to the $\alpha = 0$ case. No bounds for resonant-annihilation models, but still $\lesssim 20$ pc for mSUGRA and KK models. The HESS constraint from the angular size of the gamma-ray excess is still ~ 1 pc and so conclusions similar to those with $\alpha = 0$ apply in this case.

For profiles with steep cusps ($\alpha = 2$; Figs. 5.6 and 5.7) stellar dynamics bounds out to 10 pc do not provide a constraint on the WIMP models I examined. The constraint from the HESS angular profile is also much weaker here. I show two plots here to illustrate the effect of the cutoff radius, which comes into play only for these steep profiles. I show two cutoff radii of 10^{-4} and 10^{-6} pc.

The constraints from stellar orbits and the HESS angular distribution are summarized for comparison in Fig. (5.8). The solid line represents the 90% confidence region based on the HESS data alone. The dotted lines show the constraint coming from stellar dynamics. Various values of J are plotted so that these constraints can be compared to particle physics models. The values of J required by the mSUGRA neutralinos, MSSM neutralinos, and Kaluza-Klein particles I examined are plotted as the medium grey band. Both the stellar dynamics and the gamma-ray angular profile point to a DM source that is either small or steep.

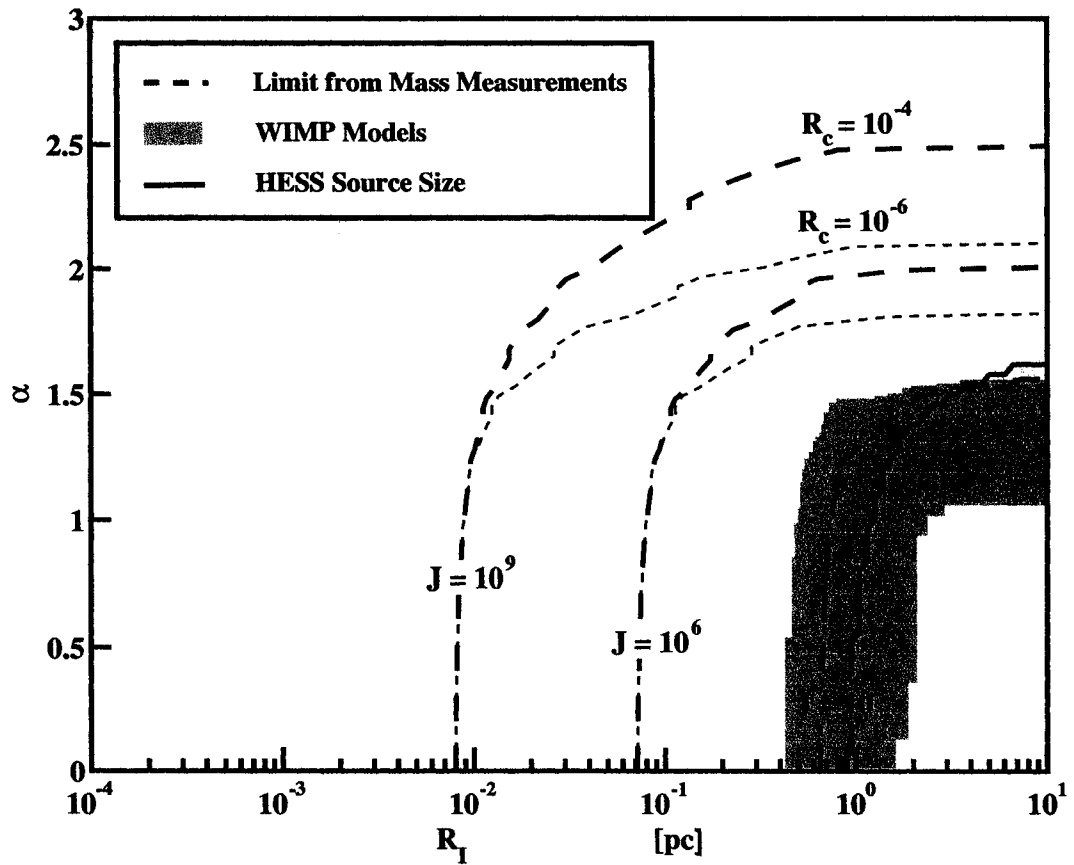


Figure 5.8. Constraints on the J parameter due to stellar orbit data [95, 107] and the HESS source profile. The dashed lines show the crossing of specific J values with the 90% confidence level from stellar orbit measurements as shown in Figs. (5.4, 5.5, and 5.6) for specific values of α . The 90% constraint on the source profile from the HESS data alone is shown as the solid line. The grey band is the expected range of J for mSUGRA neutralinos that produce the GC TeV flux.

CHAPTER 6

OBSERVATIONS WITH THE WHIPPLE TELESCOPE

In this chapter I report on an investigation with the Whipple Telescope. This chapter will give an introduction to the data and data analysis of four local group galaxies: Draco, Ursa Minor, M32, and M33. The observations are sensitive to radiation in the 300 GeV - 10 TeV energy range and were done with the Whipple Telescope on Mount Hopkins in southern Arizona. Here I describe the data and the different analyses that have been applied to these data.

6.1 The Data and Data Quality

The Whipple Telescope has a 10 m Davies-Cotton optical design [13]. The primary reflector consists of 248 hexagonal facets, composed of anodized and aluminized glass, each with a 61 cm diameter curvature. The camera consists of 490 photomultiplier tubes (PMTs) [108] with UV sensitive photocathodes. The inner 379 PMTs were used for this analysis covering a 2.6 degree field of view. The outer 111 PMTs had a larger diameter and therefore different noise and signal characteristics than the inner camera, and so were not used in the analysis. Additionally, the outer PMTs were removed from the camera during the 2003-2004, and the data set was split between two seasons spanning this downgrade of the camera.

The pixel signals are then amplified and subjected to a trigger system. A two-level hardware trigger system decides when to take a 25 ns exposure comprising the first level of the analysis. The number of exposures are reduced from the maximum rate of 40 MHz down to a sustainable rate of $\sim 20 - 30$ Hz. This hardware level trigger requirement reduces the amount of data and the complexity of the electronics needed to record the data.

An array of pixel triggers, one for each PMT, comprises the first level of the trigger system. This is implemented with constant fraction discriminators. These discriminators are used because they have a superior time resolution relative to simple threshold discriminators. The second level trigger, the pattern selection trigger, requires a time coincidence of ~ 5 ns between adjacent, usually three adjacent, discriminators triggering before a final trigger decision is sent to the data acquisition system. Once a trigger is initiated, the PMT signals, which have been delayed in a 120 ns cable, are then recorded with charge analog to digital converters.

The pixel trigger threshold, which sets the lowest energy air showers that will trigger the telescope data acquisition, is set using a bias curve. A bias curve is a measurement of the pattern trigger rate as a function of the pixel trigger threshold. The bias curve shows a break in the trigger spectrum when the accidental noise pattern trigger rate becomes less than the cosmic radiation trigger rate. The Whipple Telescope usually triggers at a rate of ~ 25 Hz on a clear night corresponding to a gamma-ray energy threshold of ~ 100 GeV at the pattern trigger level. Due to a large background of local muon events, the gamma-ray threshold is at least ~ 400 GeV after the subsequent software analysis. A more complete description of the Whipple standard operations is given by [109], [110], and [111].

There are five standard data runs taken during most nights with the Whipple Telescope. After the Sun is 15 degrees below the horizon, a nitrogen arc lamp is flashed at the camera for 1 minute in order to measure the relative gain between the pixels in the telescope. The high voltage on the PMTs is turned on approximately 30 minutes before this first calibration run to stabilize the individual pixel gains. After the nitrogen lamp relative calibration data are taken, the zenith run is usually taken. The zenith run is normally a 10-minute scan with the telescope pointed at zenith. The zenith run is used to measure both the stability of the total gain using the rate of the cosmic ray protons triggering the telescope and the relative gain of the telescope and data acquisition system between nights using the brightness of the highest energy cosmic ray protons that trigger the telescope. The zenith runs have also been combined to form a ~ 110 -hour survey of the sky at TeV energies

covering declinations of 31.2° to 40.2° at all values of right ascension [112].

After the nitrogen and zenith data are taken, the telescope goes into one of the three regular data taking modes: ON, OFF, and TRK. For ON and TRK observing modes, the telescope is pointed directly at the potential gamma-ray source. For OFF mode, the telescope is pointed to 30 minutes (RA) behind the source 30 minutes after the ON run in order to follow the same elevation and azimuth angles. Data are usually taken in periods of 28-minute runs. In all data taking, a false trigger with a rate of 1 Hz is injected into the telescope data acquisition logic in order to measure the fluctuations of the pixel average signal level (the pedestal), which is due to stars in the field of view.

Selection of the data for quality involves examining a daily observing log for information on weather conditions and telescope performance. Observers grade the weather on an A/B/C scale. Data taken in A and B weather were used in this analysis. In addition to the observers comments, the pattern trigger rate on the cosmic ray protons drops when clouds interfere with the telescopes view of high energy air showers, so data were accepted when the stability of the proton trigger rate is 10% or better. Finally, the telescope performance depends on the zenith angle, so data taken at large zenith angles, close to the horizon, were rejected. The data runs used in this analysis, after these quality selection cuts, are listed in Table (6.1).

The data for Ursa Minor and Draco dwarf galaxies were taken during the 2002-2003 observing season from December 2002 through July 2003. The M32 dataset was taken entirely during the 2004-2005 Whipple observing season from September 2004 through December 2004. The M33 exposure was split approximately evenly between these two observing periods.

6.1.1 Draco

The observer graded the weather C for just one 7-minute run, 23024. Run 24999 was rejected due to an unstability in the telescope trigger rate noticed by the observer that night. The analysis program found that an excessive amount of pixels were malfunctioning for runs 24564 and 24784, so these runs were rejected. The

Table 6.1. The unique identification number of the data runs used in this analysis. The control run used to estimate the background is also listed.

Draco ON Runs	24252, 24273, 24304, 34326, 24393, 24597, 24645, 24657, 24667, 24668, 24707, 24730, 24731, 24758, 24759, 24773, 24783, 24816, 24830, 24831, 24859, 24913
Draco Background Runs	24162, 24274, 24305, 24327, 24394, 24598, 24646, 24656, 24770, 24692, 24708, 24702, 24766, 24841, 24811, 24774, 24578, 24817, 24614, 24716, 24860, 24914
Ursa Minor ON Runs	23965, 24028, 24043, 24071, 24223, 24594, 24617, 24654, 24704, 24725, 24753, 24771, 24813, 24843, 24911
Ursa Minor Background Runs	23966, 24029, 24044, 24072, 24224, 24595, 24618, 24655, 24705, 24726, 24754, 24772, 24814, 24844, 24912
M33 2002 ON Runs	22864, 22940, 23355, 23385, 23424, 23446, 23507, 23532
M33 2004 ON Runs	27496, 27540, 27551, 27585, 27598, 27759, 27814, 27823, 27848, 27927
M33 2002 Background Runs	22865, 22941, 23356, 23386, 23425, 23447, 23508, 23533
M33 2004 Background Runs	27497, 27541, 27552, 27586, 27599, 27760, 27815, 27824, 27849, 27928
M32 ON Runs	27492, 27529, 27625, 27662, 27693, 27713, 27805, 27825, 27850, 27867, 27867, 27931, 27990, 27998, 28015, 28017, 28039, 28065, 28087, 28113
M32 Background Runs	27493, 27530, 27532, 27626, 27694, 27714, 27806, 27826, 27851, 27868, 27930, 27991, 27999, 28016, 28018, 28040, 28066, 28088, 28114
Crab 2002 ON Runs	22903, 22925, 22927, 22947, 22949, 22951, 22969, 23009, 23036, 23038, 23053, 23055, 23062, 23072, 23156, 23183, 23250, 23270, 23907, 23927, 23982, 24104, 24122, 24152
Crab 2004 ON Runs	27519, 27535, 27546, 27554, 27649, 27701, 27703, 27721, 27723, 27767, 27779, 27861, 27880, 27882, 27920, 28024, 28049, 28073, 28124
Crab 2002 Background Runs	22904, 22926, 22928, 22948, 22950, 22952, 22970, 23010, 23037, 23039, 23054, 23056, 23063, 23073, 23157, 23184, 23251, 23271, 23908, 23928, 23983, 24105, 24123, 24153
Crab 2004 Background Runs	27520, 27536, 27547, 27555, 27650, 27702, 27704, 27722, 27724, 27768, 27780, 27862, 27881, 27883, 27921, 28025, 28050, 28074, 28125

runs 24565 and 25032 were rejected because the pedestal variations in the camera is different from the rest of the dataset. After data selection there are 5 hours of TRACKING mode data, 6 hours of ON data, and 6 hours of data taking in the OFF mode on Draco Dwarf.

6.1.2 Ursa Minor

Weather caused telescope trigger rate instability in runs 23923 and 24594, so these were omitted from the analysis. Observers also notice unstable telescope trigger rates during runs 23965 and 24997, so these runs were rejected. A known software glitch possibly skewed the cosmic ray image distributions in run 24693, which was reported by the observer, so this run was rejected. Removing these runs from the dataset resulted in 7 hours in ON mode, and 7 hours in OFF mode on Ursa Minor Dwarf.

6.1.3 M33

Runs 22875, 22879, 23020, and 23849 were rejected due to weather conditions, which caused the observers to report that the telescope trigger rate fluctuated as clouds drifted through the field of view. The high voltage to half the camera lost power during runs 22876 and 23765, so these runs were rejected because this skews the data due to the geometry of the camera malfunction. After the above data quality cuts, there were 8.7 hours of ON data, and 8.7 hours of data taking in the OFF mode on M33.

6.1.4 M32

Data from November 2002 through January 2003 were rejected because the coordinates the telescope was using for this source were reported with a Declination of $+42^{\circ} 52'$; the actual center of M32 is at a Declination $+40^{\circ} 53'$. In the 2004 dataset, the telescope was pointed at the actual position of M32. Runs 28231 and 28232 were cut short because the data acquisition software was crashing. It is worth noting that in late October the telescope was running without problems with high humidity (90% relative humidity.) By December 2004, arcing was reported in the

camera with 75% relative humidity. Finally during January 2005 the high voltage supply completely stopped working. The other high voltage crashes were probably due to a bad data link to the high voltage supply controllers. After selection of quality data, there were 8.9 hours of ON data and 8.9 hours of OFF data on M32. The total exposure for possible dark matter annihilation sources, before and after quality cuts, are listed in Table (6.2).

6.1.5 Crab

Data are taken each season on the Crab pulsar nebula. The Crab data runs listed in Table (6.1) were used to check the performance of the telescope and analysis for the two observing seasons. ON/OFF pairs taken in A/B weather during the same period of observations that the local galaxy data were taken were used for verifying the performance of the telescope. In total, 20 hours of ON data and 20 hours of off data on the Crab were used in this analysis.

6.1.6 Background Estimation

There is approximately twice the amount of data with the telescope pointed in the source location, ON and TRACK modes, as there are control observations, OFF mode. In order to add more data with no gamma ray signal to the control pool. These runs are selected from the rest of the Whipple dataset by zenith angle, azimuth angle, weather conditions, camera conditions, and time of year. Data collected in OFF mode for the M87 and A2029 datasets were used to add data to

Table 6.2. The total exposure and the exposure used for this analysis on Draco, Ursa Minor, M32, and M33. The data were rejected most often for weather problems and high voltage failures.

Source	RA	Dec	ON/TRK (hrs)	OFF (hrs)
Draco	17 20 14	+57 55	10.3	5.6
Ursa Minor	15 09 10	+67 13	7.0	7.0
M32	00 42	+40 52	8.9	8.9
M33	01 33 51	+30 39	8.7	8.7

the control set. In addition, some runs taken in TRACK mode were not used if an acceptable background file could not be found. This can cut down the amount of data significantly, but the background is difficult to estimate and changes with (at least) zenith angle and the time of year. Five hours of data of this type were used to estimate the background for the Draco dataset.

6.2 Analysis

The analysis of the data was comprised of four steps. First, the calibration data from the telescope were applied to the data to make telescope independent data. This included checking which pixels are working and applying the flat-fielding to equalize the gain of each PMT. Second, the images were cleaned in order to get rid of false signal caused by fluctuations in the night sky. Third, the images were parametrized. This consisted of reducing the dimensionality of the data from the 499 dimensional pixel values, into a smaller set of image parameters. Finally cuts were placed on the parameters to extract gamma-ray events from the larger cosmic ray background.

The standard analysis technique for the Whipple Telescope is naturally sensitive to a very small region of gamma-ray energy space for weak sources. The standard analysis is optimized on the Crab data, which has a power law spectrum, $F \sim E^{-\alpha}$ with $\alpha = 2.5$, and the region of peak sensitivity is around 400 GeV. In order to check for line spectra or various power law spectra, for which the peak sensitivity of the telescope would be at a different energy, an N-dimensional maximal likelihood analysis was developed.

6.2.1 Calibration

Some PMTs malfunctioned during the observing time, or they were turned off by the observer to protect them against bright stars in the field of view. These pixels were removed from the analysis. This was accomplished by examining the random pedestal data and these bad pixels were flagged. The pedestal events were measured with the 1 Hz forced trigger in the telescope that takes random snapshots of the night sky. The mean signal from these events is called the PMT pedestal. In

addition, the width of the pedestal distribution in each PMT was calculated from the dispersion in the pedestal data. We used the fluctuations to determine the pedestal widths because the signals are AC coupled and the dark current does not scale with the intensity of light. When the fluctuations dropped to zero, the pixel was flagged as turned off and was excluded from the analysis. Fig. (6.1) shows the pixel status for the camera for run 24252 as a typical example.

The gains of the PMTs were calibrated relative to each other using two standard, independent methods. Each night a nitrogen arc lamp was flashed at the focal plane for at least 1 minute. The amount of light in each flash is relatively uniform across the field of view and so these data can be used to calibrate the relative gains of each PMT. The second method of relative gain calibration was based on the isotropy of the cosmic ray spectrum across the field of view. This method assumed that any differences in the cosmic ray spectrum between pixels were due to a difference in PMT gain. A histogram was built with the amount of charge that was recorded from each PMT in all events. Then a predefined region, bright events well away from random noise induced triggers, of was fitted to a power law spectrum. These spectra were then used to calculate the relative gains of the PMTs. We used gains calculated using the second method for this analysis. An example of the gain spread using this method is shown in Fig. (6.2). The nitrogen flasher gains were used for error and sanity checking of the cosmic ray gains. The cosmic ray throughput, calculated in a similar manner to the PMT gains, but using the total amount of light in the camera as opposed to the light in individual PMTs, allowed a measure of the total telescope gain including any differences in the atmosphere, mirrors, and PMTs through the observation season. This is discussed in more detail in [113].

Images of muon rings were used for absolute calibration of the telescope. Muons near the telescope are a natural part of the data taken with an IACT. Many of these particles survive all the way to ground level. When a muon passes through the telescope it creates a complete ring with a known amount of light in the camera as seen in Fig. (6.3). Thus, from the amount of charge recorded in the image, the absolute Cherenkov photon to digital count conversion can therefore be measured.

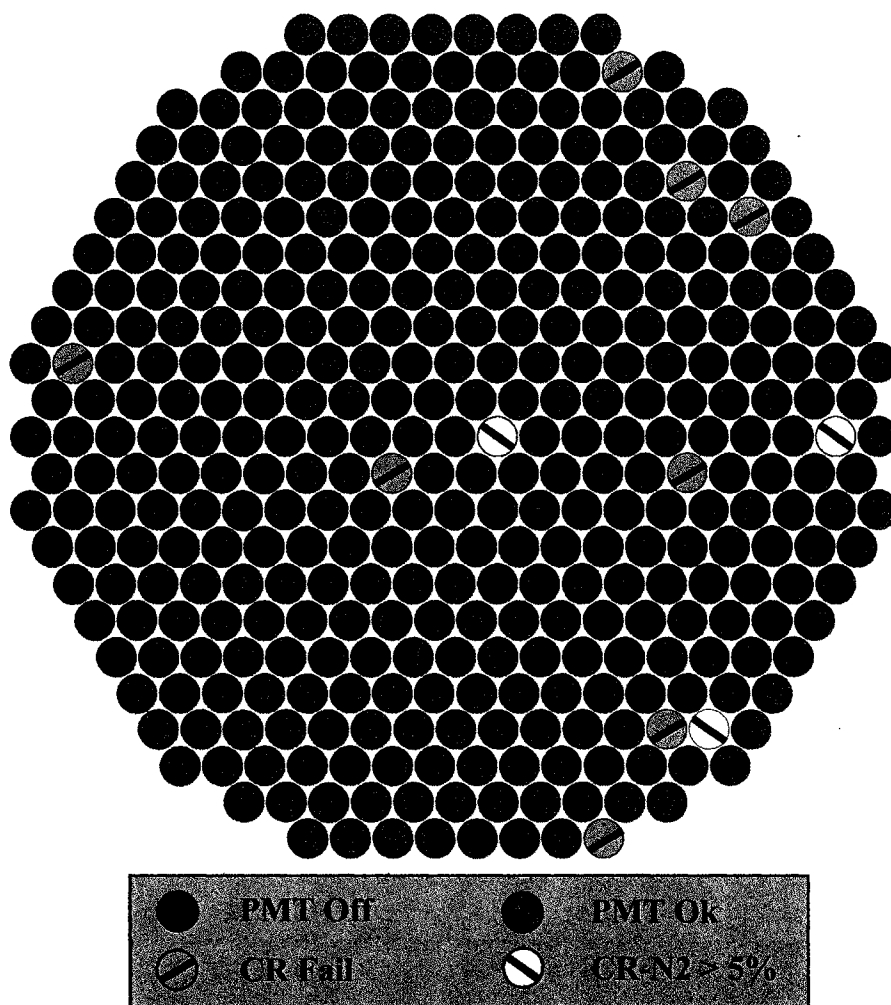


Figure 6.1. A map of the pixel calibration for run 24252. 94.7% of the PMTs in the camera were used for the analysis of the data from this run.

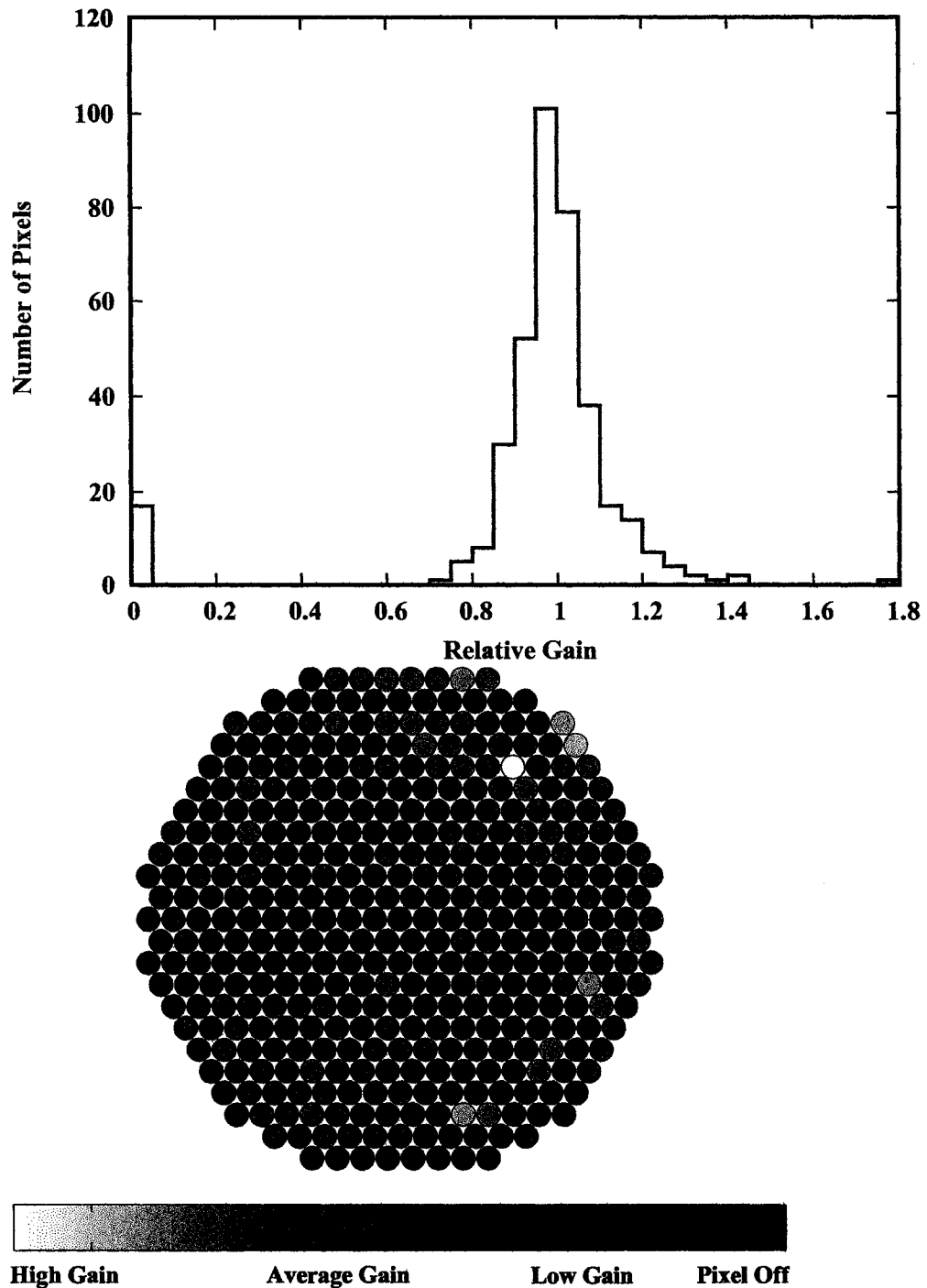


Figure 6.2. The relative gains for run 24252. The histogram shows the pixel relative gains. The bins have a width of 5% of the average gain. In the camera view, lighter grey indicates higher gains and the scale is shown because it is shifted from the normal values with an average gain of 1. Excluding the off pixels, with gain 0, and the abnormal pixel, with a gain of 1.7, the average relative gain is 1.01 with a width of 0.09.

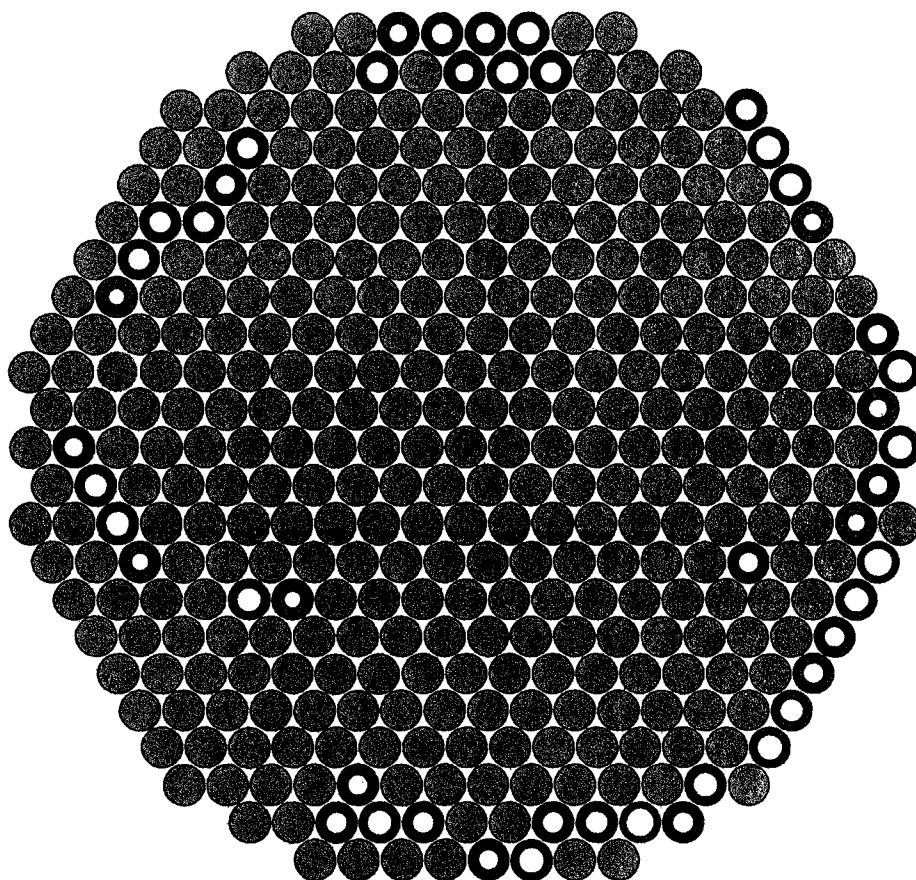


Figure 6.3. A candidate muon event. The darker grey pixels are image pixels. The size of the inner white circle represents the amount of charge measured in each pixel. Notice the characteristic circular shape of the complete muon images that are used for absolute calibration of the photon to digital count ratio in the telescope.

A more complete description of this absolute calibration method is given in [114] and [115].

6.2.2 Image Cleaning

Before the analysis was done, the images were cleaned. Cleaning is the process of removing pixels that have low signals near the level expected from the measured pedestal fluctuations. All working pixels with integrated charge of 4.25 sigma above the pedestal fluctuation were kept. These pixels are called image pixels. The pixels with a charge above 2.25 sigma of the background are kept if they neighbor an image pixel. These are called border pixels.

6.2.3 Parametrization - Hillas Parameters

The standard Whipple analysis consists of basic cuts on the parameter space of the Hillas parameters [110]. The Hillas parameters are based on the statistical moments of the light distribution in the camera. The coordinates of the center of each pixel in the image plane are given by x_j, y_j in units of degrees. The center of the field of view defines the origin of the coordinate system. The zeroth moment, the amount of light in the image, is called SIZE and is defined as

$$SIZE = \sum_j S_j \quad (6.1)$$

where S_j is the amount of charge recorded in PMT j in units of digital counts (dc). The index j runs over the pixels in the camera that were determined to be working during the observations and have signal from the event. In the analysis we use the $\log_{10}(SIZE)$ as a parameter because the fluctuations in the air shower are logarithmic due to the multiplicative nature of the shower development [116]. The amounts of charge in the brightest two pixels in the image are called MAX1 and MAX2, respectively, and were used to eliminate random triggers.

The first moments of the charge distribution determine the centroid of the image with

$$\bar{x} = \frac{\sum_j S_j x_j}{SIZE} \quad \text{and} \quad \bar{y} = \frac{\sum_j S_j y_j}{SIZE}. \quad (6.2)$$

The centroid is then used to calculate the parameters DISTANCE and ALPHA. DISTANCE is defined to be the angle between the centroid and the center of the camera

$$DISTANCE^2 = \bar{x}^2 + \bar{y}^2. \quad (6.3)$$

The DISTANCE angle is related to the impact parameter of the shower geometrically. Because the number of showers is constant per unit area we use the DISTANCE² in this analysis.

Finally the second moments are calculated as

$$Q_{xx} = \frac{\sum_j S_j x_j x_j}{SIZE}, \quad Q_{yy} = \frac{\sum_j S_j y_j y_j}{SIZE}, \quad \text{and} \quad Q_{xy} = Q_{yx} = \frac{\sum_j S_j x_j y_j}{SIZE}. \quad (6.4)$$

The matrix Q is positive symmetric and can be diagonalized. The eigenvector Q¹ with the larger eigenvalue, called LENGTH, defines the orientation of the shower image in the camera and the angular extent of the shower in the sky. The dot product of Q¹ and the centroid vector defines the angle ALPHA. The smaller eigenvalue characterizes the WIDTH of the image and is a good discriminator between hadronic and electromagnetic showers; cosmic ray showers are typically wider because the transverse momentum in the shower is carried by the pion, whereas the transverse momentum in an electromagnetic shower is carried by the electron. ALPHA is a good discriminator for point sources in the center of the field of view because the hadronic showers are isotropic. Any gamma-ray point source can be identified as an anisotropic excess of electromagnetic showers. An example of a parametrized cosmic ray image is shown in Fig. (6.4).

6.2.4 Parameter Cuts

In the standard Whipple Telescope analysis the cuts are developed as a rectangular-solid in the parameter space. Usually a SIZE cut is imposed first. The lower limit of allowed SIZEs is used to exclude events that have just barely triggered the telescope. This trigger region of the data is not well understood and can have large fluctuations due to stars, arcing, or electronic pickup noises. After the cut on the SIZE of the image is applied, a cut on the shape parameters is imposed on the images to

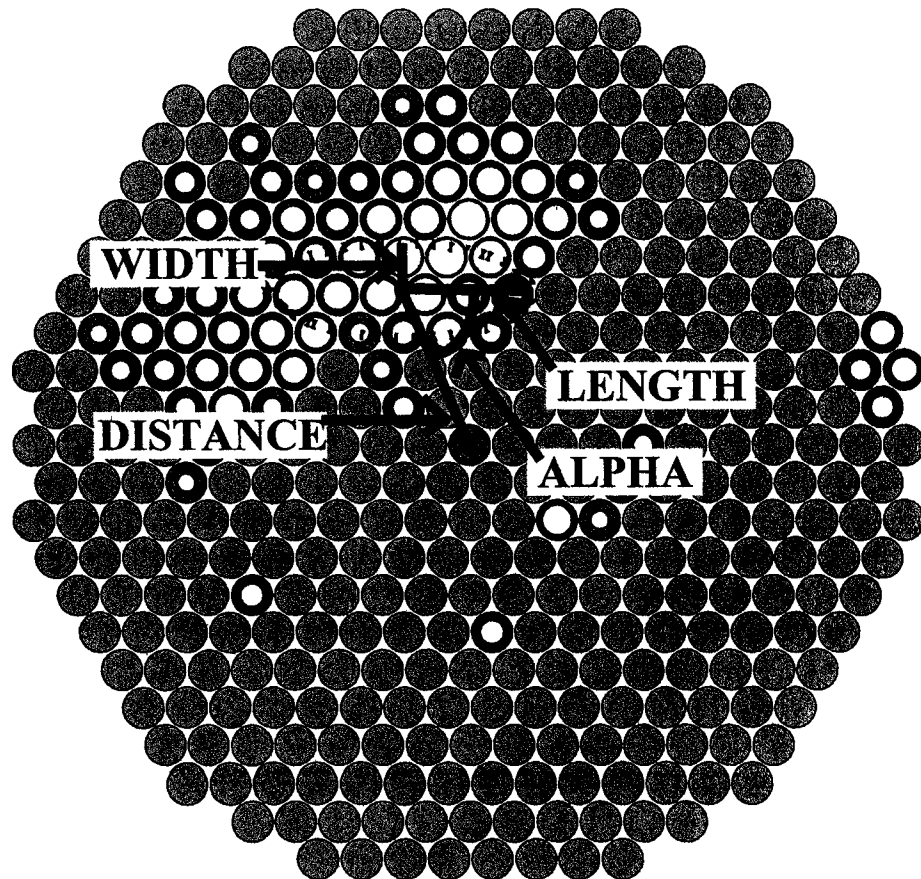


Figure 6.4. A parametrized cosmic radiation Cherenkov image. The dotted ellipse is a pictorial representation of the first and second moments of the image. The center of the ellipse is measured as the first moments of the image. The second moments are represented by the shape of the ellipse. The major axis is the LENGTH parameter and the minor axis is the WIDTH parameter. The angle between the major axis and the center of the field of view is the ALPHA parameter.

select electromagnetic showers. The parameters used are DISTANCE, LENGTH, WIDTH. Finally an ALPHA cut is imposed to restrict the analysis to showers pointed at the target in question. These cuts are generally optimized with respect to significance on data taken on the Crab pulsar from the same observing season the data to be analyzed were taken. The standard set of cuts is called SuperCuts 2000 (SC2000) and was optimized on the Crab data from the year 2000-2001 observing season. These cuts are robust for the current Whipple Telescope camera, which has not changed significantly since these cuts were derived. The most significant change in the hardware was a systematic increase of the PMT gains at the beginning of each season. None of the cuts should change as a result of this because the gain change between seasons was removed in the calibration. The SC2000 cuts are listed in Table (6.3).

We implemented a novel multidimensional analysis in order to improve the gamma-ray sensitivity beyond the standard SC2000 cuts by using correlations between the parameters. This analysis was also used to search for gamma-ray spectra different from the Crab. In this study, a five-dimensional parameter space was used. The primary reason for limiting the dimensionality was to keep the space from being sparsely populated. In order to choose the integration volume that is the most sensitive to a given source energy spectrum, we used a method based on the maximum likelihood method. In our N-dimensional parameter space, we label each cell with an index j such that \sum_j denotes integration over the parameter space volume illustrated in Fig. (6.5). The events in each cell are Poisson distributed so the probability to find k events in cell j is

$$P_{k_j(\langle n_j \rangle)} = \frac{\langle n_j \rangle^k}{k!} e^{-\langle n_j \rangle} \quad (6.5)$$

where $\langle n_j \rangle$ is the expected event average in cell j . The likelihood of a given observation, $\{k_j\}$, of the occupation of the parameter space cells is given by

$$L = \prod_j P_{k_j(\langle n_j \rangle)} = e^{-\sum_j \langle n_j \rangle + \sum_j k_j \ln(\langle n_j \rangle) - \sum_j \ln(k_j!)} \quad (6.6)$$

Now consider two datasets, ON and OFF, with exposure times T^{ON} and T^{OFF} and parameter space occupation ON_j and OFF_j . Under the hypothesis that there is

Table 6.3. The standard analysis cuts for the Whipple Telescope, SuperCuts 2000.

Parameter	Lower Bound	Upper Bound
MAX2	30	N/A
DISTANCE	0.4	1.0
WIDTH	0.05	0.12
LENGTH	0.13	0.25
LENGTH/SIZE	0	0.0004
ALPHA	0	15

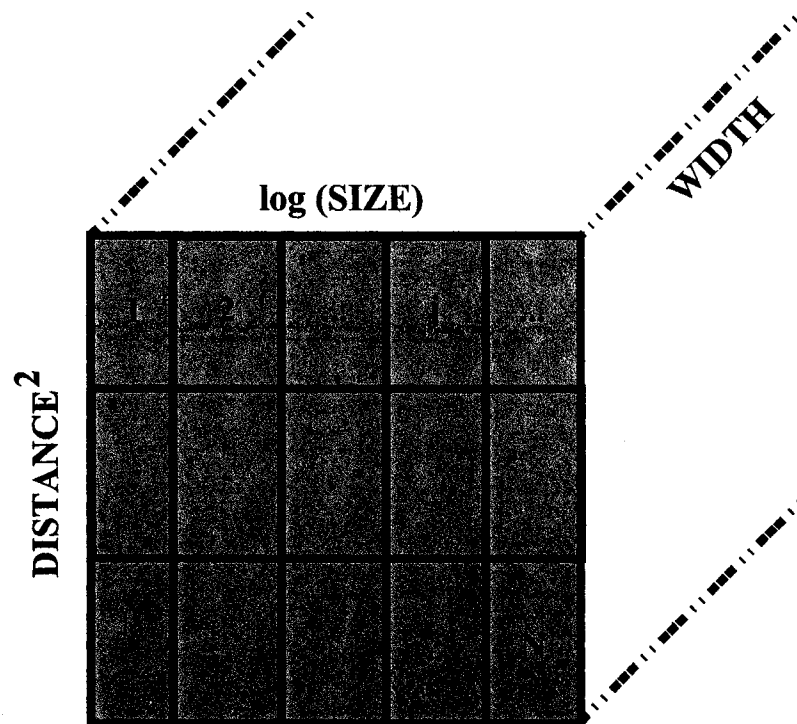


Figure 6.5. An illustration of the N-dimensional parameter space in which the maximum likelihood analysis is implemented.

no gamma-ray signal present in either dataset, the gamma-ray occupation of the parameter space $g_j = 0 \forall j$, the likelihood is

$$\begin{aligned} \ln(L_o) = & - \sum_j \langle OFF_j \rangle + \sum_j OFF_j \ln(\langle OFF_j \rangle) - \sum_j \ln(OFF_j!) \\ & - \sum_j \alpha \langle OFF_j \rangle + \sum_j ON_j \ln(\alpha \langle OFF_j \rangle) - \sum_j \ln(ON_j!) \end{aligned} \quad (6.7)$$

and $\alpha = T^{ON}/T^{OFF}$. Now the maximum likelihood estimate of $\langle OFF_j \rangle$ is the solution to

$$\frac{\delta \ln(L_o)}{\delta \langle OFF_j \rangle} = -1 + \frac{OFF_j}{\langle OFF_j \rangle} - \alpha + \frac{ON_j}{\langle OFF_j \rangle} = 0, \quad (6.8)$$

which gives the usual answer

$$\langle OFF_j \rangle = \frac{OFF_j + ON_j}{1 + \alpha} \equiv b_j. \quad (6.9)$$

Now let us assume that a gamma ray signal is present in some of the cells. The likelihood under the assumption that there is a signal present, L_g , is given by

$$\begin{aligned} \ln(L_g) = & - \sum_j \langle OFF_j \rangle + \sum_j OFF_j \ln(\langle OFF_j \rangle) - \sum_j \ln(OFF_j!) \\ & - \sum_j (\alpha \langle OFF_j \rangle + g_j) + \sum_j ON_j \ln(\alpha \langle OFF_j \rangle + g_j) - \sum_j \ln(ON_j!) \end{aligned} \quad (6.10)$$

as usual, we introduce $z = \sum_j z_j = \ln(\frac{L_g}{L_o})$ where

$$z_j = (1 + \alpha)[b_j - \langle OFF_j \rangle] - g_j + OFF_j \ln\left(\frac{\langle OFF_j \rangle}{b_j}\right) + ON_j \ln\left[\frac{\langle OFF_j \rangle}{b_j} + \frac{g_j}{\alpha b_j}\right] \quad (6.11)$$

is the ratio of the likelihoods for each cell which we rewrite as

$$z_i = -(1 + \alpha)b_j[x_j - 1] - \alpha b_j f_j + (1 + \alpha)b_j \ln(x_j) + ON_j \ln\left(1 + \frac{f_j}{x_j}\right) \quad (6.12)$$

where $x_j = \frac{\langle OFF_j \rangle}{b_j}$ and $f_j = \frac{g_j}{\alpha b_j}$. According to the Wilke's theorem $2z$ is asymptotically distributed as χ^2 . We define the coordinates of the cell j in the parameter space as $(p_1^j, p_2^j, \dots, p_m^j)$ where m is the parameter space dimension.

Now if $\frac{\delta^m A(p_1, \dots, p_m | E)}{\delta p_1 \dots \delta p_m}$ is the differential collecting area of photons after appropriate data selection, cleaning, and all cuts, then

$$\frac{\delta^m R}{\delta p_1 \dots \delta p_m} = \int \frac{\delta^m A(p_1, \dots, p_m | E)}{\delta p_1 \dots \delta p_m} \times E \frac{dF}{dE} \times \frac{dE}{E} \quad (6.13)$$

is the differential photon observation rate for a source with the spectrum $E \frac{dF}{dE}$, and the expectation value for g_j is

$$g_j = \frac{\delta^m R}{\delta p_1 \dots \delta p_m} \Big|_{(p_1^j, \dots, p_m^j)} \times \prod_{k=1}^m \Delta p_k \times T_{ON} \quad (6.14)$$

and $\Delta^m p = \prod_{k=1}^m \Delta p_k$ is the volume of the parameter space cell.

If a given spectrum, $E \times \frac{dF}{dE}$, is parameterized by ℓ parameters, s_1, \dots, s_ℓ , then the expectation values from the signal, g_j , are functions of s parameters such that they cannot be chosen independently for different cells. The parameter space cells are coupled by the differential collecting area of photons with different energies. In this sense the functional z can be viewed as

$$z = z(x_j; s_1, \dots, s_\ell) \quad (6.15)$$

where x_j estimate the background in each cell and s_1, \dots, s_ℓ estimate the spectrum of a source in question. The maximum likelihood estimates of these parameters are given by

$$\frac{\delta z}{\delta x_j} = (1 + \alpha) b_j \left(\frac{1}{x_j} - 1 \right) + ON_j \left[\frac{1}{x_j + f_j} - \frac{1}{x_j} \right] = 0 \quad , \quad \forall j \quad (6.16)$$

and

$$\frac{\delta z}{\delta s_m} = \sum_j \left[-\alpha b_j + \frac{ON_j}{f_j + x_j} \right] \frac{\delta f_j}{\delta s_m} = 0 \quad , \quad \forall m = 1, \dots, \ell. \quad (6.17)$$

6.2.5 Parameter Optimization

In order to compare the relative strengths of a given set of parameters, both the parameters derived in the standard analysis and any new proposed parameters, i.e., [117], a standard procedure for determining the best binning for the set was

developed. This procedure takes an expected signal distribution, generated from simulations, and bins the input parameters with 2^x bins where $x \in [0, 5]$ parameter by parameter. Then we calculate z_j and scan through cuts on z_j , the ratio of likelihoods for a given cell, at a level z_{cut} . We define a filter on the space

$$a_j = \begin{cases} 1 & z_j \geq z_{cut} \\ 0 & z_j < z_{cut} \end{cases} \quad (6.18)$$

Now we define the number of events in the parameter space regions of interest as

$$N_{on} = \sum_j a_j ON_j \quad \text{and} \quad N_{off} = \sum_j a_j OFF_j. \quad (6.19)$$

Then the significance is calculated in the usual way [118]

$$\sigma = \sqrt{2} \sqrt{N_{on} \ln \left[\frac{(1 + \alpha) N_{on}}{\alpha (N_{on} + N_{off})} \right] + N_{off} \ln \left[(1 + \alpha) \frac{N_{on}}{N_{on} + N_{off}} \right]} \quad (6.20)$$

By letting the algorithm choose the cuts we can optimize the cuts and parameters based on the spectrum that we expect from an observational target. Additionally we can optimize the cuts to a specific background field. This can be advantageous if, for example, the stars in the field of view cause problems like shifting any distributions or causing false triggers.

This optimization was performed on the Draco off field and the Crab off field to determine if this optimization is specific to an individual set of runs or if this is a general binning that works well for all the telescope data. We tried the usual Hillas parameters, based on the moments of the light distribution in the camera, as well as a few looking for the geometry of the shower. The binning that results in the maximum calculated significance, σ_{max} , is the binning used for calculating fluxes. Additionally we can compare various sets of parameters through σ_{max} . The set of parameters $\{LENGTH, WIDTH, \log_{10}(SIZE), DISTANCE^2, \text{and } ALPHA\}$ was the most sensitive set and the most sensitive binning depended on the expected spectral distribution. Some novel parameters from [117] were used in the optimization procedure but did not improve the signal to noise ratio.

6.2.6 Crab Normalization

After the optimization of the cuts we find either a flux, if the excess is significant, or an upper limit for the flux. Upper limits calculated are based on the method in [119] with a confidence level of 95%. The derived limit is on the rate of photons detected. This rate was then compared to the detected rate of photons from the Crab pulsar nebula. The same cuts a_j are applied to a set of Crab data taken during the same observational period. This rate then defines a Crab unit of flux. This corresponds to the flux of the Crab pulsar integrated with the telescope response and the collecting area defined by the cuts. The collection area as a function of energy with these cuts was then estimated using the simulations. The collecting area is defined as the ratio of the events that pass the cuts multiplied by the area over which the simulations were thrown. Thus the results of the standard point source analysis are given in units of the Crab flux. The energy region that this flux is integrated over is presented as a collection area in units of cm^2 in Figs. (6.6,6.7).

6.2.7 Crab Plerion

The plerion around the Crab is a known TeV gamma-ray emitter at least up to 80 TeV [66]. This was the first TeV gamma-ray source to be identified [15] and it is used as the standard candle with which to compare results. All results on the selected dwarf galaxies are stated relative to the excess of gamma rays from the Crab pulsar plerion.

In order to check for a systematic excess in the cosmic ray background of the ON and OFF regions we generated ALPHA plots for the Crab data. The ALPHA plots for the standard analysis are shown in Fig. (6.8). The plots show that the excess in the ON data is peaked at $ALPHA = 0$. This demonstrates that the excess showers are pointed towards the center of the field of view. The two histograms are well matched for $30^\circ < ALPHA < 60^\circ$. This shows that the number of cosmic ray events in the two data sets are well matched indicating the appropriateness of the OFF source data for estimating the ON source background. The cuts in the MML method include the ALPHA parameter and so ALPHA plots are not used in

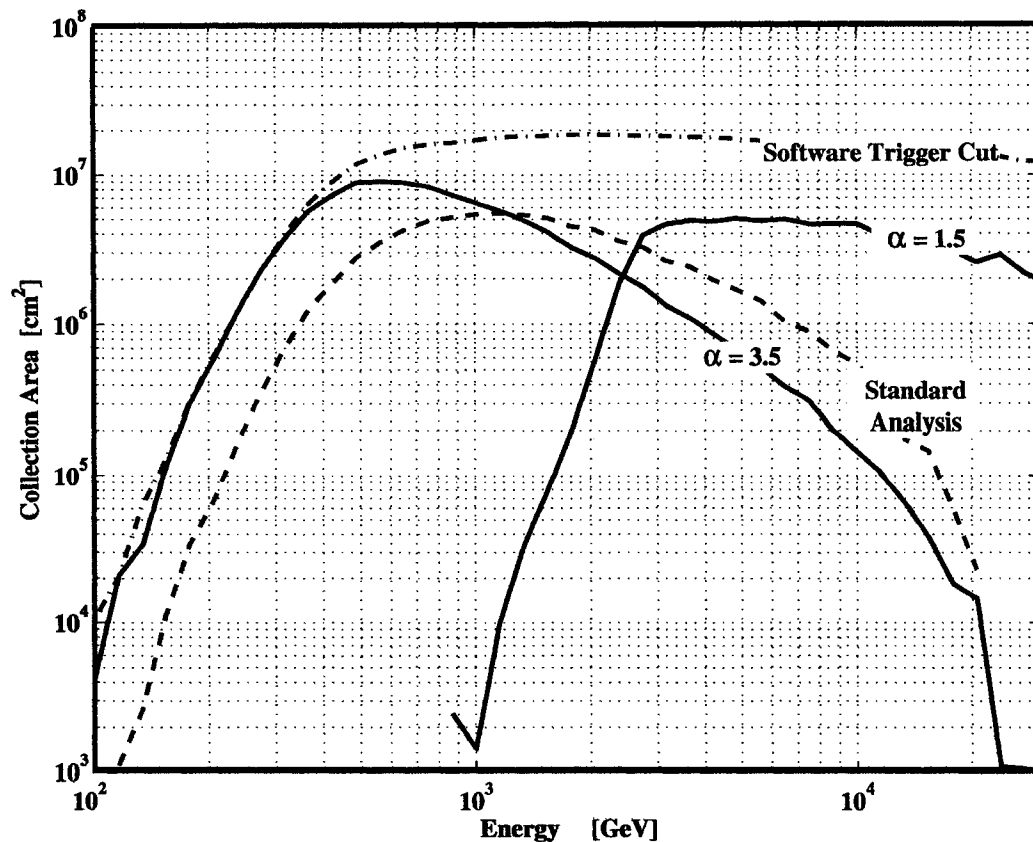


Figure 6.6. Collecting area for the cuts derived with the MML method for power law spectra. The cuts for a hard $\alpha = 1.5$ are focused on the high energy. Notice that this is much more sensitive at high energies than the standard SC2000 analysis. For a soft $\alpha = 3.0$ spectrum, the cuts focus on the low energies.

the MML method. Including the ALPHA parameter in the MML method allows adjusting the ALPHA cut for correlation of the ALPHA angle on, say, the SIZE of a particular event.

The collecting area of the different cuts is shown in Figs. (6.6,6.7). This is the ratio of the events that pass the cuts multiplied by the area over which the simulations were seeded. These two plots show the sensitivity of the cuts for the two type of spectra expected from particle annihilation: continuum power law spectra and line emission. The cuts optimized for harder spectra are more sensitive to high

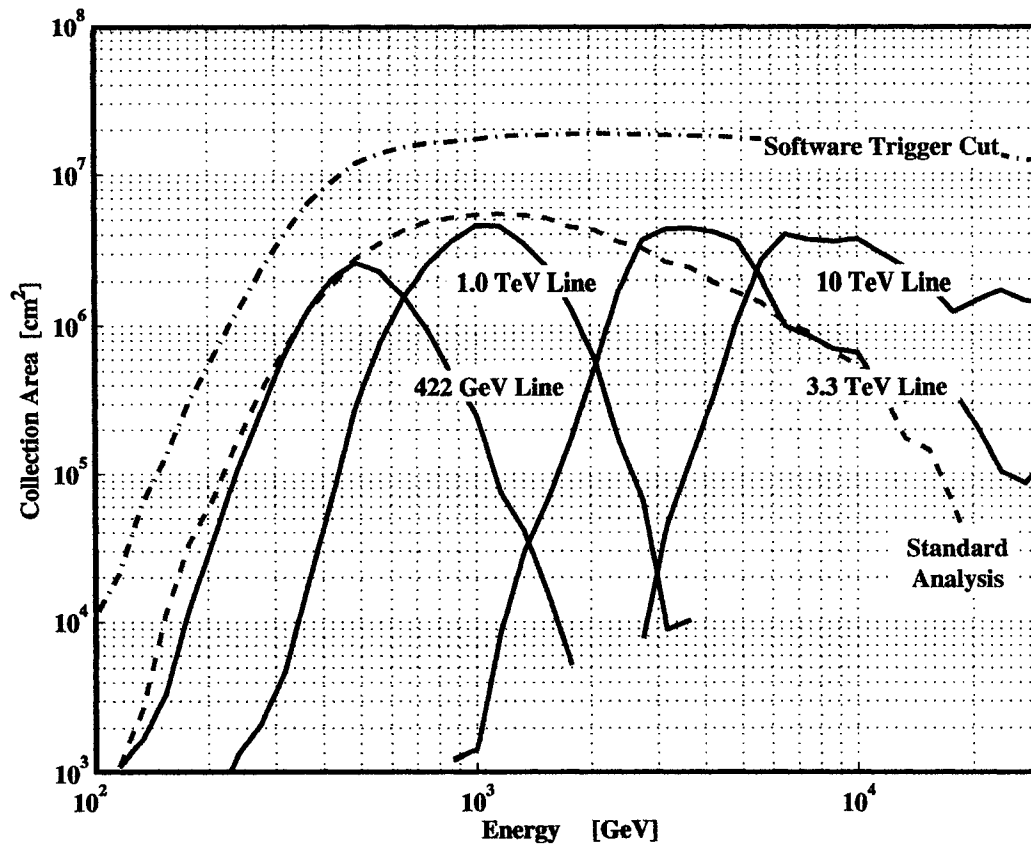


Figure 6.7. Collecting area for the cuts derived with the MML method for line emission. At low energies the algorithm just takes all low SIZE events, looking for a large excess of events. Line emission below the 'threshold' can be seen if the emission is high enough to cause spill over into the telescope energy range. At larger energies the high energy tail begins to grow as the Whipple Telescope calorimetry starts to fail when images are significantly truncated.

energy photons, whereas the soft spectrum optimized cuts are more sensitive to low energy photons. The detector energy resolution is reduced at low energies because the telescope only triggers on positive fluctuations of shower light yield. As the energy of the shower increases, the shower length increases and much of the shower is outside the field of view for the highest energy showers. In this case, a substantial fraction of the shower light is not detected, so the uncertainty in the shower energy increases. This causes the large tails in the sensitivity at high energies.

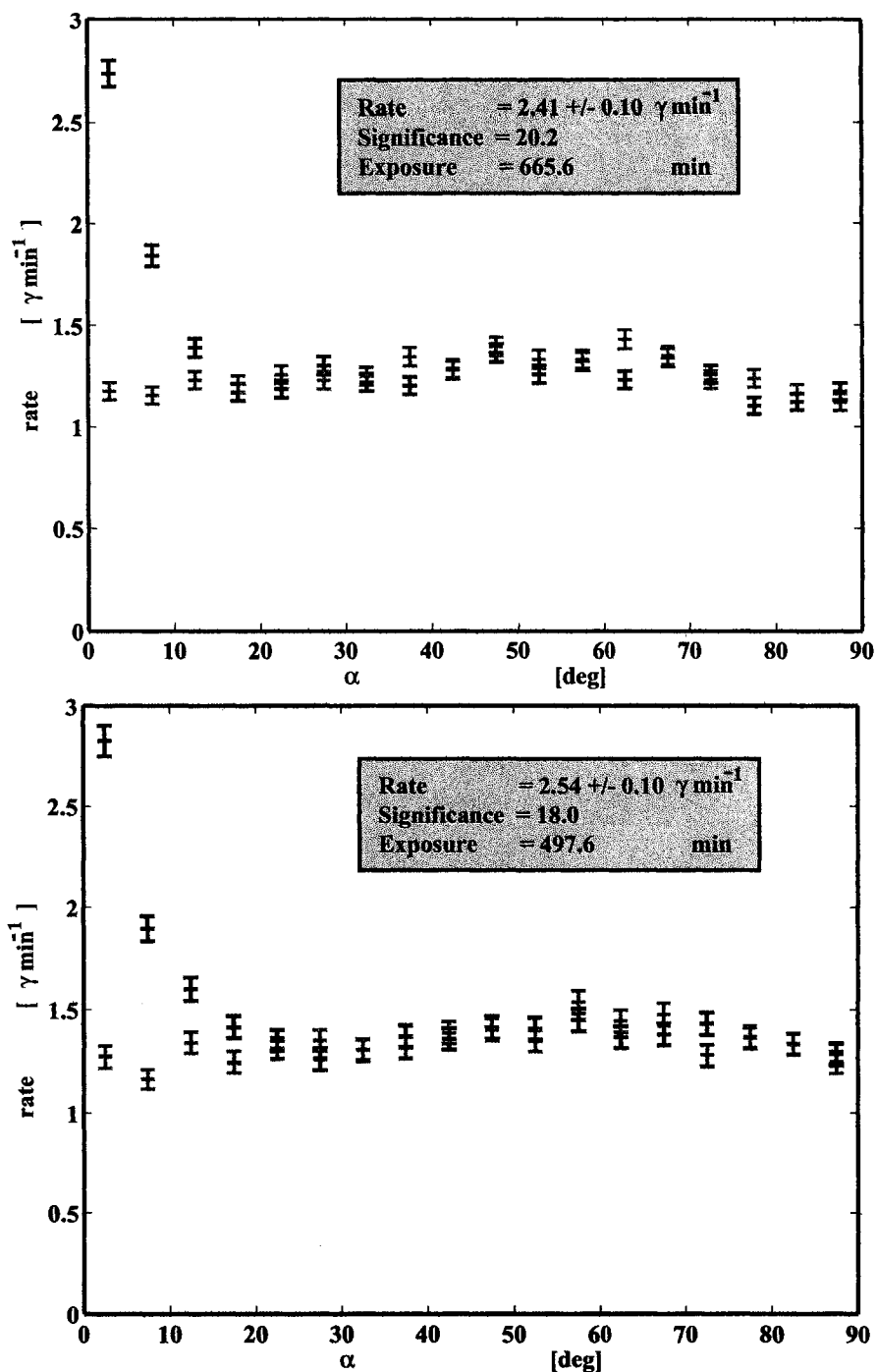


Figure 6.8. ALPHA plots for the SC2000 analysis. The top plot is for the 2002-2003 observing season and the lower plot uses the data from 2004-2005. The black points are the data passing the image shape cuts taken from in the ON mode. The grey data were taken in the OFF mode used to estimate the background. The signal is the excess in the first three ALPHA bins. The error bars are statistical only. The signal rate and the background rate between seasons agree to within the statistical errors.

The Crab dataset is taken each season to check for any yearly changes in the response of the telescope. ALPHA plots for the two observing seasons are shown in Fig. (6.8). There is a background level of electromagnetic showers that point isotropically in the camera at every alpha angle. Also, the excess in the ON ALPHA plot at $ALPHA < 15$ is interpreted as gamma rays from the Crab plerion. Both the background and the signal levels in these two datasets agree which shows that the calibration described above takes care of the 10 – 20% systematic gain difference in the telescope between the two seasons. Thus, the analysis is not changed between the two different seasons.

6.3 Analysis Results

The results from the standard point source analysis are shown in Table (6.4). These cuts are optimized for a Crab-like source spectrum and flux. We include the standard ALPHA plots for these results in Figs. (6.9, 6.10, 6.11, 6.12).

The results from the search for minimally observable power law spectra with the MML analysis are presented in Figs. (6.13, 6.14, 6.15, and 6.16). The power law index is related to the slope of the upper limit lines. The extent of the line is the range of energies for which the cuts are sensitive. We used two sets of cuts for power law spectra with power law index $\alpha = 2.0$ because during the binning optimization two sets of binning had roughly equal sensitivity, but included different energy ranges. The energy range of the cuts is shown with the extent of the line for each of our power law assumptions.

Additionally, we searched for line emission in the data. The analysis was tested for the range from 200 GeV to 40 TeV. We found that the Whipple Telescope has reasonable sensitivity to lines in the energy range [300, 10] TeV. Outside this range we found that the flux would have to be much larger than 1 Crab. The minimum flux needed for a five sigma detection in 20 hours of exposure is shown in Fig. (6.17). No significant line emission was found in the data, and upper limits on the line flux are shown in Figs. (6.18, 6.19, 6.20, and 6.21).

Table 6.4. The results of the standard analysis for the data taken on the four potential dark matter annihilation sources. The Crab flux is $3.25 \times 10^{-11} \text{ cm}^{-2} \text{ s}^{-1}$.

Object	Significance [σ]	Upper Limit [$\gamma \text{ min}^{-1}$]	Upper Limit [Crab Flux]
Draco	-0.01	0.21	0.09
Ursa Minor	-1.64	0.20	0.08
M32	-0.08	0.20	0.08
M33	+0.89	0.26	0.10

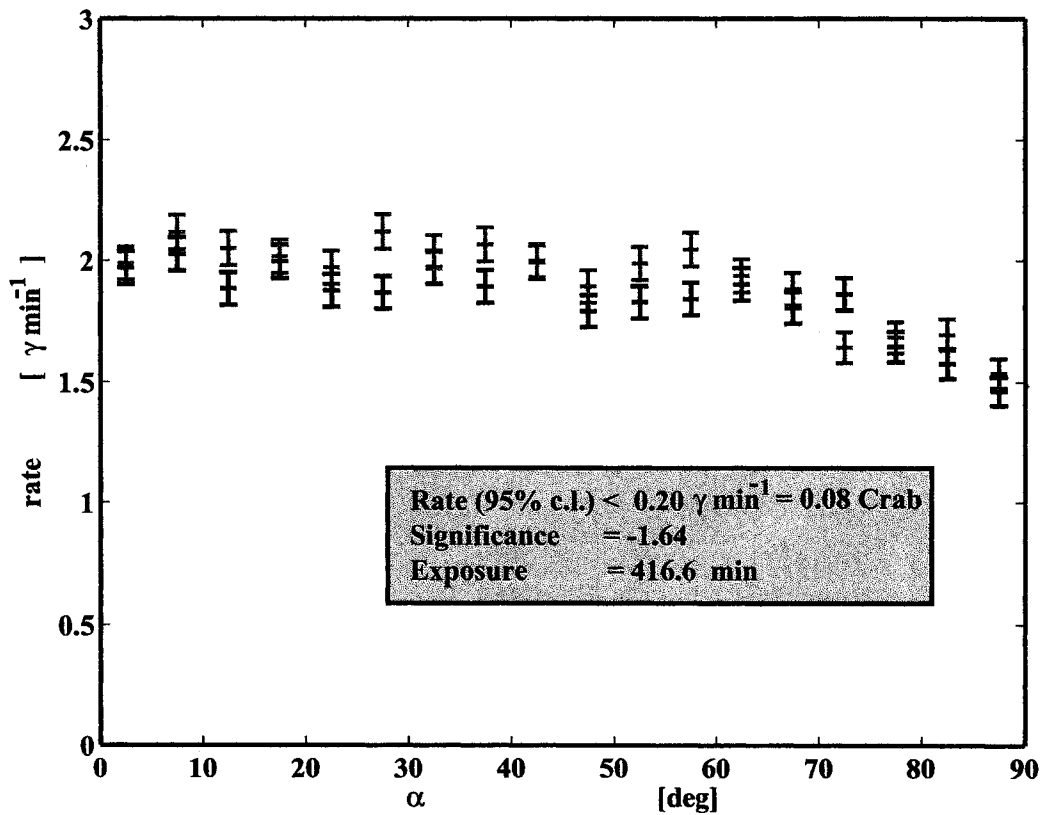


Figure 6.9. The ALPHA plot for the exposure on the Ursa Minor dwarf galaxy. The data were cut using the standard image parameter cuts listed in Table (6.3). The black points are the data passing the image shape cuts taken from in the ON mode. The grey data were taken in the OFF mode used to estimate the background. The error bars are statistical only.

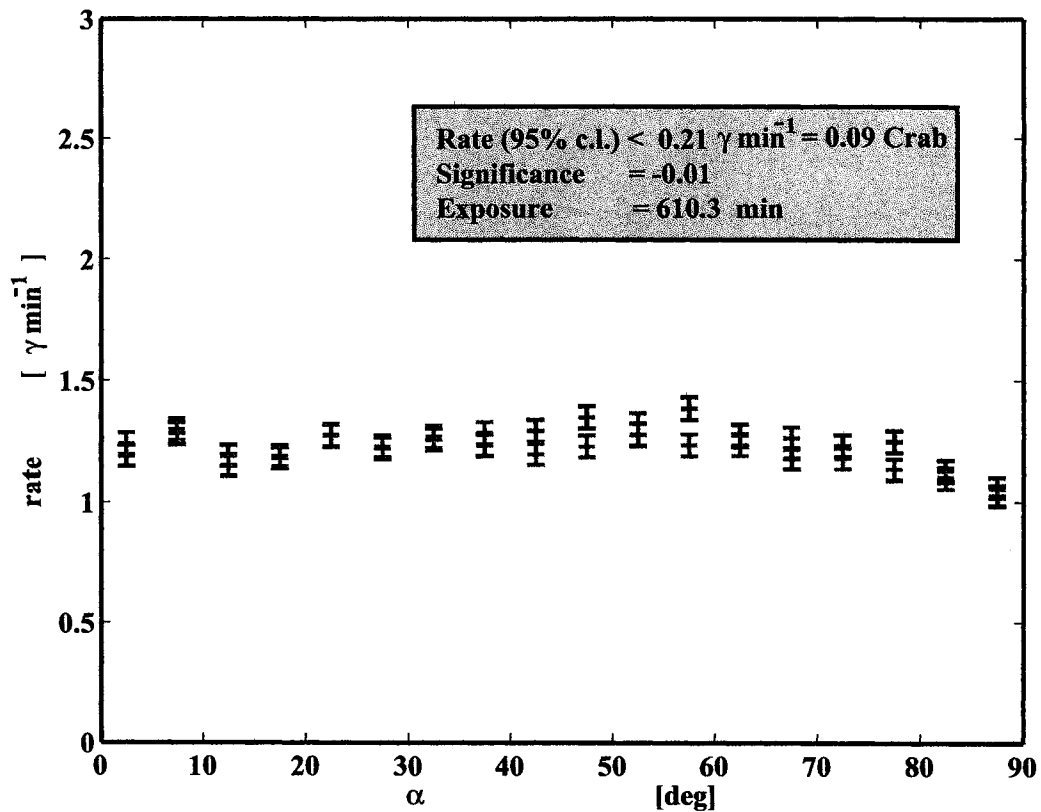


Figure 6.10. The ALPHA plot for the exposure on the Draco dwarf galaxy. The black points are the data passing the image shape cuts taken from in the ON mode. The grey data were taken in the OFF mode used to estimate the background. The data were cut using the standard image parameter cuts listed in Table (6.3). The error bars are statistical only.

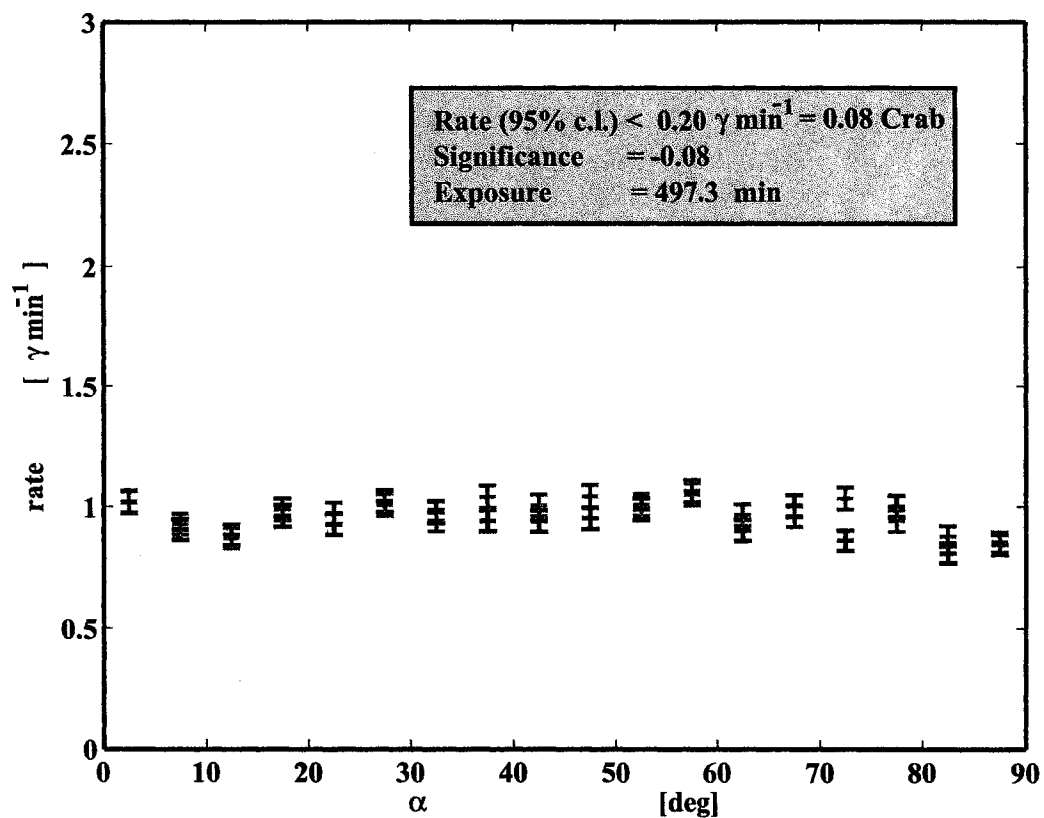


Figure 6.11. The ALPHA plot for the exposure on the M32 elliptical galaxy. The black points are the data passing the image shape cuts taken from in the ON mode. The grey data were taken in the OFF mode used to estimate the background. The data were cut using the standard image parameter cuts listed in Table (6.3). The error bars are statistical only.

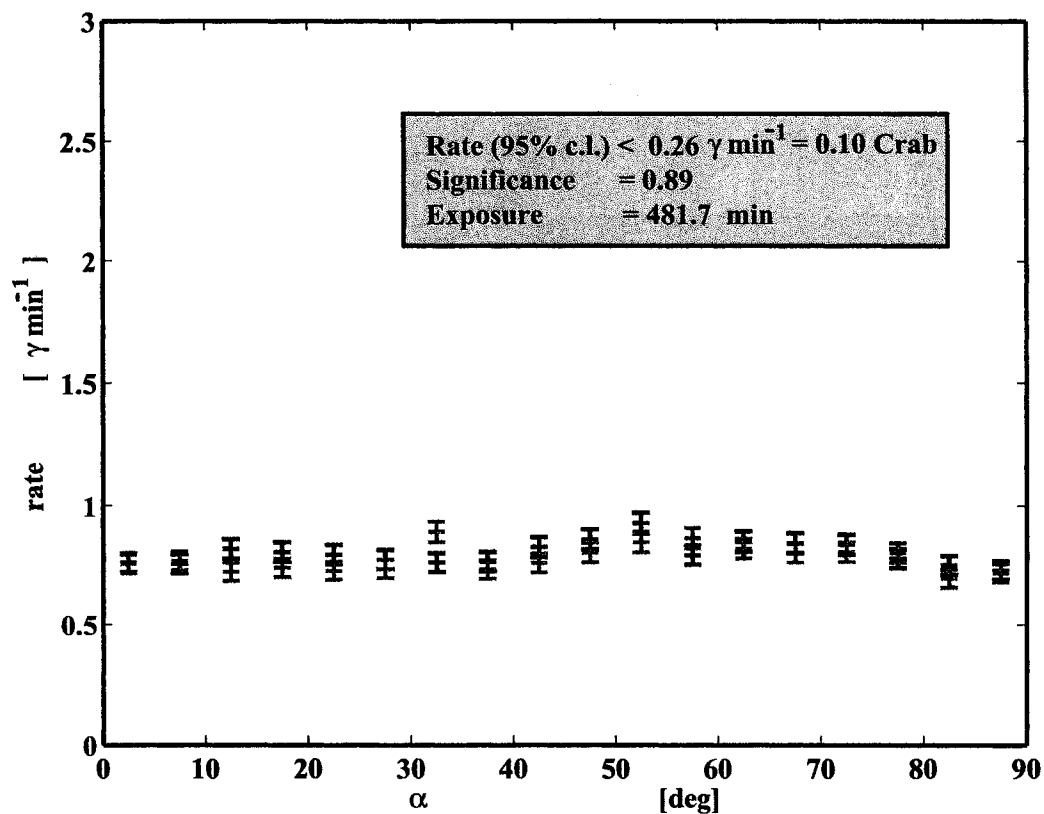


Figure 6.12. The ALPHA plot for the exposure on the M33 spiral galaxy. The black points are the data passing the image shape cuts taken from in the ON mode. The grey data were taken in the OFF mode used to estimate the background. The data were cut using the standard image parameter cuts listed in Table (6.3). The error bars are statistical only.

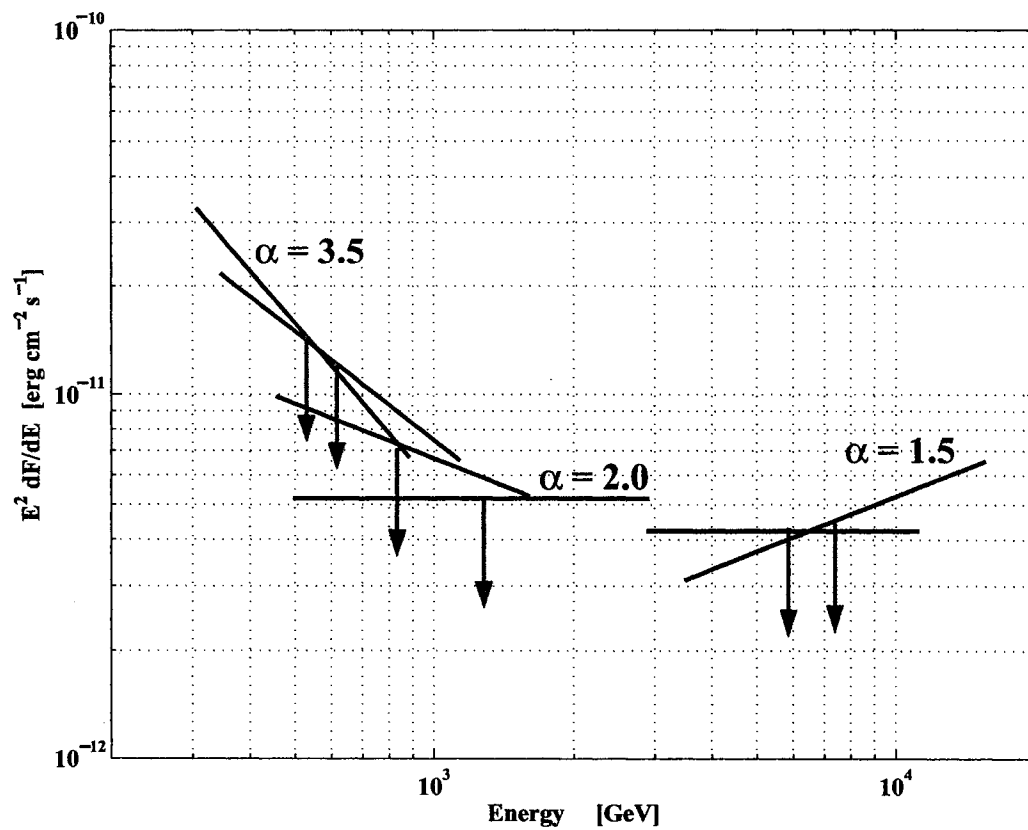


Figure 6.13. Results for the power law MML analysis on the Ursa Minor dwarf galaxy. The slope of the lines indicates the index of the power law spectrum, $dF = E^{-\alpha}dE$, for which the cuts are sensitive. The extent of the line shows the energies for which the cuts are sensitive.

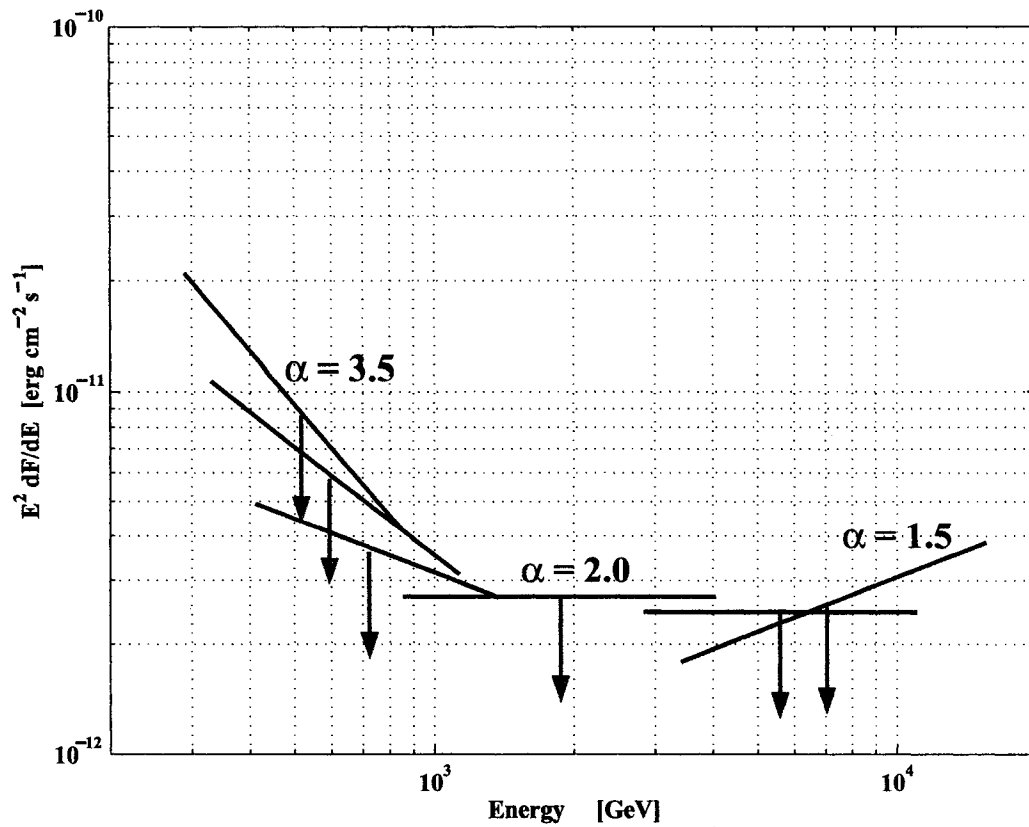


Figure 6.14. Results for the power law MML analysis on the Draco dwarf galaxy. The slope of the lines indicates the index of the power law spectrum, $dF = E^{-\alpha}dE$, for which the cuts are sensitive. The extent of the line shows the energies for which the cuts are sensitive.

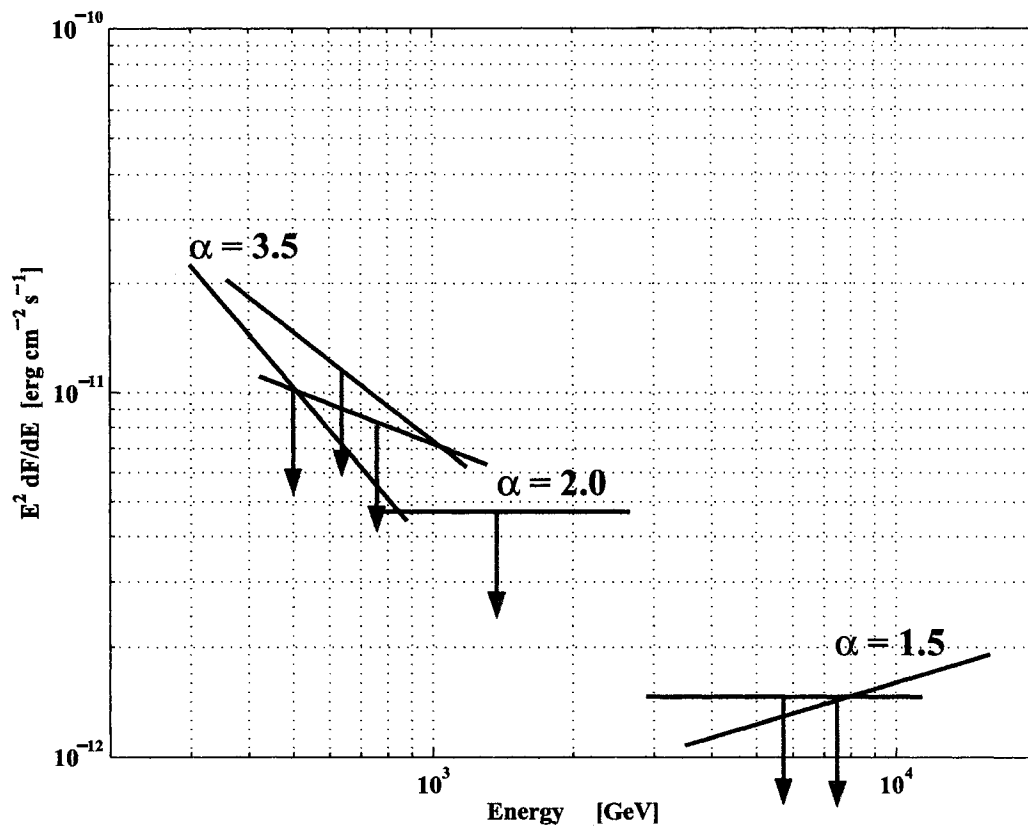


Figure 6.15. Results for the power law MML analysis on the M32 elliptical galaxy. The slope of the lines indicates the index of the power law spectrum, $dF = E^{-\alpha}dE$, for which the cuts are sensitive. The extent of the line shows the energies for which the cuts are sensitive.

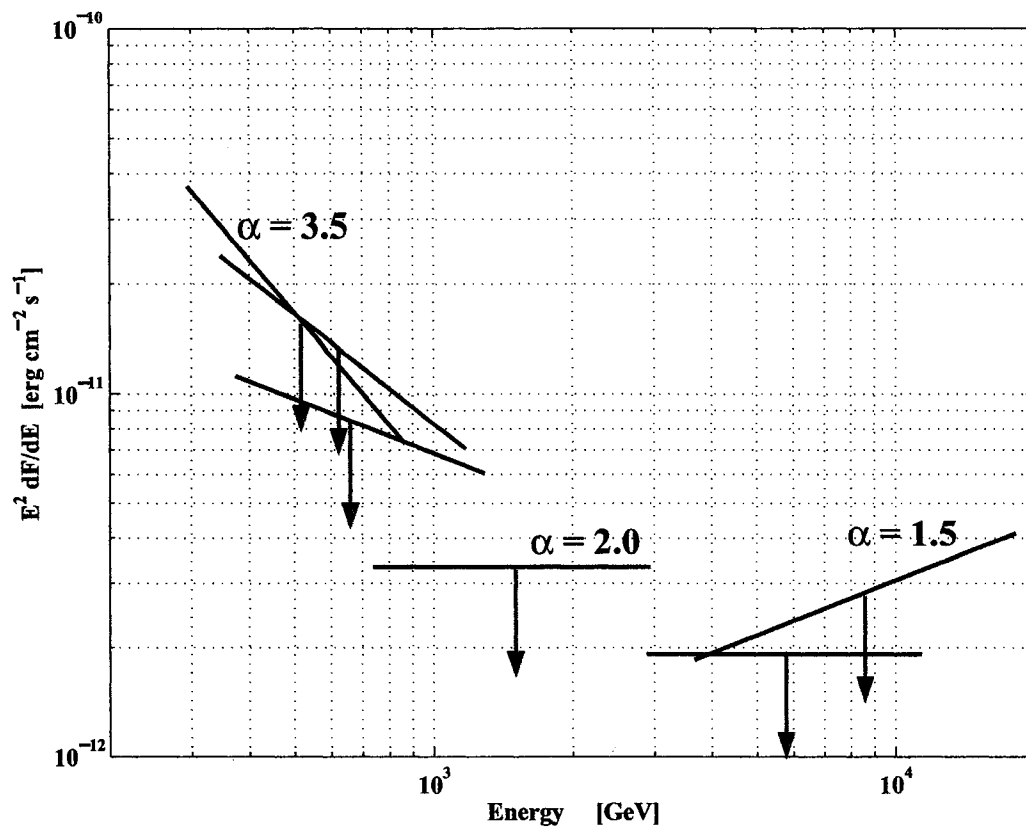


Figure 6.16. Results for the power law MML analysis on the M33 spiral galaxy. The slope of the lines indicates the index of the power law spectrum, $dF = E^{-\alpha}dE$, for which the cuts are sensitive. The extent of the line shows the energies for which the cuts are sensitive.

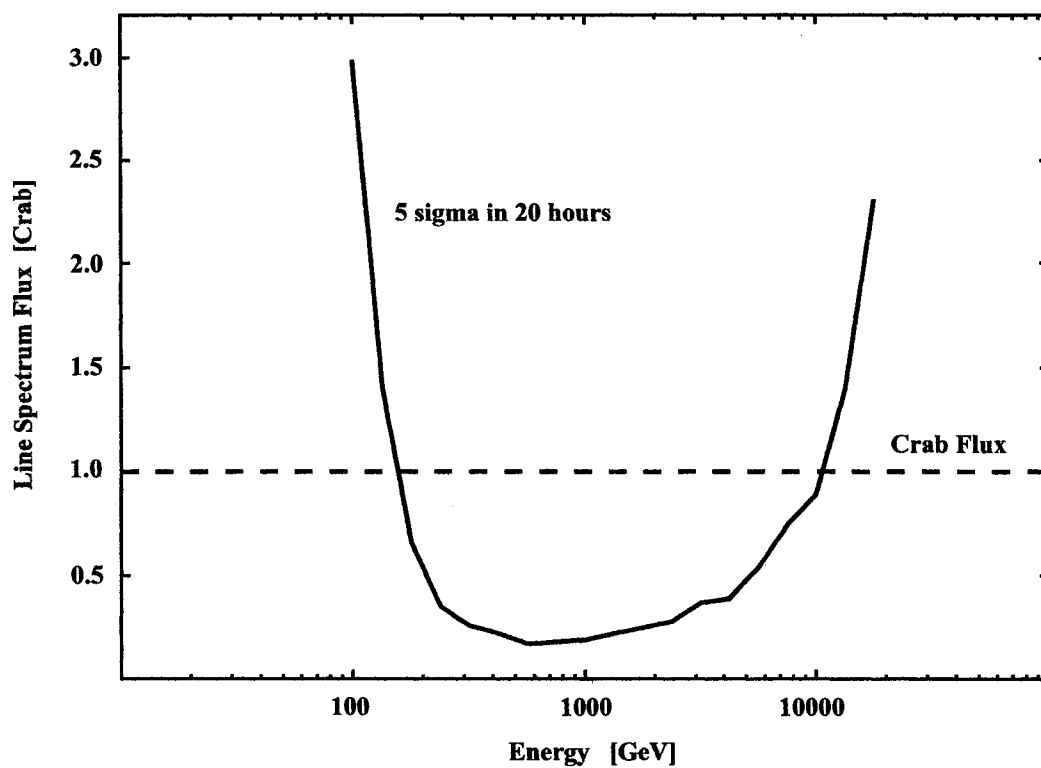


Figure 6.17. Required line flux for a 5 sigma detection in a 20-hour exposure. The background was measured using the Crab OFF exposure.

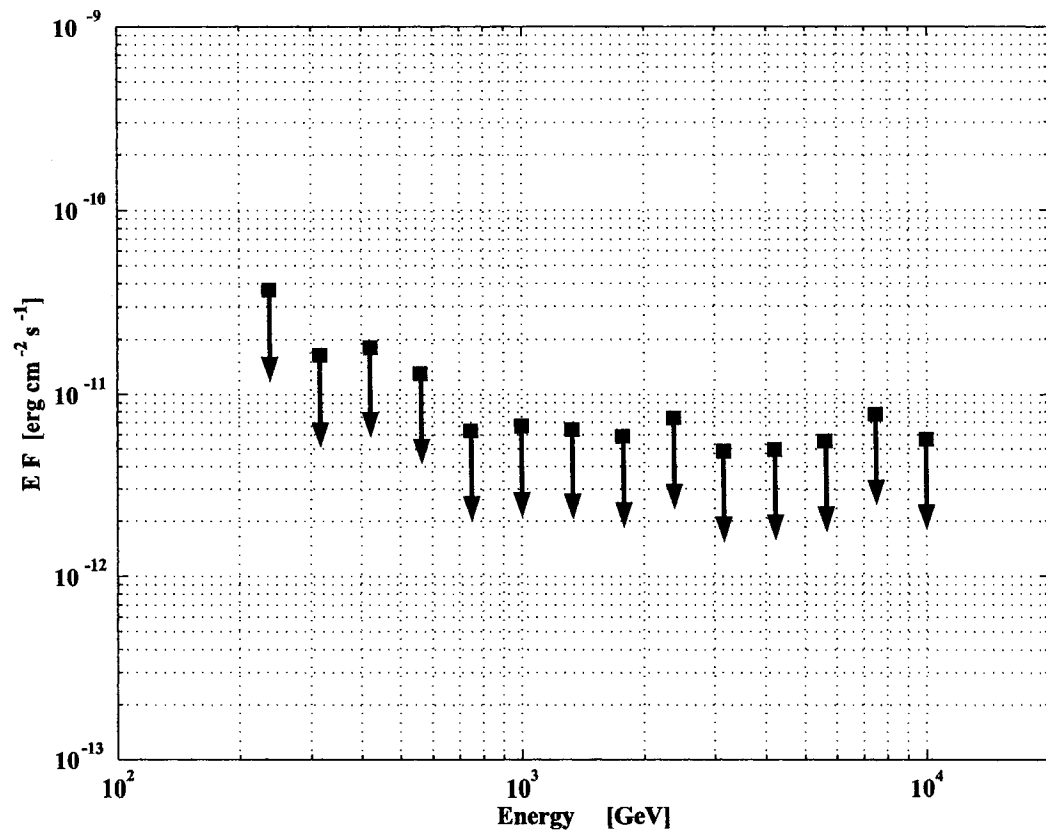


Figure 6.18. Results for the line spectrum MML analysis on the Ursa Minor dwarf galaxy. The position of the points indicates the energies of the line spectra, $dF = \delta(E - E_0)dE$, for which the cuts are sensitive.

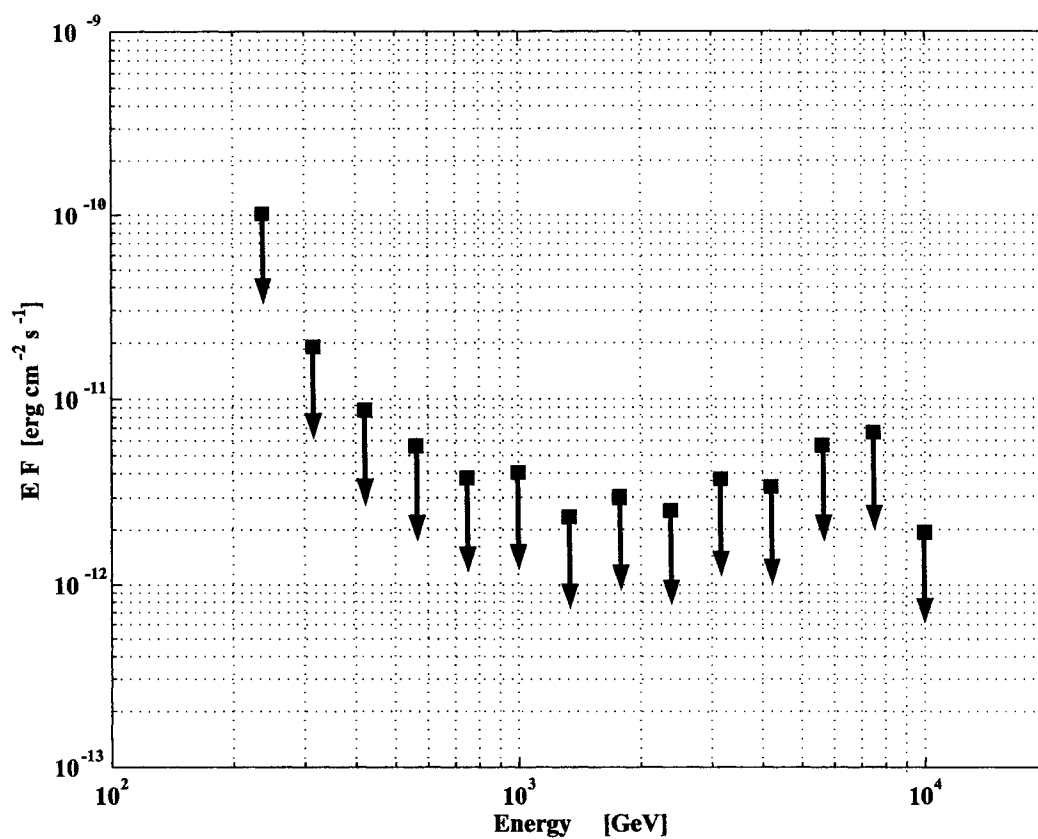


Figure 6.19. Results for the line spectrum MML analysis on the Draco dwarf galaxy. The position of the points indicates the energies of the line spectra, $dF = \delta(E - E_0)dE$, for which the cuts are sensitive.

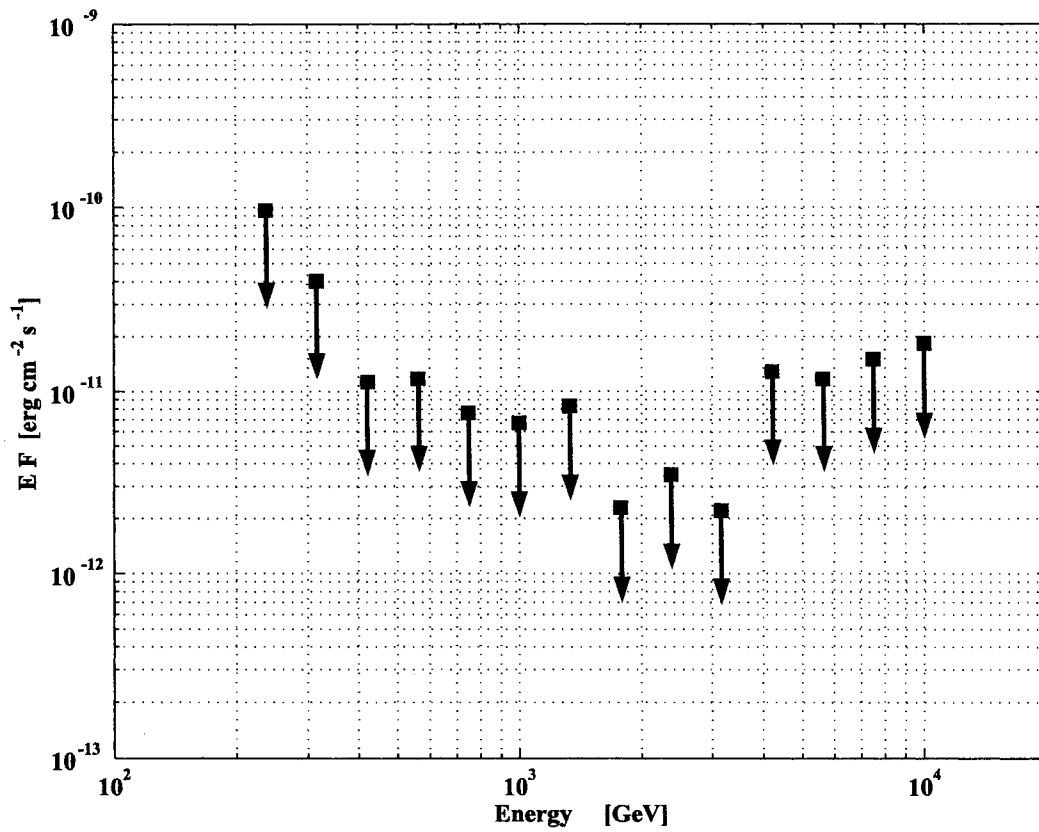


Figure 6.20. Results for the line spectrum MML analysis on the M32 elliptical galaxy. The position of the points indicates the energies of the line spectra, $dF = \delta(E - E_0)dE$, for which the cuts are sensitive.

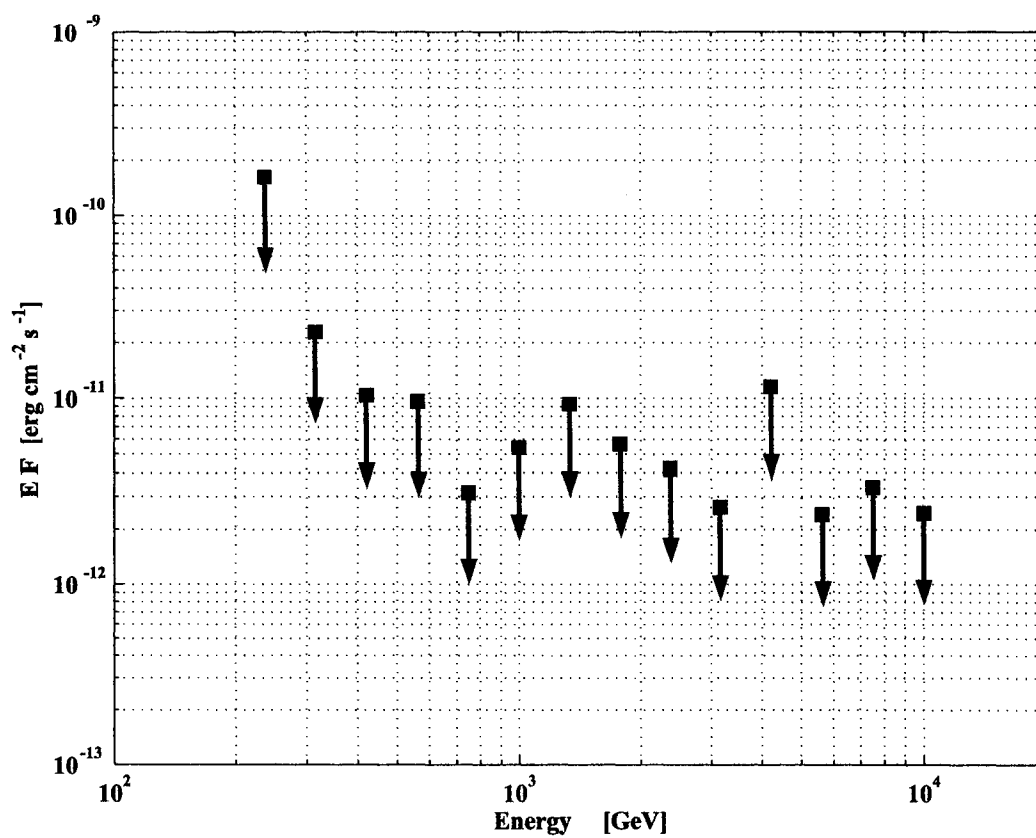


Figure 6.21. Results for the line spectrum MML analysis on the M33 spiral galaxy. The position of the points indicates the energies of the line spectra, $dF = \delta(E - E_0)dE$, for which the cuts are sensitive.

CHAPTER 7

DISCUSSION AND CONCLUSIONS

In this dissertation I have tried to give a brief overview of TeV astronomy along with the discussion and presentation of some current results. The field of TeV astronomy is new and growing rapidly. I have focused on the possibility that a new type of process, specifically a new type of particle species annihilating, could be observed.

Here we discuss the current results of the search for dark matter annihilation above ~ 100 GeV with gamma-ray telescopes. Galactic nuclei are the best places to look because the density and column volume are maximized. The column volume is maximum toward the center because dark matter halos are largely measured to be spherically symmetric around the centers of galaxies.

An enhancement in the density is due to the dark matter density profile. The dark matter density can be measured through the large scale dynamics in the galaxies. For all of the galaxies that have been measured, the dark matter density increases toward the centers of galaxies. The dark matter density profile on small scales is unknown. For all the scenarios, except extreme clumping of the dark matter, the density profiles are spherically symmetric, with perhaps an isothermal core or an increased density in the core due to compression. Finally there could be a spike of dark matter created during adiabatic compression during the formation of supermassive black holes which are at the centers of many galaxies.

I focused on the data from the centers of five galaxies: the dwarf spheroidals in Draco and Ursa Minor, the face-on spiral galaxy M33, the elliptical galaxy M32, and the Milky Way. All five of these objects were observed with the Whipple Telescope in an effort to observe or place limits on the nature of the dark matter. The Whipple Telescope observations of the Milky Way were reported elsewhere [62],

but the results from four other galaxies had not yet been reported. The upper limits on the spectral energy density are combined with other experiments in Figs. (7.1, 7.2, 7.3, and 7.4).

The limits on the energy density of the photon radiation from Draco and Ursa Minor dwarf spheroidal galaxies are particularly interesting. If TeV photons were detected from the cores of these galaxies it would be an almost 'smoking gun' of dark matter annihilation. These galaxies are dark matter dominated and they should have little TeV backgrounds because the supernova rate is low. These observations set the first limits on the TeV radiation from this type of galaxy. The limits on

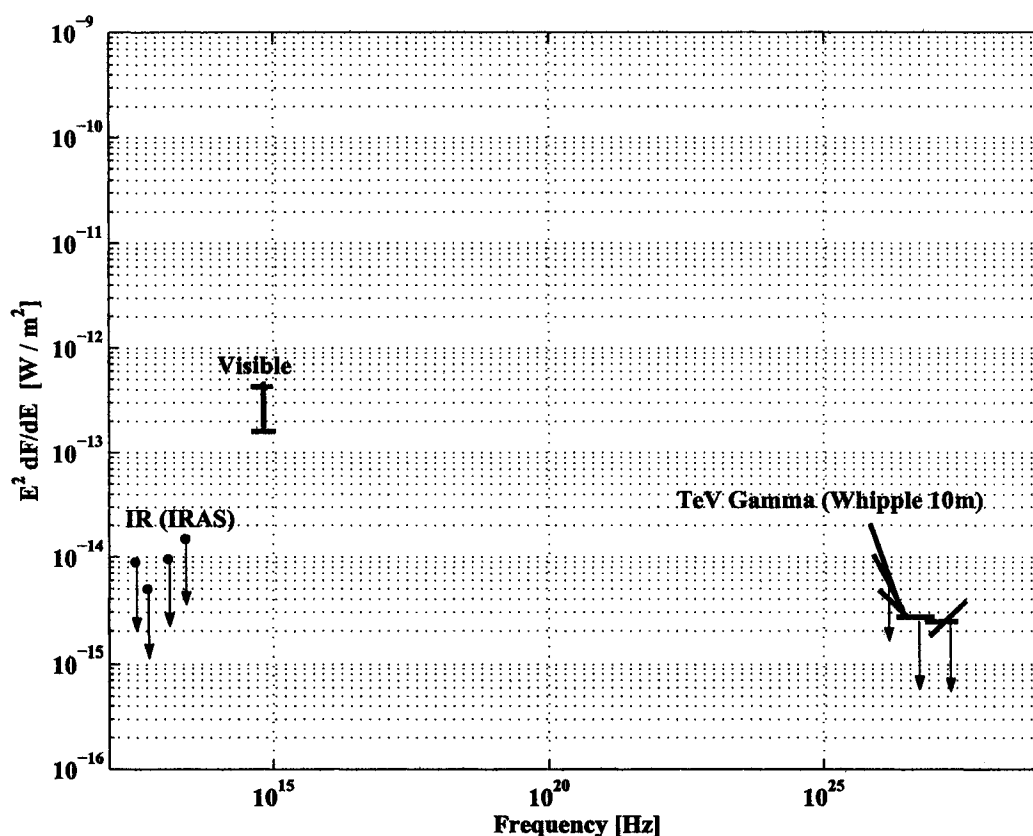


Figure 7.1. Measurements of the spectral energy density of the Draco dwarf spheroidal galaxy. Besides the optical detection, there are upper limits by IRAS at infrared energies and upper limits from this dissertation at TeV energies.

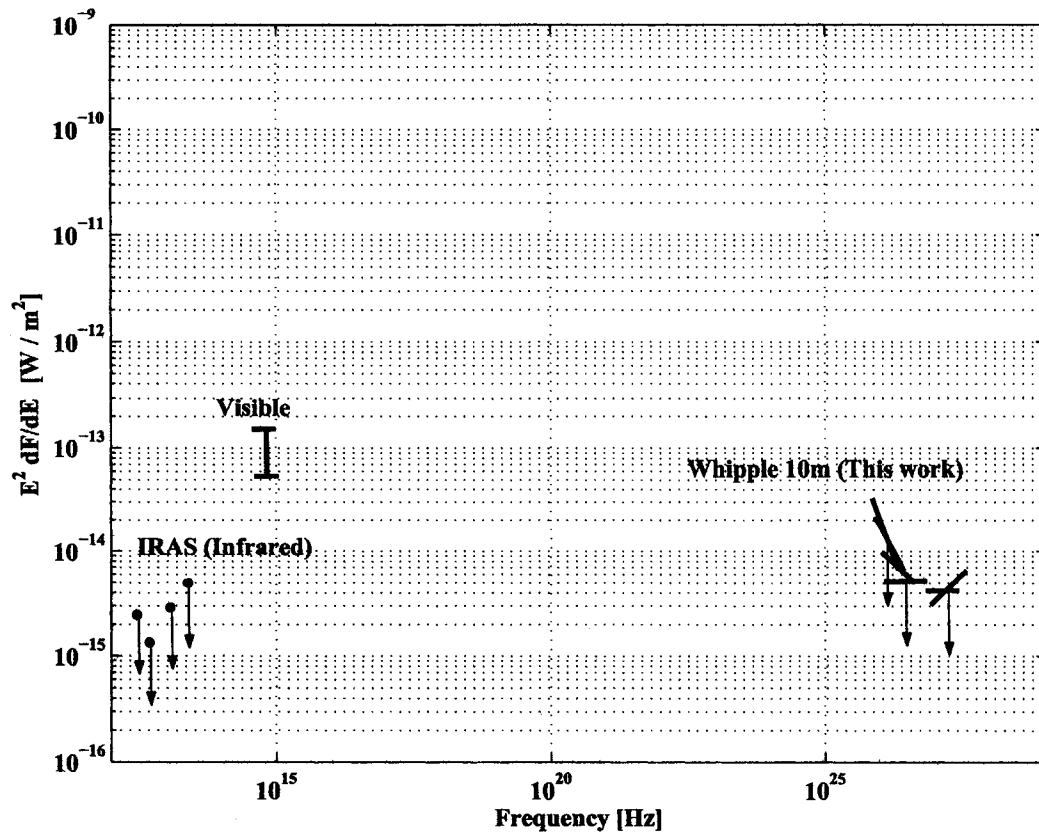


Figure 7.2. Measurements of the spectral energy density of the Ursa Minor dwarf spheroidal galaxy. Besides the optical detection, there are upper limits by IRAS at infrared energies and upper limits from this dissertation at TeV energies.

line annihilation are compared to current models of supersymmetric dark matter in Fig. (7.5) for Draco.

The Whipple Telescope observations of the GC [62] detected a faint gamma-ray emission at the limits of the sensitivity of the telescope. After this initial detection, a very high energy gamma-ray flux from the center of the Milky Way was detected by the HESS collaboration during 2003-2004 [66]. A possible explanation of the very high energy radiation from the GC is WIMP annihilation. The intensity of the annihilation flux is a function of the density profile of dark matter in the GC. The angular distribution of detected gamma rays limits the size of the emission region. Data on the proper motions of stars and star counts around the galactic center

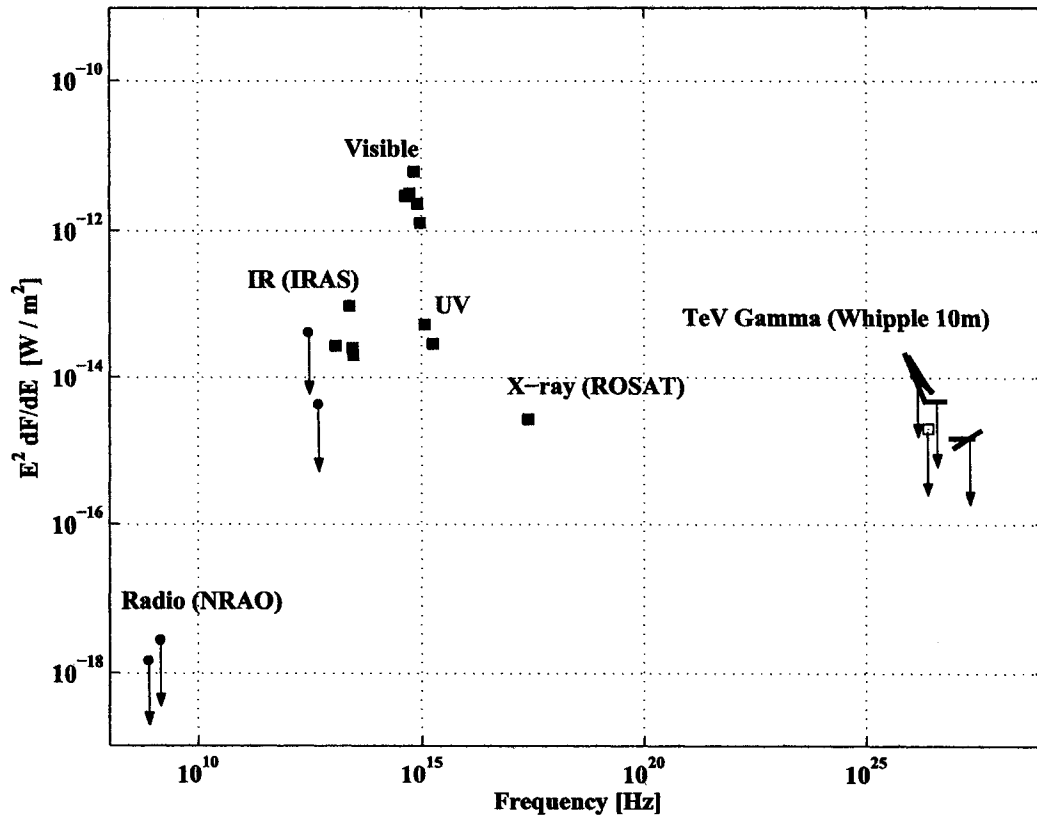


Figure 7.3. Measurements of the spectral energy density of the M32 elliptical galaxy. M32 has been studied from radio to 10 TeV. The open square at 1 TeV (2×10^{26} Hz) is an upper limit from the HEGRA experiment [120].

constrain the size and the mass of the dark matter at the GC. We have shown that the density needed to produce the observed flux from WIMP annihilation is consistent with observational constraints on the mass profile of the GC. For the stellar orbit data and the star counts, we used the infrared data in [95] and [107]. We found that these astronomical constraints on the source profile are comparable to and slightly stronger than the constraint from the angular distribution of photons measured by HESS.

There are several ways in which WIMP annihilation as the origin of the HESS flux could be confirmed or made implausible. As is clear from Fig. (5.8), a slight improvement in either the gamma-ray angular resolution or the constraints from

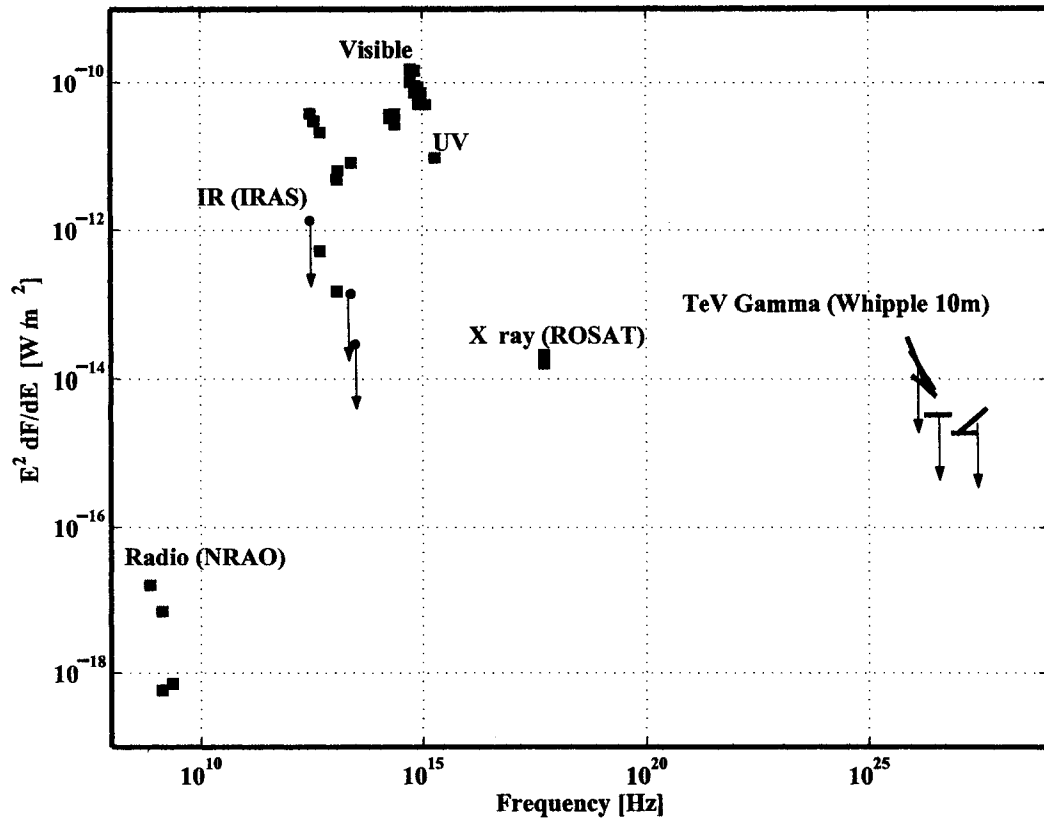


Figure 7.4. Measurements of the spectral energy density of the M33 spiral galaxy. M33 has been measured at radio, infrared, visible, ultraviolet and x-ray energies. The limits on the TeV energy density from this dissertation are the first upper limits at these energies.

stellar orbits may reveal the presence of an extended dark matter annihilation region at the GC. An extended emission out to large angles would be a possible indication of WIMP annihilation. An extended gamma-ray excess with the same spectrum and position of the GC flux has recently been reported by HESS [23]. A spectral cutoff at energies higher than the particle mass is another requirement of the DM hypothesis. The cutoff may be preceded by a gamma-ray line at the particle mass, but this spectral line does not appear to be observable with atmospheric Cherenkov telescopes in the particle models we examined due to the insufficient energy resolution. Absence of variability is another feature of WIMP annihilation; thus variability of

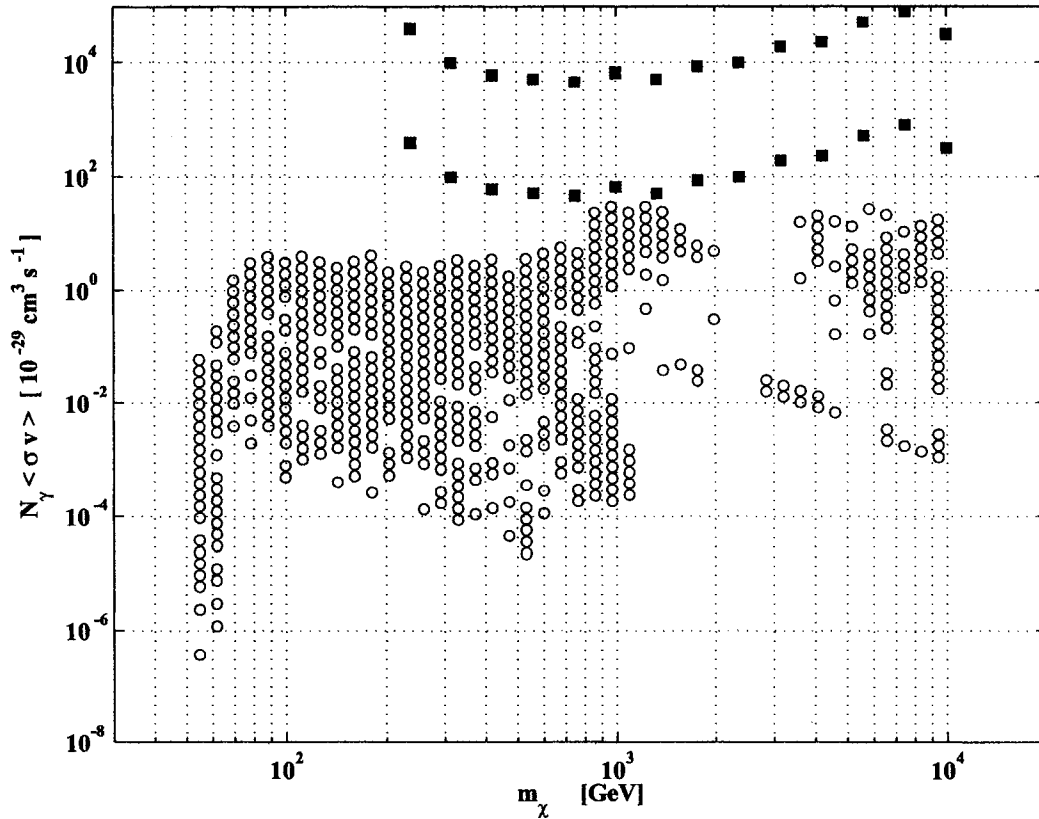


Figure 7.5. Upper limits on the cross-section for annihilation directly into an annihilation line at the mass of the neutralino. The solid squares are upper limits from the Whipple Telescope observations of Draco are from the gamma-ray limits shown in Fig. (6.19). DarkSUSY [97] neutralino cross-sections are shown as open circles. Here we use an isothermal halo, which is favored by observations [76], to derive the upper set of boxes. The lower set of limits includes an order of magnitude enhancement due to, for example, a steeper halo, which has been suggested by simulations [100].

the source would be difficult to reconcile with the DM interpretation of the GC TeV flux. Finally, since the dark matter permeates our Universe, if the same radiation was found in the centers of other mass concentrations, population studies may be possible that could help confirm or deny the annihilation nature of this radiation.

A small spike on an NFW profile could explain the large gamma-ray flux, which is not expected from cored or cusped halos. Astrophysically small spikes in the DM halos are not favored, but not ruled out either. The infrared data of proper

motions in the GC show about three million solar masses confined to a space of 90 AU. The compression of this baryonic matter may adiabatically compress the dark matter and lead to such a spike in the profile [51]. Any merger events with larger stellar sized objects should dynamically heat the DM spike reducing its density.

Further observations of the GC in gamma rays are ongoing. There are hints that the TeV radiation from the Galactic Ridge is connected to the GC point source. The TeV flux from the GC seems to be constant in time and a cutoff in the spectrum (now reported to have a spectrum with $\alpha = 2.4$) has not been found up to energies of ~ 6 TeV [121], so the models considered here are still viable. The nature of this nonthermal radiation source in the center of the Milky Way is still unknown and undergoing active study and observations.

REFERENCES

- [1] E. Rutherford, *Journal of the Royal Astronomical Society of Canada* **1**, 145 (1907).
- [2] R. Millikan, *Popular Astronomy* **34**, 232 (1926).
- [3] Gockel, *Physik Zeit.* **11**, 280 (1910).
- [4] V. Hess, *Physik Zeit.* **13**, 1084 (1912).
- [5] P. Auger, P. Ehrenfest, R. Maze, J. Daudin, and R. A. Fron, *Reviews of Modern Physics* **11**, 288 (1939).
- [6] P. Blackett, *The Emission Spectra of the Night Sky and Aurorae* (1948).
- [7] L. Landau and E. Lifshitz, *Electrodynamics of Continuous Media*, volume 8 of *Landau and Lifshitz Course of Theoretical Physics*, Pergamon Press, Oxford, 1960.
- [8] D. K. Froman and J. C. Stearns, *Reviews of Modern Physics* **10**, 133 (1938).
- [9] B. Rossi and K. Greisen, *Reviews of Modern Physics* **13**, 240 (1941).
- [10] J. Jelley, *British Journal of Applied Physics* **6**, 227 (1955).
- [11] J. H. Fruin, J. V. Jelley, C. D. Long, N. A. Porter, and T. C. Weekes, *Physics Letters* **10**, 176 (1964).
- [12] J. Delvaille et al., A large-area gas-cerenkov detector for high-energy gamma-ray astronomy, in *New Techniques in Space Astronomy. IAU Symposium no. 41*, edited by F. Labuhn and R. Lust, page 75, International Astronomical Union, 1970.
- [13] J. Davies and E. Cotton, *Journal of Solar Energy* **1**, 16 (1957).
- [14] G. Pühlhofer et al., *Astroparticle Physics* **20**, 267 (2003).
- [15] T. C. Weekes et al., *The Astrophysical Journal* **342**, 379 (1989).
- [16] F. Aharonian et al., *Science* **307**, 1938 (2005).
- [17] F. Aharonian et al., *The Astrophysical Journal* **636**, 777 (2006).
- [18] F. Aharonian et al., *Astrophysical Journal Letters* **435**, 17 (2005).

- [19] F. Aharonian et al., *Nature* **432**, 75 (2004).
- [20] F. Aharonian et al., *The Astrophysical Journal* **619**, 306 (2005).
- [21] J. B. Pollack and G. G. Fazio, *Physical Review* **131**, 2684 (1963).
- [22] R. J. Gould and G. R. Burbidge, *Annales d'Astrophysique* **28**, 171 (1965).
- [23] F. Aharonian et al., *Nature* **439**, 695 (2006).
- [24] F. Aharonian et al., *Astronomy and Astrophysics* **442**, 1 (2005).
- [25] J. G. Kirk, L. Ball, and O. Skjaeraasen, *Astroparticle Physics* **10**, 31 (1999).
- [26] F. Aharonian et al., *Science* **309**, 746 (2005).
- [27] J. Albert et al., *Scienceexpress* [www.scienceexpress.org/18 May 2006/Page 1/10.1126/science.1128177](http://www.scienceexpress.org/18_May_2006/Page_1/10.1126/science.1128177) (2006).
- [28] W. Cui, *Science* **309**, 714 (2005).
- [29] M. Punch et al., *Nature* **358**, 477 (1992).
- [30] L. Costamante and G. Ghisellini, *Astronomy and Astrophysics* **384**, 56 (1936).
- [31] J. Quinn et al., *Astrophysical Journal Letters* **456**, 83 (1996).
- [32] F. Aharonian et al., *Astronomy and Astrophysics* **448**, 19 (2006).
- [33] J. Zweerink et al., *The Astrophysical Journal* **490**, 141 (1997).
- [34] S. Fegan et al., *The Astrophysical Journal* **624**, 638 (2005).
- [35] D. B. Kieda, S. P. Swordy, and S. P. Wakely, *Astroparticle Physics* **15**, 287 (2001).
- [36] W. Hofmann, Performance limits for cherenkov instruments, in *Towards a Network of Atmospheric Cherenkov Telescopes VII*, edited by B. Degrange and G. Fontaine, Palaiseau, 2005.
- [37] M. S. Roberts and R. N. Whitehurst, *The Astrophysical Journal* **201**, 327 (1975).
- [38] J. P. Ostriker and P. J. E. Peebles, *The Astrophysical Journal* **186**, 467 (1973).
- [39] E. P. Hubble, A relation between distance and radial velocity among extragalactic nebulae, in *Proceedings of the National Academy of Sciences of the United States of America*, volume 15, pages 168–173, 1929.
- [40] E. Hubble and M. L. Humason, *The Astrophysical Journal* **74**, 43 (1931).

- [41] S. Weinberg, *Gravitation and Cosmology*, Wiley, New York, 1972.
- [42] A. G. Riess et al., *The Astrophysical Journal* **607**, 665 (2004).
- [43] C. L. Bennett et al., *Astrophysical Journal Supplement Series* **148**, 1 (2003).
- [44] J. C. Mather, D. J. Fixsen, R. A. Shafer, C. Mosier, and D. T. Wilkinson, *The Astrophysical Journal* **512**, 511 (1999).
- [45] T. J. Pearson et al., *The Astrophysical Journal* **591**, 556 (2003).
- [46] J. H. Goldstein et al., *The Astrophysical Journal* **599**, 773 (2003).
- [47] C. Alcock et al., *The Astrophysical Journal* **550**, L169 (2001).
- [48] C. Afonso et al., *Astronomy and Astrophysics* **400**, 951 (2003).
- [49] A. Udalski et al., *Acta Astronomica* **43**, 289 (1993).
- [50] D. N. Spergel et al., *Astrophysical Journal Supplement Series* **148**, 175 (2003).
- [51] P. Gondolo and J. Silk, *Physical Review Letters* **83**, 1719 (1999).
- [52] P. Ullio, H. Zhao, and M. Kamionkowski, *Physical Review D* **64**, 043504 1 (2001).
- [53] D. Merritt, M. Milosavljevic, L. Verde, and R. Jiminez, *Physical Review Letters* **88**, 191301 1 (2002).
- [54] L. Bergström, P. Ullio, and J. H. Buckley, *Astroparticle Physics* **9**, 137 (1998).
- [55] P. Gondolo, Private communication, 2004.
- [56] J. Silk and H. Bloemen, *The Astrophysical Journal* **313**, 47 (1987).
- [57] F. Stecker and A. Tylka, *The Astrophysical Journal* **343**, 169 (1989).
- [58] R. Flores and J. Primack, *The Astrophysical Journal* **427**, 1 (1994).
- [59] H. Mayer-Hasselwander et al., *Astronomy and Astrophysics* **335**, 161 (1998).
- [60] A. Cesarini, F. Fucito, A. Lionetto, A. Morselli, and P. Ullio, *Astroparticle Physics* **21**, 267 (2004).
- [61] N. Evans, F. Ferrer, and S. Sarkar, *Physical Review D* **69**, 123501 (2004).
- [62] K. Kosack et al., *The Astrophysical Journal* **608**, 97 (2004).
- [63] K. Tsuchiya et al., *The Astrophysical Journal* **606**, 115 (2004).

- [64] W. Hofmann for the HESS Collaboration, Status of the H.E.S.S. project, in *the 29th International Cosmic Ray Conference*, edited by T. Kajita, Y. Asaoka, A. Kawachi, Y. Matsubara, and M. Sasaki, pages 2811–2814, International Union of Pure and Applied Physics (IUPAP), 2003.
- [65] A. Ghez et al., *The Astrophysical Journal* **620**, 744 (2005).
- [66] F. Aharonian et al., *Astronomy and Astrophysics* **425**, 13 (2004).
- [67] F. Aharonian et al., *Nature* **432**, 75 (2005).
- [68] F. Aharonian et al., *Astronomy and Astrophysics* **432**, L25 (2005).
- [69] F. Aharonian and A. Neronov, *The Astrophysical Journal* **619**, 306 (2005).
- [70] A. Atoyan and C. Dermer, *The Astrophysical Journal* **617**, 123 (2004).
- [71] L. Bergström, T. Bringmann, M. Eriksson, and M. Gustafsson, *Physical Review Letters* **94**, 131301 (2005).
- [72] D. Horns, *Physical Letters B* **611**, 297 (2005).
- [73] O. Gnedin and J. Primack, *Physical Review Letters* **93**, 061302 (2004).
- [74] G. Bertone and D. Merritt, *Physical Review D* **72**, 103502 (2005).
- [75] M. Wilkinson, J. Kleyana, N. Evans, and G. Gilmore, *Monthly Notices of the Royal Astronomical Society* **330**, 778 (2002).
- [76] J. Kleyana, M. I. Wilkinson, N. W. Evans, G. Gilmore, and C. Frayn, *Monthly Notices of the Royal Astronomical Society* **330**, 792 (2002).
- [77] D. Lynden-Bell, *Monthly Notices of the Royal Astronomical Society* **136**, 101 (1967).
- [78] C. Tyler, *Physical Review D* **66**, 023509 (2002).
- [79] S. Profumo and M. Kamionkowski, *Journal of Cosmology and Astrophysics* **03**, 003 (2006).
- [80] L. Bergström and D. Hooper, *Physical Review D* **73**, 063510 (2006).
- [81] A. Z. Bonanos, K. Z. Stanek, A. H. Szentgyorgyi, D. D. Sasselov, and G. Á. Bakos, *The Astronomical Journal* **127**, 861 (2004).
- [82] K. J. Mighell and C. J. Burke, *The Astronomical Journal* **118**, 366 (1999).
- [83] J. T. Kleyana, M. J. Geller, S. J. Kenyon, M. J. Kurtz, and J. R. Thorstensen, *The Astronomical Journal* **115**, 2359 (1998).
- [84] P. Eskridge and A. Schweitzer, *The Astronomical Journal* **122**, 3106 (2001).

- [85] J. Kleyana, M. Wilkinson, G. Gilmore, and E. N.W., *The Astrophysical Journal* **588**, L21 (2003).
- [86] M. Bellazzini et al., *The Astronomical Journal* **124**, 3222 (2002).
- [87] H. Babcock, *Lick Observatory Bulletin* **498**, 41 (1939).
- [88] A. McConnachie et al., *Monthly Notices of the Royal Astronomical Society* **356**, 979 (2005).
- [89] C. Joseph et al., *The Astrophysical Journal* **550**, 668 (2001).
- [90] T. Lauer, S. Faber, E. Ajhar, C. Grillmair, and P. Scowen, *The Astronomical Journal* **116**, 2263 (1998).
- [91] E. Corbelli and P. Salucci, *Monthly Notices of the Royal Astronomical Society* **311**, 441 (2000).
- [92] K. Gebhardt et al., *The Astronomical Journal* **122**, 2469 (2001).
- [93] A. Ghez, B. Klein, M. Morris, and E. Becklin, *The Astrophysical Journal* **509**, 678 (1998).
- [94] A. Ghez, M. Morris, E. Becklin, A. Tanner, and T. Kremenek, *Nature* **407**, 349 (2000).
- [95] A. Ghez et al., *Astronomische Nachrichten Supplementary Issue 1*, 527 (2003).
- [96] M. Morris, (2005).
- [97] P. Gondolo et al., *Journal of Cosmology and Astrophysics* **07**, 008 (2004).
- [98] G. Gelmini and P. Gondolo, *Physical Review D* **74**, 023510 (2006).
- [99] S. Profumo, *Physical Review D* **72**, 103521 (2005).
- [100] J. F. Navarro, C. S. Frenk, and S. D. M. White, *The Astrophysical Journal* **490**, 493 (1997).
- [101] J. Silk and A. Stebbins, *The Astrophysical Journal* **411**, 439 (1993).
- [102] E. W. Kolb and I. I. Tkachev, *Physical Review D* **50**, 769 (1994).
- [103] L. Bergström, J. Edsjö, P. Gondolo, and P. Ullio, *Physical Review D* **59**, 043506 (1999).
- [104] R. Aloisio, P. Blasi, and A. Olinto, *The Astrophysical Journal* **601**, 47.
- [105] A. Gurevich and K. Zybin, *Sov.Phys.Usp.* **165**, 723 (1995).
- [106] M. Reid, *Annual Review of Astronomy and Astrophysics* **31**, 345 (1993).

- [107] R. Genzel et al., *The Astrophysical Journal* **594**, 812 (2003).
- [108] J. Finley and the VERITAS Collaboration, The whipple observatory granite III upgrade program, in *International Cosmic Ray Conference, ICRC 26*, edited by D. Kieda, University of Utah, 1999.
- [109] G. Mohanty et al., *Astroparticle Physics* **9**, 15 (1998).
- [110] P. Reynolds et al., *The Astrophysical Journal* **404**, 206 (1993).
- [111] M. Catanese et al., *The Astrophysical Journal* **501**, 616 (1998).
- [112] M. Kertzman and G. Sembroski, The whipple 10m zenith strip sky survey, in *VERITAS Collaboration Internal Memo*, 2006.
- [113] S. Lebohec and J. Holder, *Astroparticle Physics* **19**, 221 (2003).
- [114] D. Horan, in *Ph.D. Dissertation*, University College Dublin, 2002.
- [115] T. Nagai, in *Ph.D. Dissertation*, University of Utah, 2005.
- [116] T. Gaisser, *Cosmic Rays and Particle Physics*, University Press, Cambridge, 1991.
- [117] G. Walker, in *Ph.D. Dissertation*, University of Utah, 2004.
- [118] T.-P. Li and Y.-Q. Ma, *The Astrophysical Journal* **272**, 317 (1983).
- [119] O. Helene, *Nuclear Instruments and Methods in Physics Research A* **228**, 120 (1984).
- [120] F. Aharonian et al., *Astronomy and Astrophysics* **400**, 153 (2003).
- [121] L. Rolland for the HESS Collaboration, Spectrum and variability of the VHE Galactic Centre source observed with H.E.S.S., in *the 29th International Cosmic Ray Conference*, edited by T. Kajita, Y. Asaoka, A. Kawachi, Y. Matsubara, and M. Sasaki, pages 2811–2814, International Union of Pure and Applied Physics (IUPAP), 2003.